Norwegian University of Science and Technology (NTNU)

Kavli Institute for Systems Neuroscience / Centre for Neural Computation

Master's Thesis

Amyloid β-immunoreactivity in cell populations of the hippocampal region in a transgenic rat model of Alzheimer's disease

Author:

Anne Nagelhus

Supervisor:

Menno P. Witter

Faculty of Medicine

Department of Neuroscience

Trondheim, June 2015

Norwegian University of Science and Technology

ACKNOWLEDGEMENTS

The work presented in this master thesis was performed at the Kavli Institute for Systems Neuroscience and Centre for Neural Computation at the Norwegian University of Science and Technology, under the supervision of Professor Menno P. Witter.

I would like to thank my supervisor Menno Witter for his guidance, support, and great patience throughout this project. Special thanks and much appreciation to Ingrid Heggland for all her help and for always taking the time to answer my questions and give me advice – I could not have done this without. I would also like to thank Asgeir Kobro-Flatmoen for supervising and teaching me during the first part of the project.

Thanks also to all the wonderful people in the Witter group for the help and support and coffee breaks, and especially to Hanne T. Soligard and Bruno Monterotti for their technical assistance. Gunhild, thank you for the laughs and the weird conversations, and for making our office the most decorated and interesting one in the building.

Lastly, thank you to my family and friends for their tremendous moral support and for always believing in me.

ABSTRACT

Alzheimer's disease (AD) is one of the most devastating neurodegenerative disorders and the most common cause of dementia in the elderly. Both amyloid β (Aβ) and tau pathology show a characteristic spatiotemporal progression throughout the brain. In particular, parts of the hippocampal formation (HF) and parahippocampal region (PHR), which are involved in memory and spatial processing, are heavily affected in early stages. By the time the clinical symptoms of AD start to manifest, the neuropathological changes in the brain are severe, and it is thus vital to identify cell types that are vulnerable to early pathology. With use of the transgenic McGill-R-Thy1-APP rat model, which faithfully mimics human Aβ pathology, this thesis aimed to determine whether neuronal populations in HF and PHR that accumulate intracellular Aβ (iAβ) in the pre-plaque stage of AD are characterised by the presence of distinct molecular markers. The first part focused on a subset of principal neurons in layer II of entorhinal cortex (EC) that express the glycoprotein reelin and project to HF. By doing immunohistochemical double-labelling and unbiased stereology, we found that reelin-positive principal cells in layer II of both lateral and medial EC are heavily immunoreactive to iAβ in the pre-plaque stage in homozygous McGill-R-Thy1-APP rats. Reelin is important for synaptic plasticity and is believed to be involved in dysfunction associated with AD, and accumulation of iAβ in the reelin-expressing population of principal cells in layer II of EC could have important effects on plasticity in the entorhinal-hippocampal network. A subset of calbindin-positive cells in medial EC layer II were also found to express iAβ. In view of the importance of interneurons in network functionality, in the second part of this thesis we investigated whether iAβ is also expressed in interneurons in early stages of disease in homozygous McGill-R-Thy1-APP rats. Immunohistochemical double-labelling showed that interneurons in all subareas of HF and PHR express iAβ at the pre-plaque stage. iAβ was found in subsets of both parvalbumin- and somatostatin-positive interneurons. Due to early amyloid pathology in subiculum and its reciprocal connections with EC, we counted iAβ-positive interneurons in this area and found that a significantly larger proportion of interneurons in dorsal and intermediate regions of subiculum were immunoreactive to iAβ than in ventral regions. Taken together, the results of this thesis suggest that iAβ is expressed in a large number of principal cells and interneurons at early ages in the McGill-R-Thy1-APP rat model of AD, and that these cells are heterogeneous with regards to their neurochemical profiles. The finding that both principal cells and interneurons are affected heavily by iAβ in HF and PHR supports the already established idea that AD not only affects single cells or synapses, but also local assemblies and larger networks of neurons.

TABLE OF CONTENTS

ABBREVIATIONS

Aβ	Amyloid β
AD	Alzheimer's disease
ABC	Avidin-biotin complex
AMPA	α-amino-3-hydroxy-5-methyl-4-isoxazolepropionic acid
ANOVA	Analysis of variance
APir	Amygdalopiriform transition area
APOE	Apolipoprotein E
ApoER2	Apolipoprotein E receptor 2
APP/AβPP	Amyloid precursor protein
BACE-1	β-site amyloid precursor protein cleaving enzyme 1
BP	Band-pass
CA	Cornu Ammonis
CB	Citrate buffer
CE	Coefficient of error
CTF	C-terminal fragment
CV	Coefficient of variation
DAB	3,3'-diaminobenzidine
Dab-1	Disabled-1
DG	Dentate gyrus
DMSO	Dimethyl sulfoxide
DNA	Deoxyribonucleic acid
DS	Dorsal subiculum
EC	Entorhinal cortex
FA	Formic acid
FAD	Familial Alzheimer's disease
GABA	γ-aminobutyric acid
GAD67	Glutamate decarboxylase 67-kDa isoform
hAPP	Human amyloid precursor protein
HF	Hippocampal formation
HIER	Heat-induced epitope retrieval
iAβ	Intracellular amyloid β
IF	Immunofluorescence
IgG	γ-immunoglobulin
IS	Intermediate subiculum
LII	Layer II
LIII	Layer III
LEC	Lateral entorhinal cortex
LP	Low-pass
LTD	Long-term depression
LTP	Long-term potentiation
MAPT	Microtubule-associated protein tau
MCI	Mild cognitive impairment
MEC	Medial entorhinal cortex
NA	Numerical aperture
NFTs	Neurofibrillary tangles
NGS	Normal goat serum
NMDA	*N*-methyl-D-aspartase
P	Postnatal
PaS	Parasubiculum
PB	Phosphate buffer
PBT	Phosphate buffer with Triton X-100
PCR	Polymerase chain reaction
PER	Perirhinal cortex
PFA	Paraformaldehyde
PHR	Parahippocampal region

POR	Postrhinal cortex	Sub	Subiculum
PrS	Presubiculum	TBS-Tx	Tris-buffered saline with Triton X-100
qPCR	Quantitative (real-time) polymerase chain reaction	Tris	Tris(hydroxymethyl)-aminomethane
RNA	Ribonucleic acid	VldlR	Very low-density lipoprotein receptor
ROI	Region of interest		
RSC	Retrosplenial cortex		
SD	Standard deviation	VS	Ventral subiculum
SRS	Systematically randomly sampled	WT	Wild-type

1. INTRODUCTION

1.1. Alzheimer's disease

1.1.1. Dementia and Alzheimer's disease

The concept of dementia has evolved over centuries, from a natural consequence of ageing to a 'decay of perception and memory, in old age', and a condition of cognitive and psychological impairment associated with chronic brain disease (Grand and Feldman, 2007). We now have a contemporary understanding of dementia as an acquired syndrome characterised by deterioration of cognitive functions and affecting memory, behaviour, and the ability to perform normal, everyday activities (World Health Organization, 2015). With an increasing elderly population, dementia is becoming one of the leading concerns of modern medicine. In 2001, there was an estimated 24.3 million sufferers worldwide, with an estimate of 81.1 million by 2040 (Ferri et al., 2005). The most frequent cause of dementia in the elderly is Alzheimer's disease (AD).

In 1906, the German physician Alois Alzheimer described the major hallmarks of the 'presenile dementia' that would later be given his name. He had observed specific alterations in the cerebral cortex of an autopsied brain from a woman who had died at age 51. Prior to her death, the patient had showed symptoms such as memory deficits, aphasia, disorientation, paranoia, and auditory hallucinations (Maurer et al., 1997). In his subsequent report, titled 'About a peculiar disease of the cerebral cortex' and published a year later, Alzheimer described degenerating cells with bundles of neurofibrils and the presence of extracellular plaque-like deposits (Graeber and Mehraein, 1999).

Today, AD is known as one of the most devastating neurodegenerative disorders. Clinically, the disease manifests itself with gross and progressive cognitive impairment. In the first stages of the disease, most patients lose their ability to retain new information and encode new memories, and, over time, the capacity for reasoning, abstraction, and language declines. The disease is also characterised by loss of orientation and agnosia, as well as psychological manifestations such as depression, anxiety, and hallucinations, and other neurological abnormalities such as increased muscle tone or gait disorders (Forstl and Kurz, 1999).

1.1.2. Pathophysiology of Alzheimer's disease

Over the century following the first description by Alzheimer, the neurofibril bundles, or neurofibrillary tangles (NFTs), were identified as filamentous inclusions in the cell bodies and proximal dendrites that contain helical and straight filaments composed of aberrantly misfolded and hyperphosphorylated tau, a microtubule-stabilising protein (Crowther, 1991; Mandelkow and Mandelkow, 2012). The extracellular plaques were recognised as large aggregates of fibrillary amyloid β (Aβ) peptide (Figure 1.1). Dense-core plaques are round or spherical structures 15-25 µm in diameter consisting of a peripheral rim of dystrophic neurites, reactive astrocytes, and activated microglia. Diffuse plaques are non-neuritic and not associated with reactive glial cells, and, unlike dense-core plaques, are common in cognitively intact elderly people (Serrano-Pozo et al., 2012).

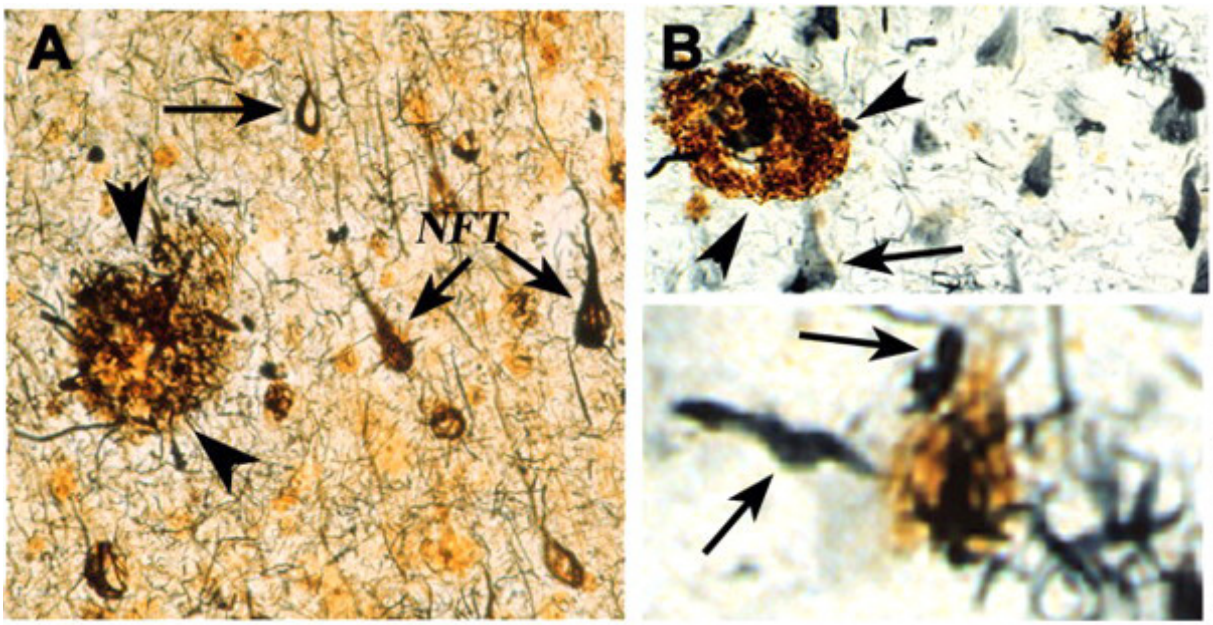

Figure 1.1. The two neuropathological hallmarks of Alzheimer's disease, neurofibrillary tangles (NFTs; arrows) and amyloid plaques (arrowheads), shown by Bielschowsky silver staining (A) and by the use of antibodies (B). Figure adapted from Nixon (2007).

Neuropathologically, AD is also associated with severe neuronal death, leading to generalised cortical atrophy, with narrowed gyri, widened sulci, reduced brain weight, and enlarged ventricles. The disease is further characterised by increased oxidative stress, amyloid angiopathy, altered glucose metabolism, reactive astrocytes and activated microglial cells, and synaptic alterations (Serrano-Pozo et al., 2012). Despite the major neuropathological hallmarks first being identified more than a hundred years ago,

the mechanisms behind the disease process are still poorly understood. Research has increasingly focused on early stages of disease, and it has become evident that the presence of biological markers can precede and predict clinical symptoms by decades. One of the most crucial and yet unanswered questions relates to the origin of pathology, and whether either amyloid or tau act as a causative to initiate disruption of each other's biochemistry and the other pathological changes, or whether they represent parallel pathogenic pathways.

1.1.3. Amyloid β, APP, and the amyloid cascade hypothesis

In 1992, John Hardy and Gerald Higgins first suggested that aggregation of Aβ is the causative step in AD (Hardy and Higgins, 1992). According to the 'amyloid cascade hypothesis', the formation of NFTs, inflammation, oxidative stress, glutamatergic excitotoxicity, and neuronal apoptosis are all considered secondary to overproduction, decreased clearance, or enhanced aggregation of Aβ.

Aβ peptides are cleavage products of the amyloid precursor protein (APP), a large transmembrane (type 1 membrane-) glycoprotein with a long extracellular N-terminal and a short intracellular C-terminal domain that is present in all parts of many types of neurons, as well as in a variety of non-neuronal cells. APP is cleaved by α-secretase in approximately 90% of cases in normal physiological conditions in the so-called non-amyloidogenic processing pathway. When cleaved by the β-secretase BACE-1 (β-site amyloid precursor protein cleaving enzyme 1) in the amyloidogenic pathway, benign amyloid is produced. Subsequent γ-secretase cleavage leads to formation of potentially toxic Aβ (Hiltunen et al., 2009; Querfurth and LaFerla, 2010).

Aβ peptides are produced constitutively in various lengths of 36 to 43 amino acids, but exist in two main forms, the predominant of which has 40 amino acids and the minor one 42. In AD, amyloid deposition begins with the more neurotoxic and rapidly nucleating Aβ42 and continues with Aβ40, which accumulates later (Jarrett et al., 1993; Liao et al., 2007). An imbalance between production and clearance of aggregated peptides causes Aβ to accumulate. Since the native Aβ has an α-helix structure and can easily be destabilised to adopt a β-sheet formation, such an imbalance may lead to subsequent aggregation into fibrils (Querfurth and LaFerla, 2010).

One of the major drawbacks of the amyloid cascade hypothesis involves the wealth of evidence that amyloid plaque burden, unlike NFTs and cell loss, does not correlate with severity of dementia (Arriagada et al., 1992; Bierer et al., 1995; Giannakopoulos et al., 2003). Insoluble plaques may be relatively inactive, and instead serve as reservoirs for smaller assemblies of Aβ. Soluble Aβ species,

including oligomers found intracellularly, correlate to a much higher degree with presence and degree of cognitive impairments than insoluble plaques (Haass and Selkoe, 2007).

1.1.4. Toxicity of amyloid ß and the role of intracellular amyloid ß

The toxicity of oligomeric Aβ was first addressed in 1990 (Yankner et al., 1990) and in the following decades, soluble Aβ oligomers gained increased attention as potential neurotoxic agents (Klein et al., 2001; Yankner and Lu, 2009). Addition of soluble Aβ42 to hippocampal neurons induce cell death (Lambert et al., 1998) and tau hyperphosphorylation in the absence of fibrils (Jin et al., 2011), whereas *in vivo,* microinjections of oligomeric Aβ inhibits hippocampal long-term potentiation (LTP; Walsh et al., 2002).

Whether neurotoxic species of Aβ accumulate intraneuronally has been controversial, largely due to the use of Aβ-targeting antibodies that also detect full-length APP (LaFerla et al., 2007; Gouras et al., 2010). By the use of antibodies specific for the C-terminus of Aβ42, Gouras and colleagues provided evidence that human brains accumulate intracellular Aβ42 prior to the formation of plaque and NFT formation (Gouras et al., 2000). Many subsequent indications of intraneuronal Aβ accumulation and toxicity have come from studies done on transgenic mice expressing mutated human APP (hAPP). Transgenic mice that have intracellular Aβ (iAβ) oligomers but no extracellular deposits show synaptic alterations and impaired LTP, as well as abnormally phosphorylated tau (Tomiyama et al., 2010), whereas iAβ coincides with cognitive deficits in the absence of plaque in double-transgenic mice (Knobloch et al., 2007). In mice co-expressing a total of five familial AD (FAD) mutations (5XFAD), accumulation of intracellular Aβ42 occurs before formation of plaques, and the plaques appear to originate from neuron cell bodies with iAβ (Oakley et al., 2006). In triple transgenic mice, accumulation of iAβ correlate with LTP deficits (Oddo et al., 2003) and impaired performance in the spatial reference version of the Morris water maze and inhibitory avoidance tasks (Billings et al., 2005).

Based on this evidence, there is now a considerably wide consensus that intracellular, soluble Aβ has a central role in the progression of AD. What remains unclear is how this peptide causes synaptic dysfunction, synapse loss, and cell death. Aβ accumulates during the pre-clinical stage of the disease before there is awareness of cognitive changes, which emphasises the need for focus on this early stage and the early affected brain regions.

1.1.5. Progression of pathology

Alterations associated with AD do not occur randomly or uniformly throughout the brain. Rather, the progression and distribution of both Aβ-deposition and tangle expression affect specific regions and show changing distribution patterns over time. Although AD is associated with generalised and widespread neuropathology, the earliest changes appear in the entorhinal cortex (EC) and then progress to the hippocampal formation (HF). The most prominent alterations occur in HF, EC, amygdala, cerebral association cortices, and selected subcortical nuclei (Duyckaerts et al., 2009).

In humans, tau pathology starts in the transentorhinal region and subsequently extends into the entorhinal region, HF, and the neocortex (Braak and Braak, 1985; Braak et al., 2006). Amyloid deposits first accumulate in the neocortex, and then progress to EC, HF, amygdala, and insular and cingulate cortices, before affecting subcortical areas (Thal et al., 2002). Volume loss also occurs in EC in incipient AD (Juottonen et al., 1998; deToledo-Morrell et al., 2004) and in mild cognitive impairment (MCI; (Pennanen et al., 2004), which often precedes clinical AD.

The HF and parahippocampal region (PHR), which play crucial roles in learning, memory, and spatial processing, consist of a number of interconnected regions with complex interactions. Alterations in these regions are likely the structural underpinnings of problems with declarative memory that are the first symptoms of AD. In order to investigate the pathophysiological processes of AD, it is therefore vital to have a thorough understanding of anatomy and connections in HF and PHR.

1.2. The hippocampal formation and parahippocampal region

1.2.1. Anatomy and connectivity of the hippocampal formation and parahippocampal region

This thesis will conform to the nomenclature of Insausti et al. (1997). According to this view, HF consists of the three-layered fields of Cornu Ammonis (CA1, CA2, and CA3, also known as the hippocampus proper), dentate gyrus (DG), and subiculum. PHR comprises EC, commonly divided into a medial (MEC) and lateral (LEC) part, pre- and parasubiculum (PrS and PaS, respectively), perirhinal cortex (PER), and postrhinal cortex (POR). Unlike the archicortical domains of HF, the regions of PHR have a six-layered appearance. In the rat, HF and PHR are located in caudal parts of the brain and occupy a substantial part of the total cortical surface (Figure 1.2).

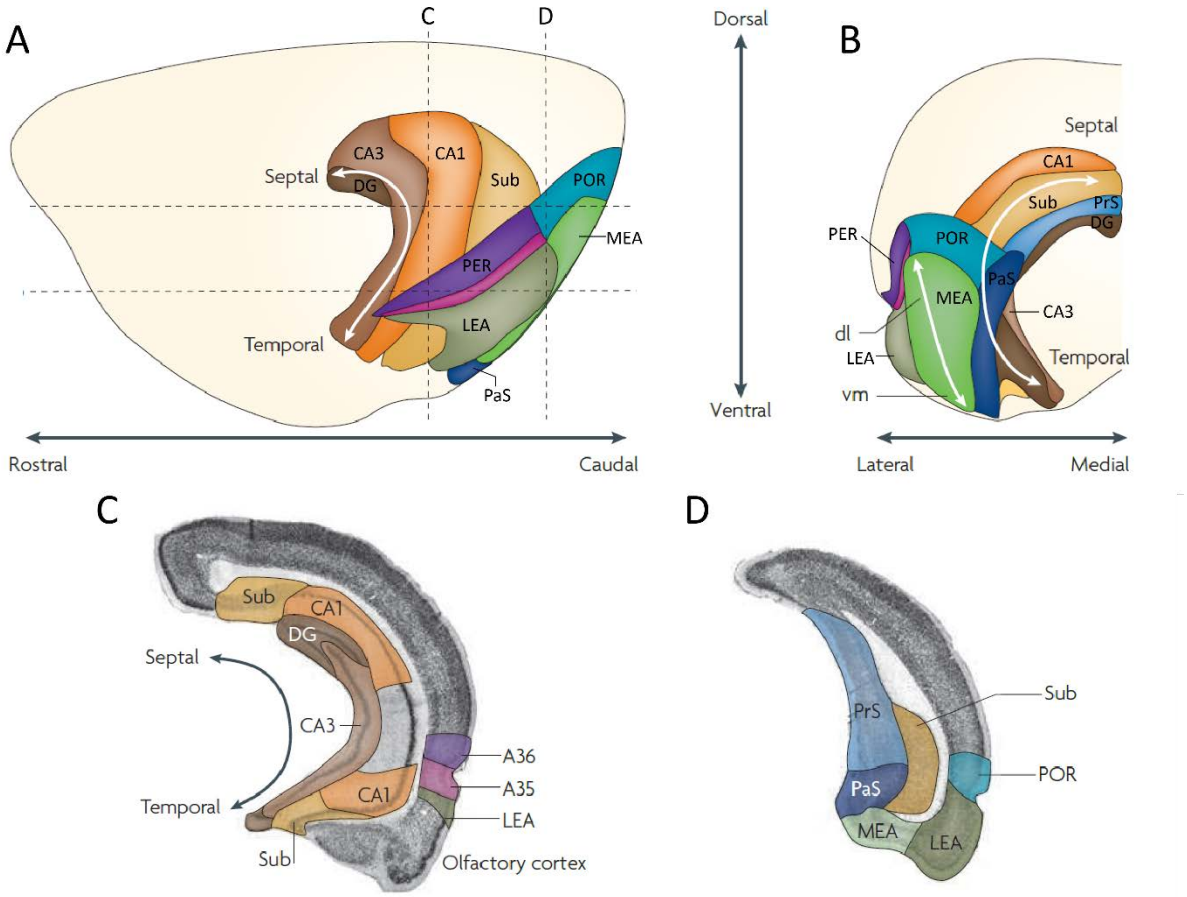

Figure 1.2. The areas of the hippocampal formation (HF) and parahippocampal region (PHR) and the main topological axes, the dorso-ventral (also called the septo-temporal), rostro-caudal, and medio-lateral, in the rat brain, shown from lateral (A) and caudal (B) views. Also shown are two coronal sections at separate rostro-caudal levels (C, D). Areas of HF include CA1, CA2 (not shown), CA3, dentate gyrus (DG), and subiculum (Sub), whereas the PHR comprises lateral entorhinal area/cortex (LEA/LEC), medial entorhinal area/cortex (MEA/LEC), presubiculum (PrS), parasubiculum (PaS), perirhinal cortex (PER) divided into Brodmann areas 35 (A35) and 36 (A36), and postrhinal cortex (POR). Figure adapted from van Strien et al., 2009.

EC forms a gateway for communication between HF and the neocortex. Cells in layers II (LII) and III (LIII) of EC are the main targets of cortical inputs, and they in turn give rise to the perforant path to all subdivisions of HF. The common view of parahippocampal-hippocampal connectivity is that there are two main projections from PHR to HF, one from POR via MEC, and the other from PER via LEC. LII of EC projects to DG and CA3, whilst LIII projects to subiculum and CA1 (van Strien et al., 2009; Witter, 2010; Figure 1.3.).

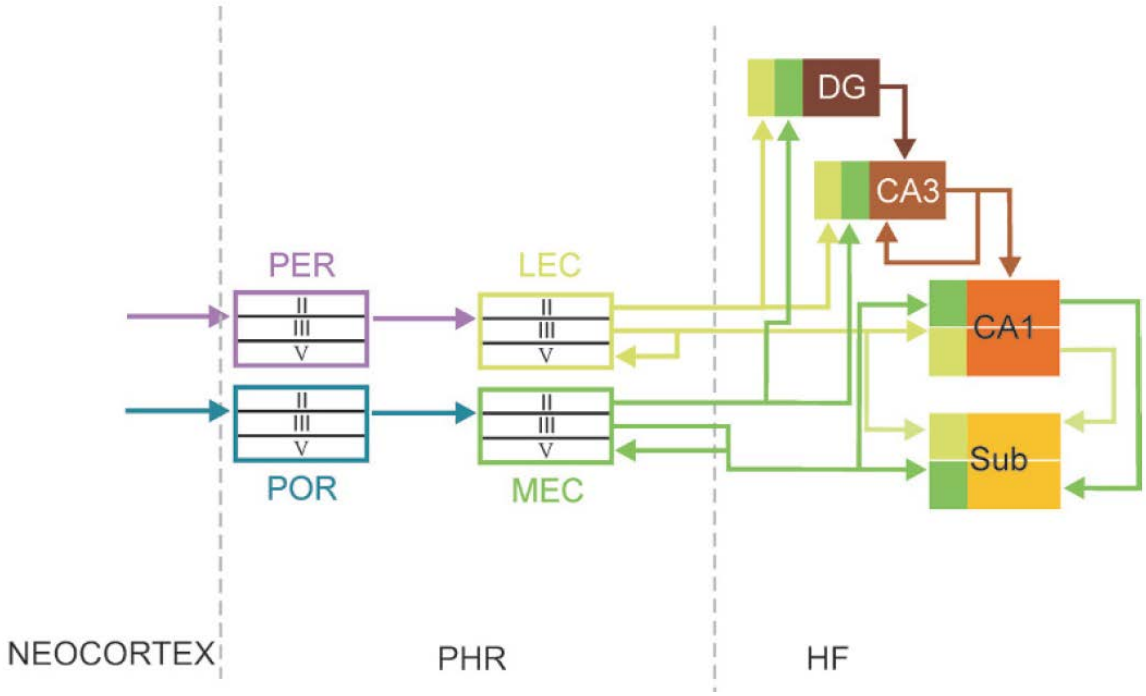

Figure 1.3. Connectivity in the entorhinal-hippocampal network. The perforant path arises from cells in layers II (LII) and III (LIII) of lateral and medial entorhinal cortex (LEC and MEC, respectively). LII projections target dentate gyrus (DG) and CA3, whereas neurons in LIII project to CA1 and subiculum (Sub). Projections from LEC and MEC target different proximal and distal locations along the hippocampal transverse axis, as indicated by light and dark green colouring. LEC and MEC receive neocortical input via perirhinal cortex (PER) and postrhinal cortex (POR), respectively. Figure taken from Witter, 2010.

The subiculum is a major source of efferent projections from the HF and has reciprocal connections with EC. It receives major input from CA1 and superficial layers of EC, and in turn sends projections to deep layers of EC which then project to the neocortex. Additionally, subiculum can bypass EC and project directly to neocortical areas as well as subcortical structures (Cappaert et al., 2015).

Projections from EC to HF are topographically organised along several axes. With regards to the dorso-ventral (septo-temporal) hippocampal axis (see Figure 1.2), lateral and posterior parts of EC are connected to the dorsal portion of HF, whereas increasingly more medial and anterior parts are connected to more ventral parts of HF. The connections to subiculum are reciprocal, so that dorsal/septal levels of subiculum preferentially project to lateral and caudal parts of EC and progressively more ventral/temporal levels project to more medially located parts of EC (Cappaert et al., 2015).

1.2.2. The hippocampal formation and parahippocampal region in Alzheimer's disease

It is widely recognised that the circuits and pathways through HF are critical for declarative memory formation, and that new memories are encoded by way of unidirectional information pass from neorcortex via PHR, to HF, back to PHR, and back to neocortex (Siegelbaum and Kandel, 2013). In most patients of AD, impairment in short-term declarative memory and the ability to retain new information are the first clinical manifestations of the disease, in line with early neuropathological changes in HF and PHR.

A severe neuronal loss is seen in EC even in very mild AD cases (Gomez-Isla et al., 1996) and atrophy and loss of neurons in LII of EC occur in individuals with MCI prior to onset of dementia (Kordower et al., 2001), which might indicate selectively vulnerable cells in this layer. The significance of EC LII will be dealt with in section 1.3.2. In transgenic mice, abnormalities in EC such as the presence of soluble Aβ40 and Aβ42, increased excitability, and increased myelin content as well as behavioural deficits first appear between two and four months of age (Duffy et al., 2015). Hypometabolism in lateral parts of EC has also been shown in pre-clinical AD and in mice models (Khan et al., 2014).

In HF, subiculum has been found to be early affected in several mouse models of amyloid pathology. In 5XFAD mice, plaques appear early in subiculum, and strong subcellular Aβ42 staining can be found within large pyramidal neurons of subiculum (Oakley et al., 2006). Lesioning the subiculum in six week old transgenic APParc mice results in reduced Aβ pathology at three and six months of age (George et al., 2014). There is selective loss of both principal cells and somatostatin-positive interneurons at an early age in subiculum in parallel with an early onset of extracellular amyloid deposits and prominent axonal damage in AβPP/PS1 mice (Trujillo-Estrada et al., 2014). Like EC, there is cell loss in areas of HF in pre-clinical AD (West et al., 2004), and extensive neuronal loss in CA1/2 has been found to correlate with strong accumulation of iAβ (Casas et al., 2004).

1.2.3. Spread of pathology in the entorhinal-hippocampal network

An interesting issue relates to whether AD pathology in certain areas initiates anatomical transmission of the disease, or if pathological changes arise independently in other areas of the brain. It has been suggested that pathology arises in EC and transsynaptically spreads to HF. Oligomeric Aβ is transferred between neurons in a manner dependent on neuritic connections (Nath et al., 2012). APP can be transported anterogradely via perforant path projections from EC to DG in rats (Buxbaum et al., 1998). Mice expressing transgene-derived APP in superficial layers of EC and pre- and parasubiculum have

high levels of soluble Aβ and Aβ deposits in perforant path terminal fields in DG (Harris et al., 2010). Correspondingly, lesions of the perforant path leads to reduced amyloid burden in the ipsilateral DG (Lazarov et al., 2002). In transgenic mice, extracellular Aβ deposits first appear in subiculum and subsequently expand to interconnected areas (Ronnback et al., 2012), similar to what has recently been described in the McGill-R-Thy1-APP rat model (Heggland et al., 2015), the subject of the present study (see section 1.4.2). Tau pathology has been found to progress from neurons in superficial layers of EC selectively expressing a human transgene in mouse models, to synaptically connected neurons in CA, subiculum, and DG not expressing the transgene (de Calignon et al., 2012; Liu et al., 2012).

1.3. Dysfunction of neurons and networks in Alzheimer's disease

1.3.1. Synapse and network dysfunction

The exact mechanisms of Aβ toxicity are unclear, but it is likely that Aβ contributes to memory dysfunctions and cognitive decline by altering synapses and neural networks. Synapses loss occurs before neuronal death in AD, and is more closely correlated with cognitive deficits (Terry et al., 1991). Transgenic mice models of AD seldom show overt loss of neurons, but they have substantial dystrophic neurites and loss of synapses, which are evident signs of neurodegeneration (Mucke and Selkoe, 2012).

It has been suggested that Aβ acts on both pre- and postsynaptic terminals and that the effect is concentration-dependent. In this view, intermediate Aβ-levels enhance presynaptic activity, whilst high levels of Aβ induce postsynaptic depression and low levels reduce presynaptic efficiency, thereby impairing synaptic activity (Palop and Mucke, 2010). Consistent with this, elevated levels of Aβ oligomers inhibit hippocampal LTP (Walsh et al., 2002) and enhance long-term depression (LTD), likely by disrupting glutamate neurotransmission and the activity of NMDA (Snyder et al., 2005; Li et al., 2009b) and AMPA receptors (Hsieh et al., 2006). Furthermore, it has been indicated that overproduction of Aβ at dendrites can reduce spine density (Wei et al., 2010).

Through its effect on synapses, Aβ could cause instability and promote synchrony of larger assemblies of neurons. AD patients have increased susceptibility to epileptic seizures (Palop and Mucke, 2009), and hyperactive neurons have been observed in transgenic mouse models (Busche et al., 2008). Both aberrant excitatory activity and compensatory inhibitory responses in memory circuits may contribute to cognitive decline. In hAPP mice with high Aβ levels, there is aberrant excitatory activity in DG associated with compensatory GABAergic activation that may serve to counteract the increase in

excitation (Palop et al., 2007). In view of the evidence summarised above, this aberrant excitatory drive may originate from LII of EC whilst the compensatory GABAergic activation points to a relevant role of interneurons, either at the level of EC or DG.

1.3.2. The importance of layer II of entorhinal cortex and reelin-expressing principal cells

LII of EC is of special interest because of its early involvement and degeneration in AD, and it still remains to be discovered what makes the cells in this layer particularly vulnerable to pathology. Principal cells and interneurons play different roles in the physiology of networks of the hippocampal-parahippocampal memory system, and this is likely the case for EC LII as well (Couey et al., 2013). Both cell types have been implicated as targets of amyloid pathology. In this section I will focus on the principal neurons in EC LII, which have diverse morphological, electrophysiological, and chemical characteristics.

LII of MEC consists of densely packed large and medium sized pyramidal and stellate cells with different morphological and electrophysiological properties (Alonso and Klink, 1993; Klink and Alonso, 1997; Canto and Witter, 2012b). For instance, a subset MEC LII principal cells function as grid cells (Hafting et al., 2005; Sargolini et al., 2006). In LII of LEC, cells tend to be clustered in 'islands'. Fan cells are the most numerous morphological type, but multiform and pyramidal neurons are also present (Canto and Witter, 2012a). The perforant path originates from most morphological cell types, though with a preference for stellate and fan cells (Schwartz and Coleman, 1981).

Cells of EC LII can be distinguished into two populations based on their molecular markers. The first is immunoreactive for the extracellular matrix glycoprotein reelin and projects to HF, whilst the other is positive for the calcium-binding protein calbindin[1] and likely projects to extra-hippocampal areas (Varga et al., 2010). In MEC, calbindin-positive cells have been estimated to account for around 40-50% of all principal cells (Varga et al., 2010; Tang et al., 2014), whereas little has been published about the distribution of calbindin and reelin in LEC.

The presence of reelin in LII principal cells is particularly interesting due to increasing evidence that reelin contributes to dysfunction associated with AD. Reelin is a large (~420 kDa) protein with an important role in layering of the cortex during development (D'Arcangelo et al., 1995). In the cortex and HF of adult rats, reelin mRNA is mainly expressed in GABAergic interneurons (Pesold et al., 1998).

[1] Calbindin includes several calcium-binding proteins. The main form has a molecular weight of 28 kDa and is referred to as calbindin-D28k. The use of 'calbindin' will hereafter refer to this isoform of the protein.

In the neocortex, reelin-immunoreactivity can be found in pyramidal cells of layer V, and, as aforementioned, reelin is also found in principal cells in LII and to a lesser extent LIII of EC. Furthermore, in DG and HF, the axons and the terminal neuropil of the entorhinal neurons appear to be heavily immunoreactive for reelin in adult rodent brains (Ramos-Moreno et al., 2006).

Numerous studies highlight the possible role of reduced reelin in amyloidosis. Reelin deficiency has been found to emerge in AD-affected human brains at early disease stages, even before the onset of amyloid pathology. In EC, a reduced proportion of reelin-positive principal cells, especially in layer II, is evident in Braak stages V-VI[2] (Herring et al., 2012). Chin et al. (2007) similarly found a decrease in reelin expression in EC LII, DG, and CA1 of hAPP mice, and fewer reelin-positive EC LII cells in human AD brains, accompanied by LTP reductions and memory impairments. Transgenic AD mice crossed with heterozygous *reeler*[3] mutants have accelerated plaque formation compared with wild type littermates, suggesting that reduced reelin levels increases Aβ levels by favouring amyloidogenic APP processing and by promoting aggregation (Kocherhans et al., 2010). In line with this, overexpression of full-length reelin has also been found to delay amyloid fibril formation in double-transgenic mice and protect against dendritic spine loss and cognitive impairment (Pujadas et al., 2014). Levels of the 180-kDa reelin fragment have been found to be increased in AD patients (Saez-Valero et al., 2003; Botella-Lopez et al., 2010), indicating altered reelin expression in AD.

Reelin binds directly to two high-affinity receptors belonging to the lipoprotein receptor superfamily, the apolipoprotein E receptor 2 (ApoER2) and the very low-density lipoprotein receptor (VldlR) (D'Arcangelo et al., 1999). In the adult brain, ApoER2 and VldlR can function as receptors for reelin to modulate synaptic plasticity by controlling calcium entry through NMDA receptors (Weeber et al., 2002; Beffert et al., 2005). There is evidence that the actions of reelin and Aβ antagonise each other at the level of the synapse. Whilst Aβ can impair LTP and enhance LTD in a concentration-dependent manner, as described above, reelin signalling at excitatory synapses can restore normal synaptic plasticity, and reelin has been found to almost completely prevent the LTP defect that is caused by AD brain extracts in wild-type hippocampal slices (Durakoglugil et al., 2009). Moreover, reelin signalling induces phosphorylation of the cytoplasmic adapter protein disabled-1 (Dab-1) in a pathway that inhibits phosphorylation of tau. Disruption of this could lead to hyperphosphorylated tau and NFT formation (Hiesberger et al., 1999). Reelin fails to form physiologically active dimers and has decreased

[2] Braak staging is a method used to classify the severity of pathophysiological changes in the brains of AD subjects. The stages, ranging from I to VI, are based on Braak and Braak's descriptions of spatiotemporal distribution and progression of NFTs in the brain.

[3] *Reeler* mouse mutants lack expression of the reelin-encoding gene, *Reln. Reeler* mice are so named because of their reeling gait, which is due to hypoplasia of the cerebellum.

binding capacity to ApoER2 in the presence of Aβ (Cuchillo-Ibanez et al., 2013). Reelin also directly interacts with soluble Aβ42 species and modifies their kinetics, and co-localises with Aβ42 in aggregated fibrils (Pujadas et al., 2014). Further, reelin immunostaining is associated with the neuritic component of Aβ plaques in APP/PS1 double-transgenic mice (Wirths et al., 2001), and reelin and APP have been found to co-localise in dendritic regions of hippocampal neurons (Hoe et al., 2009).

1.3.3. Interneurons and their role in network pathology

An increasing number of studies indicate that inhibitory interneurons are tightly related to the pathoaetiology of AD. GABAergic interneurons make up 20-30% of the cortical neuronal population and approximately 10% of the population in HF and are the main source of inhibition in the brain. Interneurons are involved in maintaining stable states in assemblies of neurons and regulate synaptic signalling of principal cells, and loss of this regulation could contribute to destabilisation of neural networks.

Early studies indicated that interneurons were resistant to Aβ-induced toxicity. No significant loss of GABAergic cells was observed after treatment with aggregated Aβ in long-term mixed cultures consisting of hippocampal neurons, despite significant neuronal loss (Pike and Cotman, 1993). However, later studies found that GABAergic neurons are vulnerable to Aβ42 toxicity and AD pathology. Aβ42-positive neurons with small and round somata have been identified in LII-IV of the cortex in human AD subjects (Mochizuki et al., 2000). GABAergic neurons are degenerated in HF (Krantic et al., 2012; Loreth et al., 2012) and EC (Moreno-Gonzalez et al., 2009) of transgenic mice. Further, transgenic hAPP mice express spontaneous non-conclusive seizure activity in cortex and HF, and dysfunction in parvalbumin-positive interneurons has been found to lead to abnormal network activity and memory impairments in these mice (Verret et al., 2012). Directly related to their potential role in clinical manifestations of AD, transplanting inhibitory interneuron progenitors to hilus of HF restores normal learning and memory in transgenic mice with interneuron loss (Tong et al., 2014).

1.3.4. Selective vulnerability of interneuron subsets

Interneurons are incredibly diverse in their chemical profiles, and subtypes can generally be distinguished based on the presence of neuropeptides, such as somatostatin, or calcium-binding proteins, including calbindin, calretinin, and parvalbumin (Freund and Buzsaki, 1996). Whether calcium-binding proteins protect against or trigger pathological changes is still undetermined. Several studies have indicated the resistance of calcium-binding protein-expressing neurons in AD. For

instance, iAβ accumulation occurs primarily in calcium-binding protein-deficient neurons in 5XFAD mice (Moon et al., 2012). GABAergic calbindin-positive interneurons in layers II-IIIa of the prefrontal cortex were resistant to degeneration and NFT pathology, whereas pyramidal cells were more vulnerable (Hof and Morrison, 1991). Calbindin-positive cells have also been found not to contain tangles in HF in human AD subjects (Iritani et al., 2001). On the other hand, calbindin-reactivity is reduced in DG of APP/PS1 mice (Popovic et al., 2008), and calbindin-positive interneurons are earlier and more severely affected than calretinin-positive interneurons in EC of human AD brains (Mikkonen et al., 1999). Levels of parvalbumin-positive interneurons have been found to be reduced in HF of human AD brains (Brady and Mufson, 1997), and in APP/PS1 transgenic mice, paralleling the accumulation of iAβ (Takahashi et al., 2010). Parvalbumin-expression is also reduced in DG of APP/PS1 mice (Popovic et al., 2008). Calretinin-positive neocortical neurons have been found to be resistant to the degenerative processes of AD (Hof et al., 1993), and to be less affected by pathology in EC of human AD brains compared to calbindin- and parvalbumin-positive interneurons (Mikkonen et al., 1999). However, levels of calretinin are reduced in HF of APP/PS1 mice (Popovic et al., 2008; Takahashi et al., 2010), and calretinin-positive interneurons are reduced at an early age in CA1-3 of APP/PS1 mice despite hippocampal interneurons in this model not expressing mutated hAPP (Baglietto-Vargas et al., 2010). Similarly, in the piriform cortex and LEC, calretinin-positive cells show an early decrease in transgenic APP/PS1 mice (Saiz-Sanchez et al., 2012).

Unlike calcium-binding proteins, the involvement of somatostatin in AD seems to be less dubious, although not many studies have looked into the matter. Somatostatin shows reduction and a high degree of co-localisation with Aβ deposits in LEC and piriform cortex of APP/PS1 mice (Saiz-Sanchez et al., 2012). Co-localisation of somatostatin with Aβ deposits has also been found in the anterior olfactory nucleus of human AD brains (Saiz-Sanchez et al., 2010). Later results from the same group indicated preferential vulnerability of somatostatin cells that co-localised with Aβ in piriform cortex of human AD-subjects. (Saiz-Sanchez et al., 2014). This is in accordance with earlier observations of decreased somatostatin-positive cells in HF of PS1/APP mice (Ramos et al., 2006).

1.4. Modelling Alzheimer's disease in transgenic animals

1.4.1 Genetics and animal models of Alzheimer's disease

Genetically modified animals offer unique opportunities to understand pathogenic mechanisms. The majority of AD animal research has traditionally been done on transgenic mice expressing one or several mutations involved in FAD, more specifically in the *APP* gene or in the two presenilin genes (*PS1* and *PS2*), which encode parts of the γ-secretase complex. Although they show Aβ pathology with various degrees of severity and cognitive deficits in different behavioural test paradigms, APP and presenilin mice models have little cell loss. However, evidence for progressive synaptic dysfunction and degeneration has been found in several of these models (McGowan et al., 2006).

Autosomal-dominant mutations such as mutations in *APP* and *PS1*/*PS2* are estimated to account for less than 5% of AD cases, whereas the majority of AD cases are sporadic and have unknown, and likely complex, causes (Tanzi and Bertram, 2005). Presence of the ε4 allele of the apolipoprotein E gene (*APOE*) increases the risk of developing sporadic, late-onset AD (Schmechel et al., 1993). Class E apolipoproteins are involved in transporting lipids throughout the circulatory systems, and several mouse models with *AOPEε4* and *APOE*-related mutations have been developed (Herz and Beffert, 2000). Despite the fact that no known tau mutations cause FAD, mouse models with mutations in the tau gene, *MAPT* (microtubule-associated protein tau), that show robust NFT pathology have been created, several of which show significant neuronal loss (McGowan et al., 2006).

Rats are the most commonly used species for modelling several neurological diseases, such as Parkinson's disease and ischaemic stroke (Cenci et al., 2002), but their use in AD research has been lacking. Transgenic rats are more difficult to develop than mice, but they are considered superior to mice as disease models due to their larger size and the fact that they in many aspects are more similar to humans (Tesson et al., 2005; Do Carmo and Cuello, 2013). For instance, mice have accelerated postnatal brain development compared to rats, and rats, like humans, thus have increased number of and more complex synapses (Whishaw et al., 2001).

Early transgenic rat models of AD were considered inferior as model systems as they did not display cell loss, plaques, or NFTs, but only accumulation of iAβ. Some of these did nonetheless have cognitive deficits along with LTP dysfunction, supporting the notion that these features are dependent on soluble Aβ rather than insoluble fibrils (Do Carmo and Cuello, 2013). Flood et al. (2009) reported the development of one of the first transgenic rat models of AD with extracellular amyloid deposits (Flood

et al., 2009). This model had a triple transgenic construct, likely making it more susceptible to kidney diseases, immunosuppression, and premature death (Zahorsky-Reeves et al., 2007). In 2013, a rat model expressing mutant *APP* and *PS1* and showing complete AD-like pathology with intraneuronal Aβ42-expression, progressive deposition of Aβ plaques, NFTs, and neuronal loss was developed (Cohen et al., 2013). The relatively newly developed McGill-R-Thy1-APP rat model is so far one of the few, if not the only, rat model that reproduces full AD-like amyloid pathology whilst expressing only a single transgene (Leon et al., 2010). This rat model is the subject of the present study.

1.4.2. The McGill-R-Thy1-APP rat model

The McGill-R-Thy1-APP rat model of AD expresses a single transgene coding for a modified variant of the human $A\beta PP_{751}$ protein with the co-expression of the Swedish and Indiana mutations. The Swedish double mutation causes a double amino acid change that leads to cleavage of APP by BACE-1, whereas the Indiana mutation increases the ratio of Aβ42 to Aβ40. Both mutations are under the control of the murine *Thy*1.2 promoter, making expression of the transgene highly restricted to neurons. The model shows progressive AD-like amyloid pathology, including accumulation of iAβ from one week postnatal in homo- and hemizygous animals and extracellular dense amyloid deposits in homozygous animals as young as six months (Leon et al., 2010). Amyloid plaque pathology appears to progress between anatomically connected areas and is heaviest in HF and PHR, with dorsal subiculum being the earliest and most severely affected region (Heggland et al., 2015). The model exhibits cognitive deficits and impaired LTP at a stage when no extracellular Aβ depositions but only iAβ is present (Leon et al., 2010; Qi et al., 2014). Hemizygous McGill-R-Thy1-APP rats, which only have sparse plaque pathology (Heggland et al., 2015), but display iAβ in HF and cortex at three, six, and 12 months of age, have been shown to have both working memory and spatial reference memory deficits as early as three months when compared to wild-type controls (Galeano et al., 2014).

The progression of Aβ pathology, which follows a spatiotemporal pattern of expression similar to humans, makes the McGill-R-Thy1-APP rat a good model for studying early pathological mechanisms in AD. In particular, the fact that iAβ accumulates at early ages and correlates with cognitive deficits, makes the McGill-R-Thy1-APP rat a useful tool for investigating which cells express iAβ. To date, no report on amyloid pathology in interneurons in the McGil-R-Thy1-APP rat model has been published.

1.5. Aims

Amyloid pathology shows a characteristic spatiotemporal progression throughout the brain, both in human AD subjects and the McGill-R-Thy1-APP rat model, with areas of the HF and PHR being early and heavily affected. What makes these areas particularly vulnerable is currently unknown. By the time the clinical symptoms of AD start to manifest, the neuropathological changes in the brain are severe, and it is thus vital to identify cell types that are selectively vulnerable to early pathology. With use of the transgenic McGill-R-Thy1-APP rat model, this thesis aims to characterise whether neuronal populations that are selectively vulnerable to accumulation of iAβ in the pre-plaque stage of AD are characterised by the presence of distinct molecular markers. Since neurons in LII of EC are among the earliest and heaviest affected areas in AD, and the subpopulation of DG-projecting neurons are characterised by a the presence of the glycoprotein reelin, the first aim is to establish whether reelin-expressing principal cells in LII of EC are more susceptible to the accumulation of iAβ than neighbouring cell populations. Further, with regards to the importance of interneurons in network dysfunctions, the aim of the second part of this thesis is to investigate whether iAβ is also expressed in interneurons in early stages of disease in the McGill-R-Thy1-APP rat model. Focus will be on areas of PHR and HF, with a particular focus on subiculum due to its reciprocal connections with EC and the early amyloid pathology in this area.

2. MATERIALS AND METHODS

Lists of antibodies and chemicals can be found in Appendix A, recipes for solutions can be found in Appendix B, and a detailed list of animals used for all experiments can be found in Appendix D.

2.1. Animals

2.1.1. Housing and breeding

All housing and breeding of animals was approved by the Norwegian Animal Research Authority and was in accordance with the Norwegian Animal Welfare Act §§ 1 – 28, the Norwegian Regulations on Animal Research §§ 1- 26, and The European Convention for the Protection of Vertebrate Animals used for Experimental and Other Scientific Purposes.

Transgenic McGill-R-Thy1-APP rats were used for all parts of this thesis. Animals were housed and bred at the Kavli Institute for Systems Neuroscience and the Centre for Neural Computation at the Norwegian University of Science and Technology (NTNU; Trondheim, Norway). Two breeding pairs from McGill University, Montreal, Canada (Leon et al., 2010) were the basis for the transgenic colony. The animals were kept on a 12 hour light/dark cycle under standard laboratory conditions (19-22 ˚C, 50-60% air humidity) with access to food and water *ad libitum.* Breeding was conducted in cages with one adult male and one or two adult females. Pups were housed with the parents or in some cases only with the mother until weaned on postnatal day 21, when they were separated and placed in cages with one to three littermates of the same sex.

Littermates negative for the transgene were used as controls in most cases, but as there were not enough negative littermates available for all age groups, wild-type Wistar rats (WistarHan from Taconic, Hudson, NY, USA and Charles River Laboratories International, Wilmington, MA, USA) were used as additional controls.

2.1.2. Genotyping

Ear tissue for genotyping was taken from each rat prior to perfusion. The procedure for genotyping followed that described in detail recently (Heggland et al., 2015). Briefly, genotyping for expression of

the transgene was done by quantitative PCR (qPCR) with a High Pure PCR Template Preparation Kit (Roche Diagnostics, Basel, Switzerland). Genomic DNA was isolated from ear tissue, and RT^2 qPCR Primer Assays (Qiagen, Venlo, Netherlands) were used to detect human AβPP and a normalisation gene (GAPDH or beta-actin) with FastStart Universal SYBR Green Master (Roche Diagnostics, Basel, Switzerland) on an Applied Biosystems StepOnePlus real-time PCR system (Life Technologies Ltd., Thermo Fisher Scientific, Waltham, MA, USA). $\Delta\Delta C_T$ values were calculated with a known homozygous sample as reference (Livak and Schmittgen, 2001).

2.2. Histology

2.2.1. Transcardial perfusion

Immediately prior to perfusion, rats were weighted in order to determine the dose of anaesthetics that needed to be given. Rats were sedated in chambers containing 5% isoflurane gas before being deeply anaesthetised with pentobarbital injected intraperitoneally (approximately 0.2 mL/100 g). The animals were checked for absence of pain responses and reflexes. Perfusion was done using a Peri-Star Pro 4-channel low rate pump (World Precision Instruments Inc., USA) with Ringer's solution (3.35 mM KCl, 145 mM NaCl, 2.28 mM $NaHCO_3$, pH 6.9) to remove blood content followed by a 4% solution of freshly depolymerised paraformaldehyde (Merck kGaA, Darmstadt, Germany) in 125 mM phosphate buffer (PB; pH 7.4; PFA) to facilitate post-fixation.

The brains were removed and post-fixed in PFA for approximately 24 hours (or longer if needed) before being transferred to 2% dimethyl sulfoxide (DMSO; VWR International, Radnor, PA, USA) in 125 mM phosphate buffer (PB) and 20% glycerol for cryoprotection. Brains were stored at 4 ˚C for at least 24 hours before sectioning.

2.2.2. Cutting and storage

Brains were cut into 40 µm coronal sections using a freezing microtome (Microm HM430, Thermo Fisher Scientific, Waltham, MA, USA) set at approximately -40 ˚C. The caudal side of the brain was attached to the microtome with a 30% sucrose solution. The brain was covered with pulverised dry ice to keep it frozen during cutting. The sections were stored as six separate series, making the sections in each series 240 µm apart. Cut sections were kept in DMSO/glycerol at -23 ˚C until they were used for immunohistochemical staining.

2.2.3. Immunohistochemistry

To identify neurons expressing intracellular amyloid β (iAβ), sections were double- or triple-labelled for iAβ and reelin, calbindin, glutamate decarboxylase 67-kDa (GAD67), parvalbumin, or somatostatin according to standard immunohistochemistry protocols. All immunohistochemical procedures were performed on free-floating sections and conducted at room temperature unless otherwise stated. One randomly chosen series of sections from each brain was used.

In most protocols used, sections were first subjected to heat-induced epitope retrieval (HIER) in 125 mM phosphate buffer (PB) for 2 or 3 hours at 60 ˚C. Next, the sections were washed 1 x 10 minutes in PB, permeabilised with 0.5% Triton X-100 (Merck kGaA, Darmstadt, Germany) in PB (PBT; 3 x 10 minutes), and blocked with 5 or 10% normal goat serum (NGS; Abcam, Cambridge, UK) in PBT for 2 hours before being incubated with the primary antibodies in PBT (with or without 5% NGS) overnight or for 48 hours at 4 ˚C. In the case of somatostatin, normal donkey serum (Sigma-Aldrich, St. Louis, MO, USA) was used as blocking medium instead of NGS.

After incubation, sections were washed 3 x 10 minutes in PBT and incubated with secondary antibodies in PBT (with or without 5% NGS) for 2 hours in room temperature or overnight at 4 ˚C. For immunofluorescence, sections were finally washed 3 x 10 minutes in PB. For peroxidase/3,3'-diaminobenzidine (DAB) staining, sections were washed 3 x 10 minutes in PBT and incubated with avidin-biotin complex (ABC; Vectastain ABC kit, Vector Laboratories, Burlingame, CA, USA) for 90 minutes. Subsequently, the tissue was washed 3 x 10 minutes in PBT and 2 x 5 minutes in 50 mM Tris (Merck KGaA, Darmstadt, Germany) adjusted to pH 7.6 with HCl (Tris-HCl) before being incubated with 0.67% DAB (Sigma-Aldrich, St. Louis, MO, USA) and 0.024% H_2O_2 for 30 minutes.

Sections were washed 2 x 5 or 1 x 10 minutes in Tris-HCl before being mounted on glass slides from Tris-HCl with 0.2% gelatine (Oxoid Ltd., Basingstoke, UK) and left to dry overnight on a 30 ˚C heating plate. Finally, sections were coverslipped with Toluene (VWR International, Radnor, PA, USA) and Entellan (Merck kGaA, Darmstadt, Germany) and dried overnight.

Double-stainings for calbindin and iAβ or reelin and for iAβ and somatostatin were done sequentially, in which cases sections were washed 3 x 10 minutes in PB and 3 x 10 minutes in PBT between incubation with the first secondary antibody and the second primary antibody.

See Appendix C for all immunohistochemistry protocols.

2.3. Stereological estimation of intracellular amyloid β- and reelin-immunoreactive cells in layer II of entorhinal cortex

20 homozygous McGill-R-Thy1-APP transgenic rats, 14 males and six females, were used to investigate the expression of iAβ in reelin-positive cells in layer II (LII) of entorhinal cortex (EC). The rats were divided into four age groups: postnatal day 15 (P15), one month, three months, and six months, with five animals per group. Cells were immunohistochemically double-labelled using a polyclonal rabbit antibody against reelin (Biorbyt, Cambridge, UK) and a monoclonal mouse antibody against human Aβ (McSA1; MédiMabs, Montreal, Canada). Stained sections were analysed using a Zeiss Axio Imager.M1 microscope (Carl Zeiss, Jena, Germany) connected to a CX9000 camera (MBF Bioscience, Williston, VT, USA). Reelin-positive cells labelled with Alexa fluorophore 488 were visualised with a BP 450-490 filter, and iAβ-positive cells stained with Alexa fluorophore 546 with a BP 546/12 filter. The number of cells immunoreactive for reelin, iAβ, or both were counted and the total numbers estimated by unbiased stereology, also known as design-based stereology, using the Optical Fractionator method. The project was carried out in collaboration with PhD student Asgeir Kobro-Flatmoen, who did the stereological estimations of a few of the brains.

2.3.1. Delineating layer II of entorhinal cortex

The region of interest (ROI) must be defined before estimating the number of cells with the Optical Fractionator. The boundaries of EC LII were delineated throughout the entire rostrocaudal extent in the commercial software Stereo Investigator 10 (MBF Bioscience, MicroBrightField Inc., Williston, VT, USA) using dark field and a Plan-Apochromat 5x objective (NA 0.16). Delineations were done in accordance with *The Rat Hippocampus Atlas* (Kjonigsen et al., 2011). We separated EC into lateral and medial entorhinal cortex (LEC and MEC, respectively), but no further subdivisions were made.

Briefly, the rostral border of LEC was considered to emerge at approximately the same level as ventral hippocampus emerges. At this level, LEC is distinguished from the dorsally bordering perirhinal cortex by its much larger LII cells that occasionally extend into the relatively cell-free layer I. More caudally, LEC is separated from postrhinal cortex by the same criterion. LEC is separated from the ventrally bordering piriform cortex by its six-layered structure. Caudally, LEC gradually occupies more of the dorsoventral extent and eventually comes to border MEC roughly as the posteromedial cortical amygdaloid nucleus disappears. LEC and MEC are distinguishable by LEC having a narrower layer I, and cells of LEC LII being more densely distributed. Additionally, large pyramidal cells are present throughout the entire layer V of LEC, whereas in MEC they are only located in superficial layer V.

Rostrally, MEC is distinguishable from the dorsally bordering ventral subiculum by its six layers, whereas more caudally, MEC is separated from parasubiculum by its characteristically club-shaped LII.

2.3.2. Cell counts and the Optical Fractionator

Counting of cells was performed using a Plan-Apochromat 100x oil immersion objective (NA 1.4). The right hemisphere was always used for counting unless it was missing or severely damaged, in which case the left hemisphere was used instead. If both left and right EC or entire sections were missing, damaged, or destroyed, the section was registered as 'missing' and taken into account in the subsequent analysis. Confocal images were taken after counting and consequent bleaching of EC of the right hemisphere. Figures in the results section therefore show the left hemisphere; however, the brains are the same as the ones used for stereology.

The Optical Fractionator method estimates the total cell number from a systematically randomly sampled (SRS) number of cells. The stereological estimate is unbiased and systematic errors in the calculations are eliminated as counts are not influenced by cell size, shape, spatial orientation, or spatial distribution (Gundersen, 1986). The steps for the Optical Fractionator are shown in Figure 2.1.

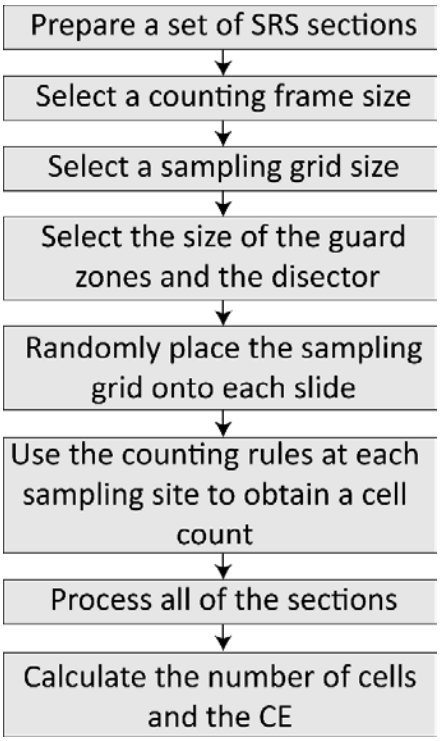

Figure 2.1. Steps for the Optical Fractionator method. SRS: systematically randomly sampled; CE: coefficient of error. Adapted from stereology.info.

A virtual grid is placed randomly on each pre-defined ROI. Then, a set of unbiased, virtual counting spaces are superimposed on the grid with uniform distance in X,Y directions after random placement of the first counting frame. The counting frames are shown as red and green square probes that consist of two inclusion lines and two exclusion lines (Figure 2.2) and a defined height in the Z axis. The height of the frames was set to 10 µm in order to leave guard zones, so that the cell number would not be underestimated as a result of lost cells near the upper and lower borders of the sections (Andersen and Gundersen, 1999).

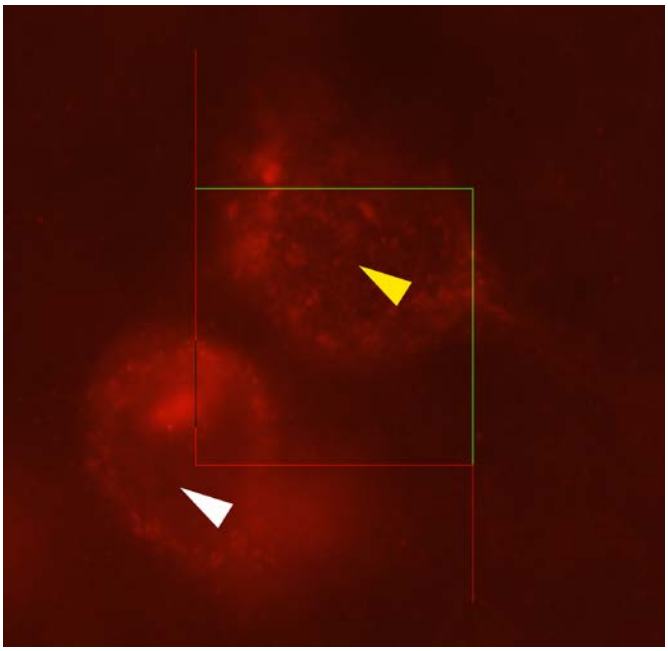

Figure 2.2. Example of counting frame showing one included cell (yellow arrow) and one excluded cell (white arrow). Neurons were counted if their middle point was within the counting frame or crossed the inclusion lines (green) from either inside or outside the frame, and not counted if their middle crossed the exclusion lines (red) or was outside the counting frame.

For LEC, we used counting frames of 400 µm^2 (20 µm x 20 µm) applied mostly to a 16,900 µm^2 (130 µm x 130 µm) grid, whereas the counting frames for MEC were 400 µm^2 (20 µm x 20 µm) applied to a 25,600 µm^2 (160 µm x 160 µm) grid. To compensate for the seemingly lower cell number in some the youngest animals (P15 group), we adjusted the grid size to 14,400 µm^2 (120 µm x 120 µm) for LEC and 22,500 µm^2 (150 µm x 150 µm) for MEC for three brains. These parameters were also applied when counting three brains in the one month group and one brain in the six month group, as these were uncounted at the time we changed the parameters. In addition, the grid spacing for two other six months old brains were 19,600 µm^2 (140 µm x 140 µm) and 32,400 µm^2 (180 µm x 180 µm), respectively, as these were used to optimise the grid and counting frame sizes.

The thickness of the section was measured at each counting frame by first bringing the top into focus and then moving through the Z axis until the cells were out of focus. The middle of the cell was set as the unique, identifiable point, and cells were counted if this point was in focus and was within the counting frame or crossed the inclusion lines from either inside or outside the frame. Cells whose middle point crossed the exclusion lines or that were outside the counting frame were not included (Figure 2.1). To avoid bias, cells that were Aβ-positive were marked first. Subsequently, the cells were checked for presence of reelin-immunoreactivity. A cell was considered positive for either reelin or iAβ when a cell body with dense cytoplasm was clearly distinguishable from the background. The proteins were considered to co-localise when a cell shape and cytoplasm could clearly be seen with both stains in the same Z-plane.

2.3.3. Estimation of total number of cells and analysis

The estimated number of cells positive for both reelin and iAβ (i.e., co-localised cells) in LEC and MEC was calculated based on the Optical Fractionator counts by Stereo Investigator. We used the reported 'estimated total by number weighted section thickness'. The Optical Fractionator estimates the total number of particles (N) as

$$N = \sum Q^{-} \cdot \frac{t}{h} \cdot \frac{1}{asf} \cdot \frac{1}{ssf}$$

where Q^{-} is the number of counted particles, *t* is the section thickness, *h* is the counting frame height, *asf* is the area sampling fraction, and *ssf* is the section sampling fraction.

The accuracy of an estimate in stereological sampling can be measured by the coefficient of error (CE). The CE describes the contribution of methodological variance to the estimate. We set the desired CE to 0.1, and for this level of accuracy it is recommended to count at least 100 cells in each ROI (West et al., 1991). The smoothness factor, *m*, was set as 1 as this is considered most suitable for biological samples (Gundersen et al., 1999).

CE is defined as

$$CE = \frac{\sqrt{TotalVar}}{s^2}$$

where s^2 is the variance due to noise (variability within sections, also known as the nugget effect), defined as

$$s^2 = \sum_{i=1}^{n} Q^-$$

TotalVar is the total variance, or

$$TotalVar = s^2 + VAR_{SRS}$$

where VAR_{SRS} is the variance due to systematic random sampling (intersection variability):

$$VAR_{SRS} = \frac{3(A - s^2) - 4B + c}{240}$$

where

$$A = \sum_{i=1}^{n} (Q_i^-)^2, B = \sum_{i=1}^{n-1} Q_i^- Q_{i+1}^-, C = \sum_{i=1}^{n-2} Q_i^- Q_{i+2}^-$$

The observed coefficient of variation (CV) among animals in each age group was calculated as SD/mean. The ratio CE^2/CV^2 was calculated to determine the contribution of the methodological variance to the total variance.

2.3.4. Mouse anti-reelin and MOAB-2 immunohistochemistry

To ensure the specificity of the rabbit anti-reelin antibody, sections from age groups P15, one month, three months, and six months were double-labelled using rabbit anti-reelin and the well-characterised G10 clone of a monoclonal mouse anti-reelin-antibody (Merck Millipore, Merck kGaA, Darmstadt, Germany).

MOAB-2 (Biosensis, Thebarton, SA, Australia), a monoclonal mouse antibody specific for Aβ40/42, was tested as a potential alternative to McSA1. Several variations were tested in order to optimise the protocol; these are all listed in Appendix G together with the results of the tests.

2.3.5. Checks for spectral bleed-through in the fluorescent microscope

The BP 450-490 and BP 546/12 filters used to visualise iAβ and reelin, respectively, showed remarkably similar labelling in the fluorescent microscope, whereas in the confocal microscope, the co-localisation did not seem to be complete. To check whether the BP 450-490 filter used to visualise Alexa fluorophore 488 (reelin) also produced excitation of Alexa fluorophore 546, additional images using a BP 470/40 and a BP 475/40 filter were taken. Control images of section single-labelled with McSA1 and Alexa fluorophore 546 and excited using the BP 450-490 filter were also taken.

2.4. Intracellular amyloid β in calbindin-immunoreactive cells in layer II of entorhinal cortex

The expression of iAβ in calbindin-immunoreactive cells of EC LII was investigated by double-immunohistochemical labelling using McSA1 and a polyclonal rabbit anti-calbindin antibody (Swant, Marly, Switzerland) in tissue from one, three, and six month old homozygous McGill-R-Thy1-APP rats. As an additional control and to look for potential co-localisation between reelin and calbindin in EC LII, sections from a six month old animal were double-labelled with the rabbit anti-calbindin and mouse anti-reelin antibodies.

2.5. Analysis of intracellular amyloid β in interneurons

To determine whether interneurons express iAβ in the McGill-R-Thy1-APP rat model, sections were immunohistochemically double-stained for Aβ and GAD67, a marker for GABAergic cells, using McSA1 and a monoclonal mouse antibody against GAD67 (Merck Millipore, Merck kGaA, Darmstadt, Germany). The secondary antibodies were goat anti-mouse IgG1 Alexa fluorophore 555 and goat anti-mouse IgG2a Alexa fluorophore 647 (Invitrogen, ThermoFisher Scientific, Waltham, MA, USA) for McSA1 and GAD67, respectively. After establishing the protocols, 10 rats, five males and five females, were used to investigate the proportion of iAβ-positive interneurons in dorsal, ventral, and intermediate subiculum. Rats were divided into the age groups one month and six months, with five animals per group. Two brains from P15 rats and two brains from three month old rats were stained with the same antibodies in order to investigate and describe the pattern of iAβ in interneurons in the hippocampal formation and parahippocampal region at these ages.

2.5.1. Fluorescent scanning

The analysis of iAβ-positive interneurons was performed using scanned images instead of live imaging of the sections due to the use of Alexa fluorophore 647 to label GAD67-positive cells. Stained sections were scanned using a MIRAX Midi BF/FL v 1.12 fluorescent digital slide scanner (Carl Zeiss, Jena, Germany) equipped with a Plan-Apochromat 20x objective (NA 0.8), a HXP 120 illuminator, and an AxioCam MRm Rev. 3 camera. A BP 545/25 filter was used to visualise Alexa fluorophore 546/555 and a BP 640/30 filter to visualise Alexa fluorophore 647.

Fluorescent scanning was also used for visualisation and digital storage of immunostained sections that were not used for counting. For sections stained with Alexa fluorophore 488, a BP 470/40 filter was used for visualisation.

2.5.2. Delineating subiculum

The scanned sections were viewed using the software Pannoramic Viewer (3DHISTECH Ltd., Budapest, Hungary). Annotated ROIs were exported as TIF files and opened and processed in Neurolucida 11 (MBF Bioscience, MicroBrightField Inc., Williston, VT, USA). Images of the two stains were exported as separate files and subsequently overlaid in Neurolucida.

As for EC LII, subiculum was delineated according to *The Rat Hippocampus Atlas* (Kjonigsen et al., 2011). Subiculum was separated into a dorsal, ventral, and intermediate part. Throughout the entire rostrocaudal axis, both dorsal and ventral subiculum can easily be separated from the bordering CA1 and presubiculum due to its wide pyramidal layer with less densely packed pyramidal cells. When MEC emerges, it can be distinguished from ventral subiculum by having six layers as opposed to three.

The delineations were performed in Neurolucida using a combination of the GAD67 stain and the McSA1 stain. As the McSA1 antibody shows strong staining of subicular pyramidal layer cells that follows the cytoarchitectonic features of subiculum and the adjacent regions it was not found necessary to delineate in dark field or using Nissl stained sections.

2.5.3. Cell counts and inclusion criteria

Cells were counted using Neurolucida by the placement of markers; one set of markers was used to plot cells that stained positive for GAD67 and another for cells that stained positive for both GAD67

and iAβ. Cell that were only positive for iAβ were not included. The GAD67 antibody strongly stains neuropil in addition to cell somas, and it was occasionally problematic to distinguish the two. A cell was counted as positive for GAD67 or iAβ if the contour of a cell body with densely labelled cytoplasm could clearly be seen. As counting was done using two-dimensional pictures, cells were included even if they were slightly out of focus as long as the above criteria were met, to get a more precise estimate of total cell number.

2.5.4. Statistical analysis

Differences in proportions of iAβ-positive interneurons between dorsal, ventral, and intermediate subiculum in age groups one and six months were tested using a two-way analysis of variance (ANOVA). The data was modelled as a mixed linear model with post-hoc Bonferroni comparisons after testing for normality and homogeneity of variances. The results were considered statistically significant when $P < 0.05$. Statistical analyses were done using R 2.14.1 (R Foundation for Statistical Computing, Vienna, Austria), SPSS version 21.0 (IBM SPSS Statistics, IBM Corp., Armonk, NY, USA), and Minitab Statistical Software version 17.1 (Minitab, State College, PA, USA).

2.5.5. Parvalbumin and somatostatin

To see whether iAβ is expressed in specific subsets of interneurons in the McGill-R-Thy1-APP rat model, section from a six month old homozygous rat were double-immunohistochemically labelled for iAβ and somatostatin using McSA1 and a polyclonal goat antibody for somatostatin (Santa Cruz Biotechnology, Inc., Dallas, TX, USA). In addition, sections from a three month old animal were triple-labelled using McSA1, mouse anti-GAD67, and a polyclonal rabbit anti-parvalbumin antibody (Swant, Marly, Switzerland).

2.6. Confocal microscopy

To confirm co-localisation in the Z-plane and to obtain high-resolution images, immunostained sections were scanned with an Axio.Imager Z1 confocal microscope (LSM 510; Carl Zeiss, Jena, Germany) using a Plan-Apochromat 20x objective (NA 0.8), a Plan-Apochromat 40x objective (NA 0.95), and a Plan-Apochromat 40x oil immersion objective (NA 1.3). A DPSS 561-10 laser was used for exciting Alexa fluorophore 546/555, a HeNe 633 laser for Alexa fluorophore 647, and an Argon 488 laser for

Alexa fluorophore 488. The filters used for detection were BP 505-550, BP 575-615, and LP 650 for Alexa fluorophores 488, 546/555, and 647, respectively.

2.7. Image processing

Images were processed using ImageJ 1.48V (Rasband W, National Institutes of Health, Bethesda, MD, USA) and Adobe Photoshop CS6 (Adobe Systems Inc., San Jose, CA, USA). Adobe Illustrator CS6 (Adobe Systems Inc., San Jose, CA, USA) was used to make figures.

3. RESULTS

3.1. Intracellular amyloid β in the McGill-R-Thy-1-APP rat model

This thesis focuses on the pre-plaque stage in the McGill-R-Thy1-APP rat model of Alzheimer's disease (AD) and investigates cells in the hippocampal formation (HF) and parahippocampal region (PHR) that express intracellular amyloid β (iAβ) at ages postnatal day 15 (P15), one month, three months, and six months in homozygous rats. The expression of iAβ at these ages and at 18 months is illustrated in Figure 3.1. There is a substantial amount of iAβ in many parts of the brain already at P15 (Figure 3.1 A), and iAβ has previously been found at one week postnatal in this rat model (Leon et al., 2010). Tissue from a P6 rat was stained with McSA1, which confirmed that iAβ was indeed present at this early age (data not shown). The level of iAβ in the brain appears to increase from P15 to one month, after which it remains steadily high at least until six months (Figure 3.1 B-D). The areas with the strongest labelling include subiculum, the pyramidal layer of CA1 and CA3, layer II of entorhinal cortex (EC), retrosplenial cortex, and piriform cortex (Figure 3.1 A-D; see also Heggland et al., 2015). The first amyloid plaques appear at approximately nine months in rats from our colony, and at 18 months there is a substantial amount of plaques in areas of HF and PHR (Figure 3.1 E). At later ages, the heavy plaque load makes it difficult to determine the amount of iAβ, but the levels appear to remain stable even with increasing extracellular Aβ. There is no staining in negative littermates or wild-type animals with this antibody, which confirms that it only labels human Aβ (Figure 3.1 F). Although the pattern of amyloid expression is similar between animals, there are huge individual differences both in plaque load (Heggland et al., 2015) and level of iAβ.

Figure 3.1. Expression of intracellular amyloid β (iAβ) at different ages in the McGill-R-Thy1-APP rat model. Coronal sections at approximately the same rostro-caudal level are labelled with the mouse anti-human Aβ antibody McSA1. iAβ is present in homozygous rats already at P15 (A), and the levels appear to increase up to one month (B), after which it remains stable to three months (C) and six months (D). At 18 months, there is heavy plaque pathology in several areas (E). There is no staining in negative animals with this antibody, as shown for a six month wild-type (WT) control (F). Scale bar: 1000 µm.

3.2. Intracellular amyloid β in reelin-immunoreactive principal cells in layer II of entorhinal cortex

EC LII is one of the most strongly iAβ-labelled areas in the McGill-R-Thy1-APP rat model (Figure 3.1 A-D), and the pattern of iAβ in this layer is remarkably similar to the distribution of cells positive for reelin in both lateral (LEC) and medial entorhinal cortex (MEC; Figure 3.2).

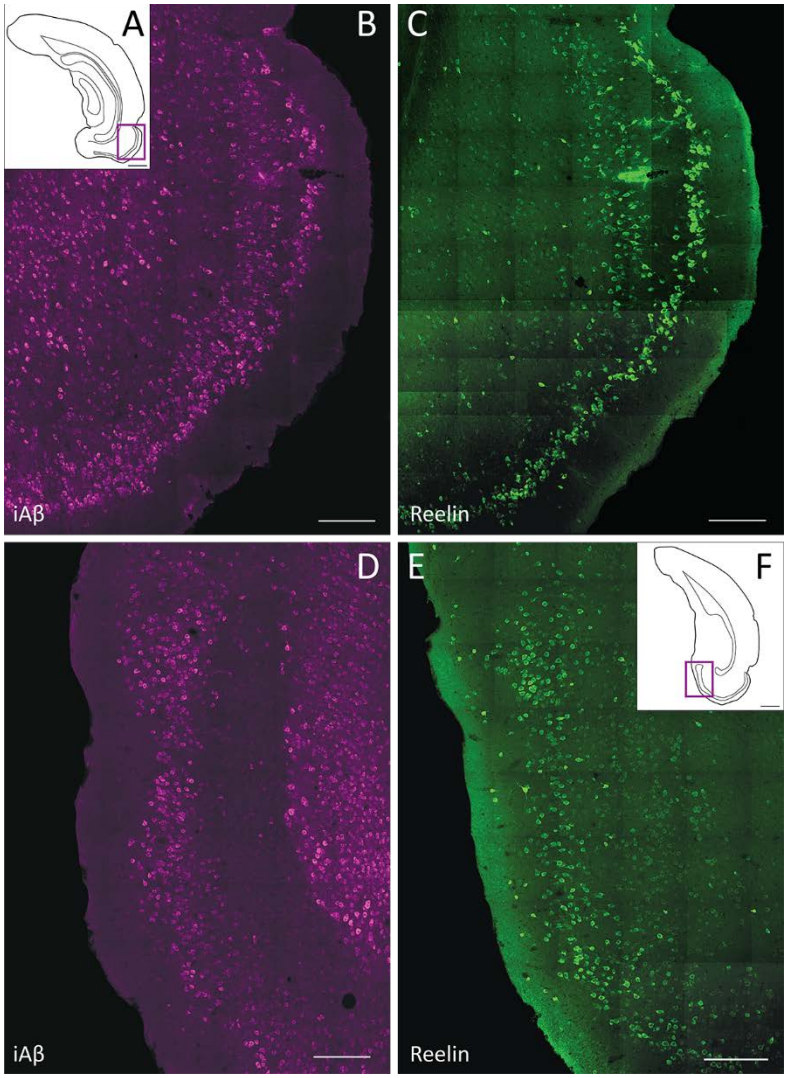

Figure 3.2. The expression of iAβ in layer II (LII) of both lateral and medial entorhinal cortex (LEC (A-C) and MEC (D-F), respectively), is similar to the pattern of reelin-immunoreactive principal cells, as show in single-stained adjacent sections from the same six months old homozygous McGill-R-Thy1-APP transgenic rat (ID: 19601). A, F: Schematic line drawings indicative of the rostro-caudal position of the selected coronal sections. Boxed areas indicate the extent and position of the high-power images shown in B, C, D, and E. B, D: iAβ labelled with McSA1 (mouse anti-human Aβ); C, E: reelin-positive cells labelled with mouse anti-reelin. Scale bars: 200 µm (B-E), 1000 µm (A, F).

3.2.1. Reelin and amyloid β antibody testing

The rabbit reelin antibody is relatively uncharacterised, and numerous variations were tested in order to optimise the immunohistochemistry protocol. Most of the tests were done prior to this master thesis project; thus, example images of these tests will not be shown here. A few additional variations

were tested after stereology, but none resulted in improved staining. Figures of these can be found in Appendix G along with descriptions.

Double-staining with rabbit anti-reelin and the G10 clone of mouse anti-reelin was done in order to further determine the specificity of the polyclonal rabbit antibody. The rabbit anti-reelin antibody strongly labelled LII of EC, and these cells had a particularly clear expression also with the mouse antibody (Figure 3.3 A-B). However, in other areas, more cells appeared positive with the rabbit antibody than with the mouse antibody, and it was often hard to distinguish labelled cells from what could be background or unspecific labelling (Figure 3.3 D-E).

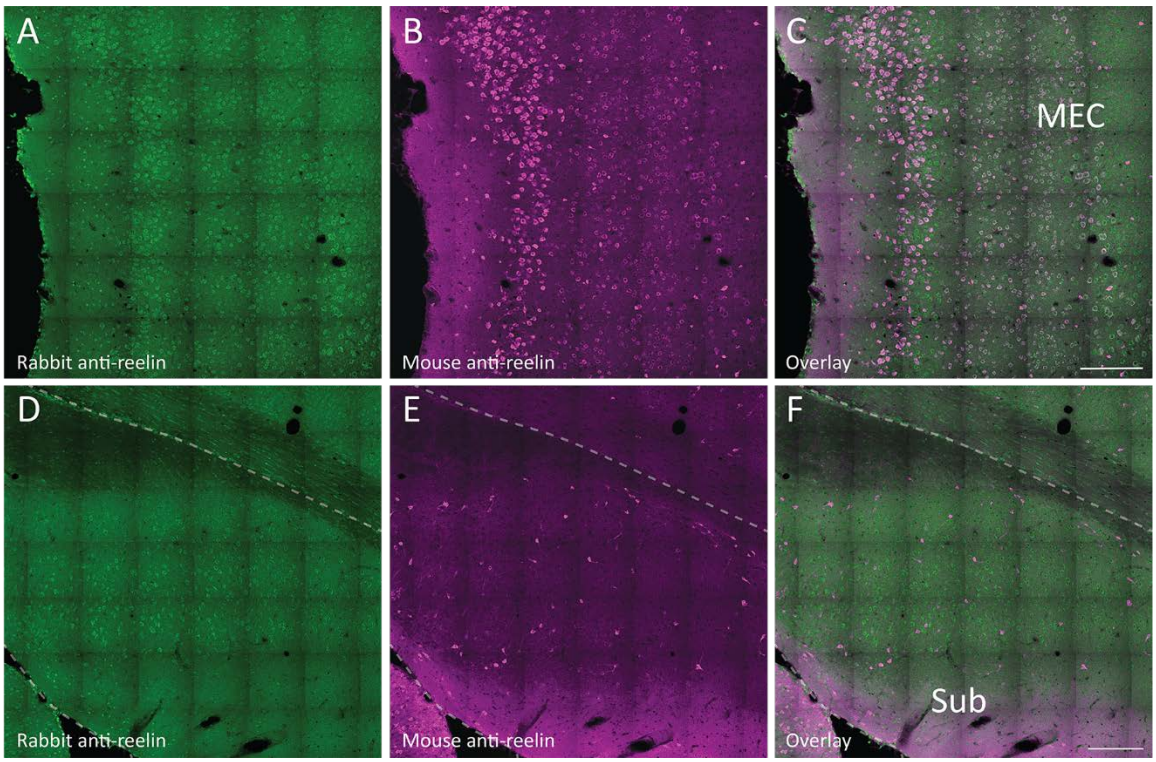

Figure 3.3. Difference in labelling of reelin-immunoreactive cells with two reelin-specific antibodies, shown for medial entorhinal cortex (MEC, A-C) and subiculum (Sub, D-F) of a one month old homozygous McGill-R-Thy1-APP transgenic rat (ID: 20061). A, D: rabbit anti-reelin; B, E: mouse anti-reelin; C, F: overlay. Scale bars: 200 µm.

Additional images from other areas and age groups can be found in Appendix H. Based on its variability and occasionally unspecific labelling, it was concluded that the rabbit antibody was not reliable enough to use for staining other areas than LII of EC. Thus, it was not used for further studies.

To ensure that the rabbit antibody did not influence the staining of the mouse antibody, single-stainings with mouse anti-reelin were also done on entire sections from one P15 and one six month old rat, as well as on tissue from age-matched negative controls. These tests confirmed that double-labelling did not influence the quality or staining pattern of the mouse reelin antibody. In addition, there was no apparent difference in reelin expression between P15 and six months old or between homozygous positive McGill-R-Thy1-APP rats and negative controls (Supplementary Figure H.2).

MOAB-2, a mouse monoclonal antibody to Aβ40/42, was tested as a potential alternative to McSA1. This antibody is of immunoglobulin subclass IgG2b, and can thus be used for double-labelling with mouse anti-reelin (IgG1). Furthermore, MOAB-2 is reported to be specific for Aβ40 and Aβ42 and not detect APP or APP-CTFs in 5XFAD mice (Youmans et al., 2012). Several protocol variations were tested; however, no satisfactory results were obtained. See Appendix G for descriptions of tested protocols and results.

3.2.2. Checks for spectral bleed-through

There were discrepancies in the quality of the rabbit anti-reelin staining between images taken using the fluorescent microscope and a 100x objective (Figure 3.6) and some of the subsequent images taken with the confocal microscope (Figures 3.8-3.15). The two filters used to visualise iAβ and reelin, respectively, showed remarkably similar labelling in the fluorescent microscope. To check whether the BP 450-490 filter used to visualise Alexa fluorophore 488 (reelin) caused spectral bleed-through from Alexa fluorophore 546 (iAβ), additional images of the reelin-labelling using a BP 470/40 and a BP 475/40 filter were taken. The intensity of labelling was reduced when visualised with the BP 470/40 and BP 475/40 filters, but most cells could still be separated from the background, indicating near complete co-localisation of reelin and iAβ or that the BP 470/40 and BP 475/40 filters also produced excitation of Alexa fluorophore 546 (Figure 3.4).

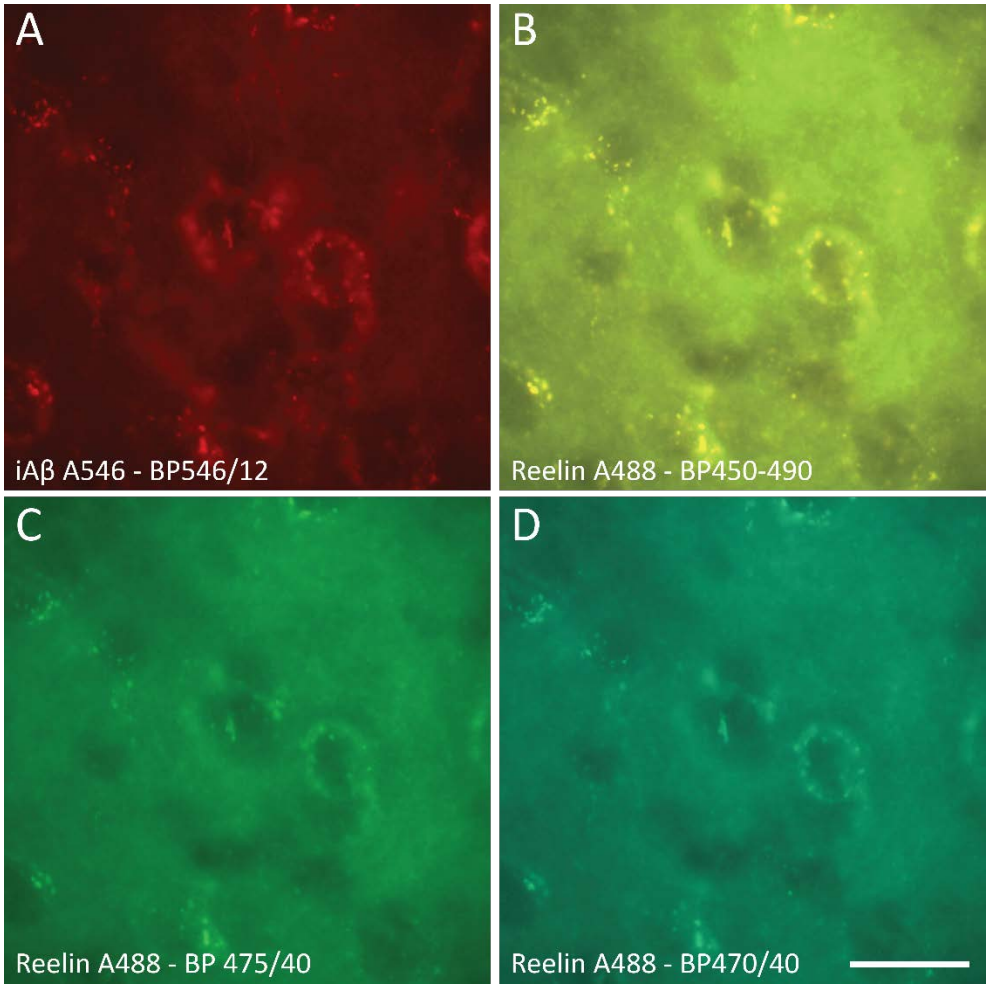

Figure 3.4. Representative images of cells labelled for iAβ and reelin visualised with different filter sets in subiculum in a one month old homozygous McGill-R-Thy1-APP transgenic rat (ID: 20061). A: iAβ-positive cells labelled with McSA1 (mouse anti-human Aβ) and Alexa fluorophore 546 visualised with a BP546/12 filter; B: reelin-positive cells labelled with rabbit anti-reelin and Alexa fluorophore 488 visualised with a BP450-490 filter; C: reelin-positive cells labelled with rabbit anti-reelin and Alexa fluorophore 488 visualised with a BP475/40 filter; D: reelin-positive cells labelled with rabbit anti-reelin and Alexa fluorophore 488 visualised with a BP470/40 filter. Scale bar: 20 µm.

Control images of section single-labelled with McSA1 and Alexa fluorophore 546 and excited using the BP 450-490 filter revealed faint contours of cells against the background, indicating background fluorescence or some spectral bleed-through of emitted fluorescence from the Alexa 546 dye (Figure 3.5).

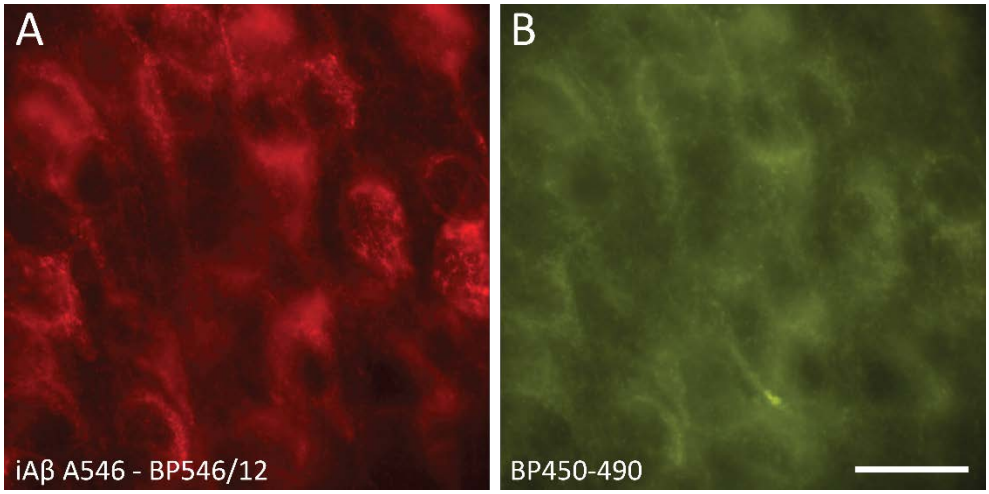

Figure 3.5. Control for spectral bleed-through by visualising cells labelled for iAβ with McSA1 and Alexa fluorophore 546. A: Visualisation with a BP546/12 filter showed clear labelling of cells; B: Visualisation with a BP450-490 filter, which should not show emission from Alexa fluorophore 546, showed faint contours of cells against the background. Scale bar: 20 µm.

3.2.3. Almost complete overlap between reelin- and amyloid ß-immunoreactive cells

20 rats divided into age groups P15, one month, three months, and six months (see Appendix D for details about rats) were used to investigate the potential co-localisation between iAβ and reelin in layer II (LII) of EC. For each age group, immunohistochemical double-labelling and unbiased stereology was used to estimate the total number of reelin-positive cells, iAβ-positive cells, and reelin and iAβ double-positive cells. After delineations, cells were counted throughout the entire rostro-caudal extent of LII of LEC and MEC in the right hemisphere. Our anatomical criteria yielded 10-19 sections of LEC and 6-12 sections of MEC per brain (Tables E.1 – E.4).

Fluorescent live images showed striking overlap between cells expressing of iAβ and reelin, as shown for two representative cases (Figure 3.6). Our counts confirmed a near complete overlap between reelin- and iAβ-immunoreactive cells in all age groups (Table 3.1). Out of a total number of 2124 cells in LEC and 3748 in MEC, we observed only 13 cells in LEC and 11 cells in MEC that were positive for reelin did not express iAβ, whereas we only observed four iAβ-expressing cells in LEC and four in MEC that were not reelin-positive. On average, 527 double-positive cells in LEC and 933 in MEC were counted for each age group.

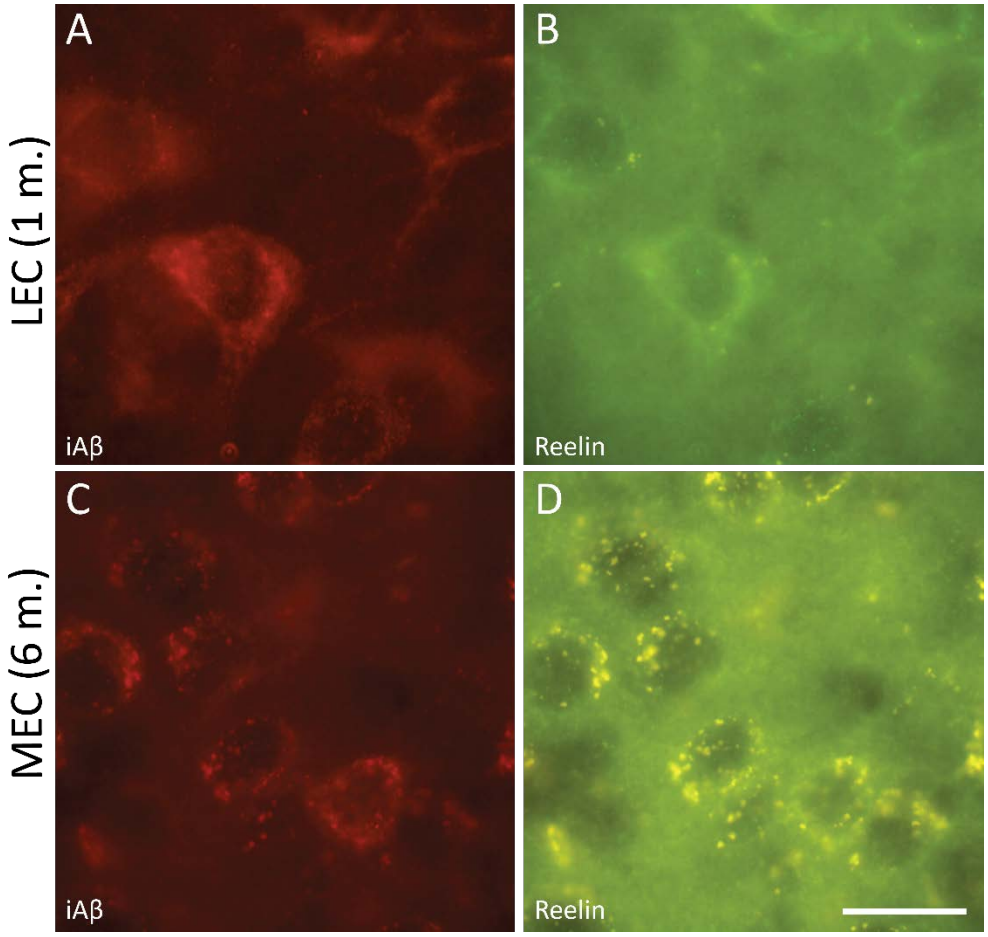

Figure 3.6. Cells labelled for iAβ and reelin in homozygous McGill-R-Thy1-APP transgenic rats visualised with the fluorescent microscope and a 100x objective. A, B: LII of LEC in a one month old rat (ID: 20061) from the area indicated in Figure 3.10. C, D: LII of MEC in a six months old rat (ID: 15234) from the area indicated in Figure 3.15. A, C: iAβ-positive cells labelled with McSA1 (mouse anti-human Aβ); B, D: reelin-positive cells labelled with rabbit anti-reelin. Scale bar: 20 µm.

Table 3.1. Total number of counted cells positive for reelin and intracellular amyloid β (iAβ; reelin+/iAβ+), positive for reelin and negative for iAβ (reelin+/iAβ-), and negative for reelin and positive for iAβ (reelin-/iAβ+) in LII of lateral and medial entorhinal cortex (LEC and MEC, respectively). Numbers are totalled over the five animals in each group.

	P15		1 month		3 months		6 months	
	LEC	MEC	LEC	MEC	LEC	MEC	LEC	MEC
Reelin+/iAβ+	443	622	587	1023	590	996	487	1092
Reelin+/iAβ-	9	7	0	0	0	0	4	4
Reelin-/iAβ+	0	1	0	0	1	2	3	1

Details from the Optical Fractionator used to estimate the total number of reelin and iAβ double-positive cells are shown in Table 3.2. The average CE was equal to or below the recommended value of 0.1 in all but two cases (MEC of the P15 group: 0.11; LEC of the six month group: 0.11). The CV was also relatively low in most cases, as was the calculated CE^2/CV^2 ratio, indicating that the biological variance between animals contributed more than the methodological variance to the total variance. A full table of number of counted cells, estimated cells, and CE values for each animal can be found in Appendix E.

Table 3.2. Details from the estimation of the total number of cells double-positive for iAβ and reelin in LII of lateral and medial entorhinal cortex (LEC and MEC, respectively) of age groups P15, one month, three months, and six months. Mean numbers are averaged over five animals.

	P15		1 month		3 months		6 months	
	LEC	MEC	LEC	MEC	LEC	MEC	LEC	MEC
Mean number of sections	11.6	7.0	11.4	10.2	14.0	9.0	14.2	8.6
Mean number of probes	149.4	158.0	117.8	269.2	168.2	231.6	175.4	297.8
Mean $\sum Q^-$	88.6	124.4	117.4	204.6	118.0	199.2	97.4	218.4
Mean CE	0.11	0.09	0.09	0.07	0.10	0.08	0.11	0.07
CV	0.22	0.29	0.16	0.11	0.33	0.17	0.18	0.11
CE^2/CV^2	0.24	0.10	0.33	0.42	0.09	0.19	0.35	0.43

Mean $\sum Q^-$: mean sum of cells counted per animal; mean CE: mean of the estimated coefficient of error for each animal, calculated as $\sqrt{\text{mean } CE^2}$; CV: observed coefficient of variance in each group, calculated as CV = SD/mean. CE^2/CV^2 estimates the contribution of the methodological variance to the total variance.

Estimated number of cells positive for both reelin and iAβ averaged were averaged for the five animals in each age group (Figure 3.7). The cell estimates increased with increasing age in MEC, whereas in LEC, the three month group had a slightly higher cell estimate than the six month group. The estimates ranged from 34,772 (P15 group) to 51,441 (three month group) for LEC, and from 78,834 (P15 group) to 130,122 (six month group) for MEC. The total numbers of cells single-positive for either reelin or iAβ were not estimated, as the cell counts were low (Table 3.1).

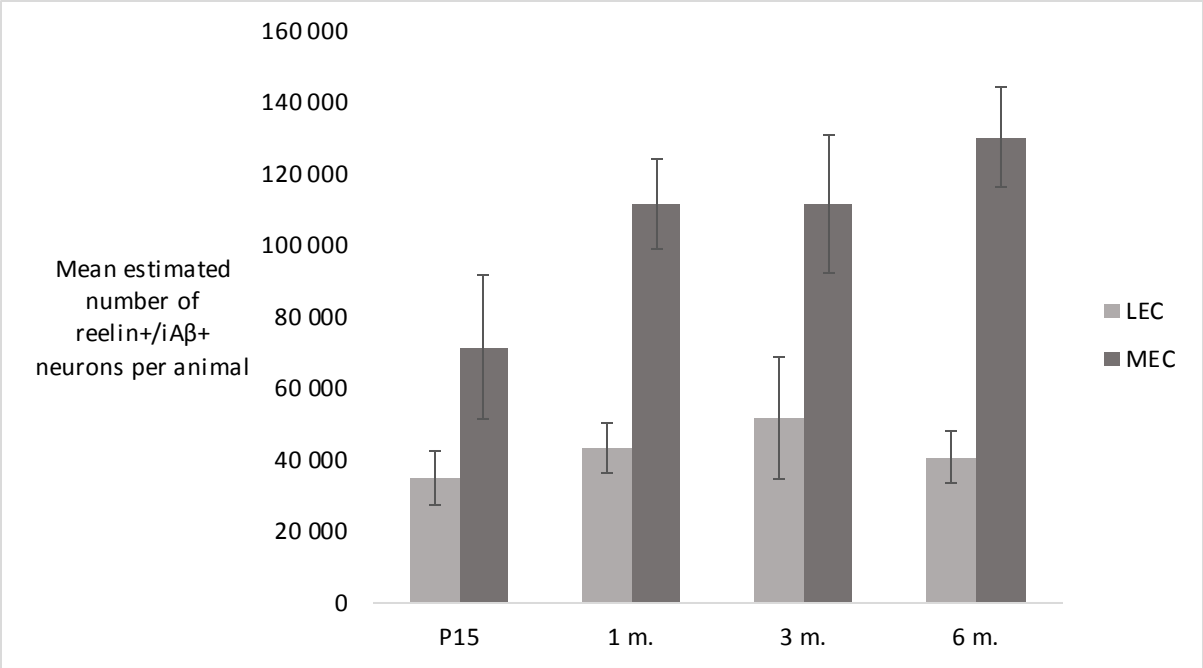

Figure 3.7. Estimates of the total number of neurons double-positive for reelin and iAβ in LII of lateral and medial entorhinal cortex (LEC and MEC, respectively) in age groups P15, one month (1 m.), three months (3 m.), and six months (6 m.) old. Numbers are averages of estimates for five animals in each group. Bars represent standard deviations.

Example images of immunohistochemical staining taken with the confocal microscope are shown for LEC and MEC of each age group in the sections below. Overall, the quality of the reelin-labelling when visualised with the confocal microscope was highly variable across animals, and the variability did not seem to correlate with differences between batches of antibody or rounds of immunolabelling (see Appendix G). However, there were some noticeable differences between the age groups, particularly the P15 and the six month group, with noticeably less labelling in the latter (Figures 3.8-9 and 3.14-15).

3.2.4. P15 group

In the P15 group, we counted 452 reelin-positive cells in total in LEC, nine of which were negative for iAβ. 443 cells were double-positive for reelin and iAβ. In MEC, we counted 630 cells in total, seven of which were reelin-positive/iAβ-negative, one of which was reelin-negative/iAβ-positive, and 622 of which were reelin- and iAβ-positive (Table 3.1). The average number of estimated reelin-/iAβ-positive neurons per animal was 34,771.6 ± 7,570.9 and 71,239.8 ± 20,188.8 for LEC and MEC, respectively (Figure 3.7). The mean CE was 0.11 for LEC and 0.09 for MEC.

Confocal images taken after stereology confirmed co-localisation of reelin and iAβ in LII of LEC (Figure 3.8 E) and MEC (Figure 3.9 E). Notably strong labelling of cells with the reelin antibody in deeper layers of both LEC (Figure 3.8) and MEC (Figure 3.9) was characteristic for the P15 group, as shown for a representative case.

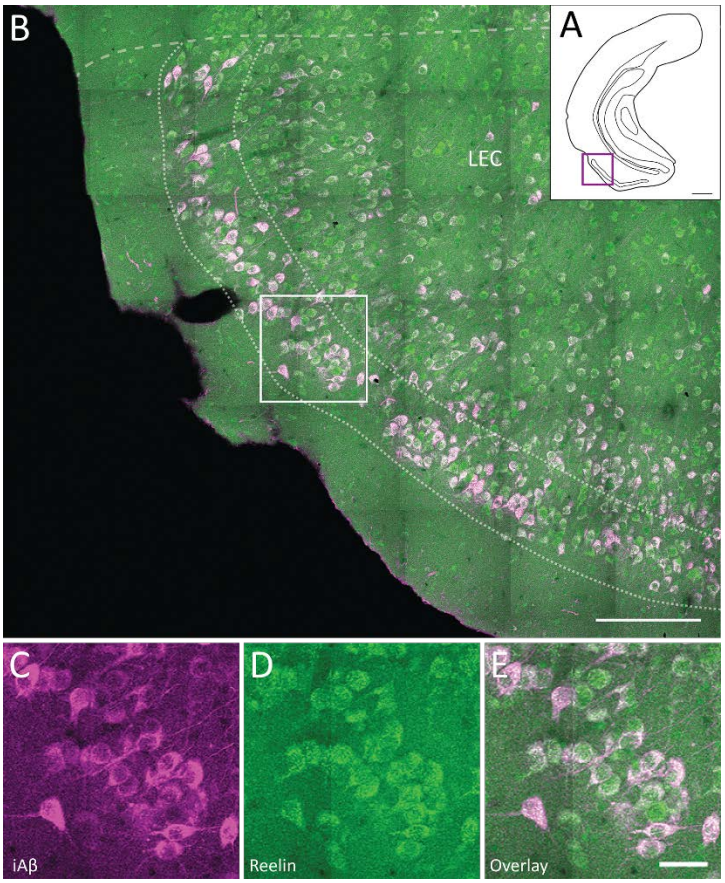

Figure 3.8. Cells expressing iAβ and reelin and cells double positive for reelin and iAβ in LII of lateral entorhinal cortex (LEC) in a P15 homozygous McGill-R-Thy1-APP transgenic rat (ID: 19872). A: Schematic line drawing illustrating the rostro-caudal position of the selected coronal section. The boxed area indicates the extent and position of the high-power image shown in B. B: Co-localisation of reelin and iAβ in LII of LEC. C: iAβ-positive cells labelled with McSA1 (mouse anti-human Aβ); D: reelin-positive cells labelled with rabbit anti-reelin; E: overlay. Scale bars: 1000 µm (A), 200 µm (B), 40 µm (C-E).

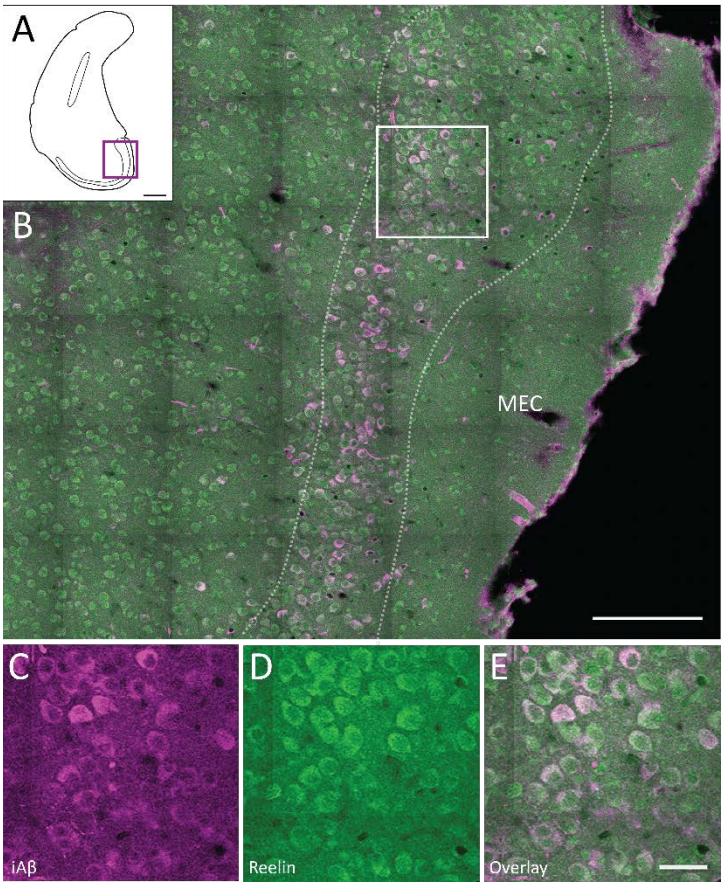

Figure 3.9. Cells expressing iAβ and reelin and cells double positive for reelin and iAβ in LII of medial entorhinal cortex (MEC) in a P15 homozygous McGill-R-Thy1-APP transgenic rat (ID: 19872). A: Schematic line drawing illustrating the rostro-caudal position of the selected coronal section. The boxed area indicates the extent and position of the high-power image shown in B. B: Co-localisation of reelin and iAβ in LII of MEC. C: iAβ-positive cells labelled with McSA1 (mouse anti-human Aβ); D: reelin-positive cells labelled with rabbit anti-reelin; E: overlay. Scale bars: 1000 µm (A), 200 µm (B), 40 µm (C-E).

3.2.5. One month group

In the one month old group, we counted in total 587 and 1023 cells in LEC and MEC, respectively, all of which were positive for both reelin and iAβ (Table 3.1). No cells were found to be single-labelled for either reelin or iAβ.The average number of estimated reelin-/iAβ-positive neurons per animal was 46,814.4 ± 15,251.8 and 111,482.2 ± 12,394.1 for LEC and MEC, respectively (Figure 3.7). The mean CE was 0.09 for LEC and 0.07 for MEC.

Overall, the quality of reelin- and iAβ-staining in LII of LEC and MEC was variable in the one month old group. The labelling of reelin-positive cells in LII of LEC was particularly clear in the shown case (Figure 3.10 B, D). However, the confocal images do not indicate a complete overlap of reelin- and iAβ (Figure 3.10 E), which contradicts the cell counts (Table 3.1). The labelling in MEC in this representative case was weaker and seemed to be less specifically restricted to LII (Figure 3.11 B, D).

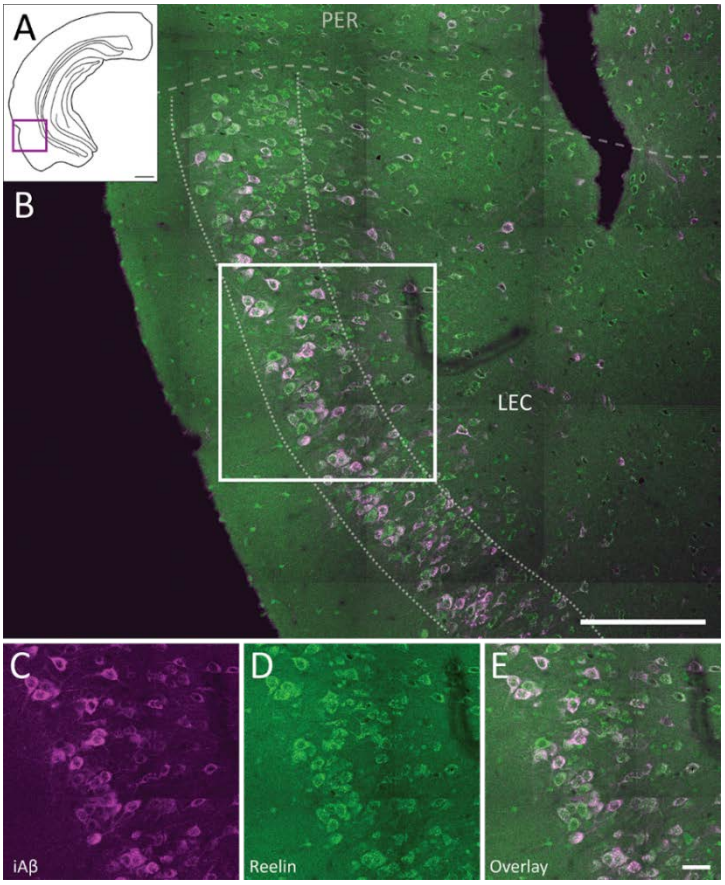

Figure 3.10. Cells expressing iAβ and reelin and cells double positive for reelin and iAβ in LII of lateral entorhinal cortex (LEC) in a one month old homozygous McGill-R-Thy1-APP transgenic rat (ID: 20061). A: Schematic line drawing illustrating the rostro-caudal position of the selected coronal section. The boxed area indicates the extent and position of the high-power image shown in B. B: Co-localisation of reelin and iAβ in LII of LEC close to the border of perirhinal cortex (PER). C: iAβ-positive cells labelled with McSA1 (mouse anti-human Aβ); D: reelin-positive cells labelled with rabbit anti-reelin; E: overlay. Scale bars: 1000 µm (A), 200 µm (B), 40 µm (C-E).

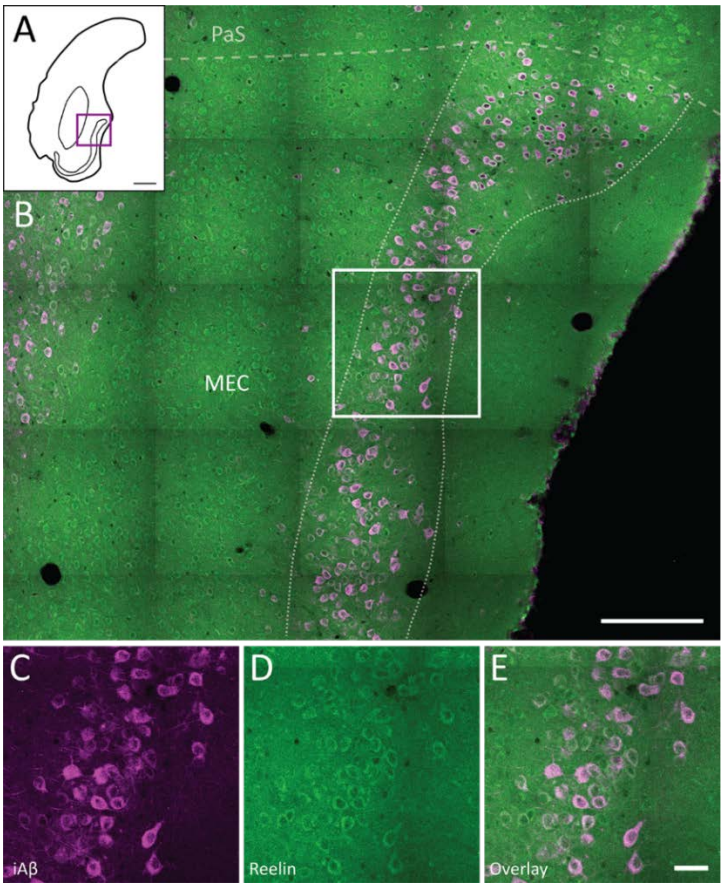

Figure 3.11. Cells expressing iAβ and reelin and cells double positive for reelin and iAβ in LII of medial entorhinal cortex (MEC) in a one month old homozygous McGill-R-Thy1-APP transgenic rat (ID: 20061). A: Schematic line drawing illustrating the rostro-caudal position of the selected coronal section. The boxed area indicates the extent and position of the high-power image shown in B. B: co-localisation of reelin and iAβ in LII of the most medial part of MEC, bordering parasubiculum (PaS). C: iAβ-positive cells labelled with McSA1 (mouse anti-human Aβ); D: reelin-positive cells labelled with rabbit anti-reelin; E: overlay. Scale bars: 1000 µm (A), 200 µm (B), 40 µm (C-E).

3.2.6. Three months group

In the three month old group, we counted 591 cells in total in LEC, of which one cell was negative for reelin and positive for iAβ. 590 cells were double-positive for reelin and iAβ. 998 cells were counted in total in MEC, two of which were reelin-negative and iAβ-positive, and 996 of which were double reelin- and iAβ-positive. No cells were positive for reelin and negative for iAβ in either area (Table 3.1). The average number of estimated reelin-/iAβ-positive neurons per animal was 51,440.4 ± 17,177.8 and 111,393.6 ± 19,226.7 for LEC and MEC, respectively (Figure 3.7). The mean CE was 0.10 for LEC and 0.08 for MEC.

Like the one month old group, the staining pattern in the three month group varied between animals when visualised with the confocal microscope. There was clear reelin-immunoreactivity in LII of LEC in the shown example case, but also more than expected in deeper layers (Figure 3.12). In MEC, the reelin labelling was more restricted to LII (Figure 3.13).

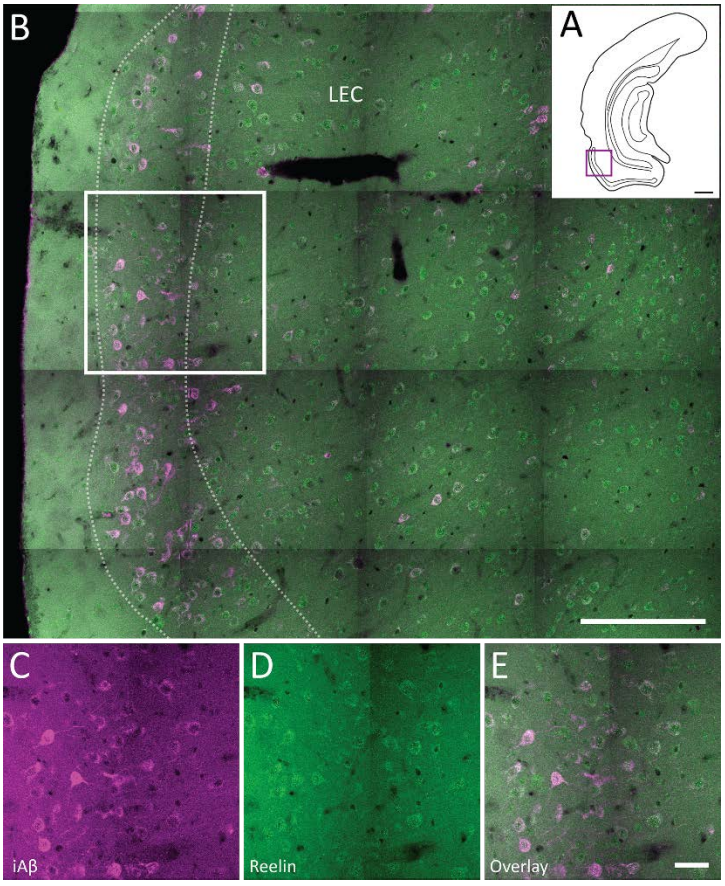

Figure 3.12. Cells expressing intracellular amyloid β (iAβ) and reelin and cells double positive for reelin and iAβ in LII of lateral entorhinal cortex (LEC) in a three months old homozygous McGill-R-Thy1-APP transgenic rat (ID: 17017). A: Schematic line drawing illustrating the rostro-caudal position of the selected coronal section. The boxed area indicates the extent and position of the high-power image shown in B. B: Co-localisation of reelin and iAβ in LII of LEC. C: iAβ-positive cells labelled with McSA1 (mouse anti-human Aβ); D: reelin-positive cells labelled with rabbit anti-reelin; E: overlay. Scale bars: 1000 µm (A), 200 µm (B), 40 µm (C-E).

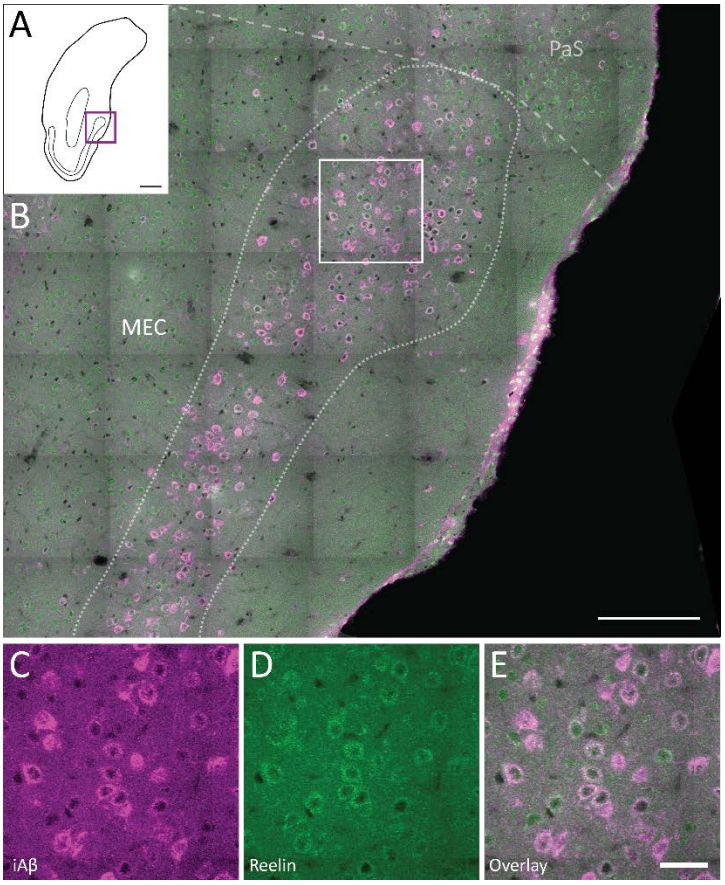

Figure 3.13. Cells expressing iAβ and reelin and cells double positive for reelin and iAβ in LII of medial entorhinal cortex (MEC) in a three months old homozygous McGill-R-Thy1-APP transgenic rat (ID: 17017). A: Schematic line drawing illustrating the rostro-caudal position of the selected coronal section. The boxed area indicates the extent and position of the high-power image shown in B. B: Co-localisation of reelin and iAβ in LII of the most medial part of MEC, bordering parasubiculum (PaS). C: iAβ-positive cells labelled with McSA1 (mouse anti-human Aβ); D: reelin-positive cells labelled with rabbit anti-reelin; E: overlay. Scale bars: 1000 µm (A), 200 µm (B), 40 µm (C-E).

3.2.7. Six months group

In the six month old group, we counted 494 cells in total in LEC, three of which were reelin-negative/iAβ-positive, four of which were reelin-positive/iAβ-negative, and 487 of which were reelin- and iAβ-positive. In MEC, 1097 cells were counted in total, four of which were reelin-positive/iAβ-negative, and one of which was reelin-negative/iAβ-positive (Table 3.1). 1092 cells were double-positive for reelin and iAβ. The average number of estimated reelin-/iAβ-positive neurons per animal was 40,524.6 ± 7,125.7 and 130,121.2 ± 13,969.0 for LEC and MEC, respectively (Figure 3.7). The mean CE was 0.1 for LEC and 0.07 for MEC.

In the six month group, the reelin-labelling was often weak in all layers, including LII, of both LEC (Figure 3.14 D) and MEC (Figure 3.15 D) when visualised with the confocal microscope, as shown for a representative case. However, clear co-localisation could be observed in the fluorescent microscope (Figure 3.6 C-D).

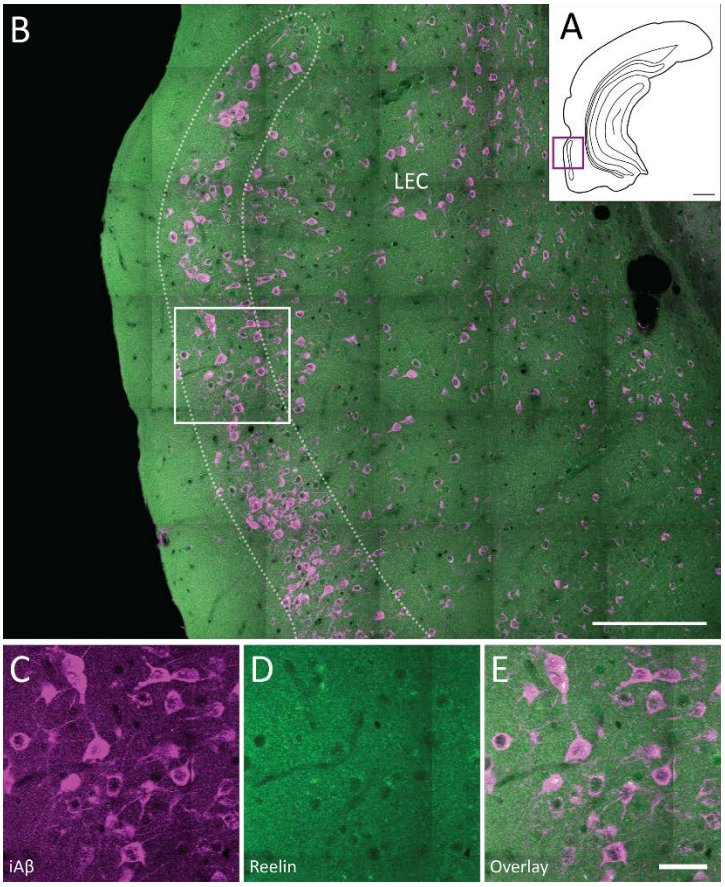

Figure 3.14. Cells expressing iAβ and reelin and cells double positive for reelin and iAβ in LII of lateral entorhinal cortex (LEC) in a six months old homozygous McGill-R-Thy1-APP transgenic rat (ID: 15234). A: Schematic line drawing illustrating the rostro-caudal position of the selected coronal section. The boxed area indicates the extent and position of the high-power image shown in B. B: Co-localisation of reelin and iAβ in LII of LEC. C: iAβ-positive cells labelled with McSA1 (mouse anti-human Aβ); D: reelin-positive cells labelled with rabbit anti-reelin; E: overlay. Scale bars: 1000 µm (A), 200 µm (B), 40 µm (C-E).

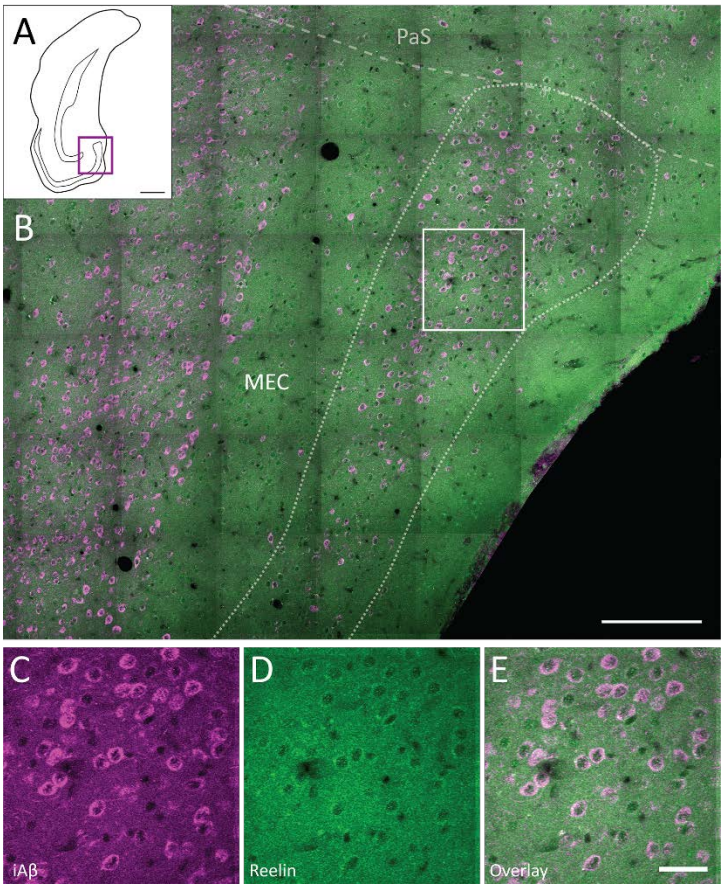

Figure 3.15. Cells expressing iAβ and reelin and cells double positive for reelin and iAβ in LII of medial entorhinal cortex (MEC) in a six months old homozygous McGill-R-Thy1-APP transgenic rat (ID: 15234). A: Schematic line drawing illustrating the rostro-caudal position of the selected coronal section. The boxed area indicates the extent and position of the high-power image shown in B. B: Co-localisation of reelin and iAβ in LII of the most medial part of MEC, bordering parasubiculum (PaS). C: iAβ-positive cells labelled with McSA1 (mouse anti-human Aβ); D: reelin-positive cells labelled with rabbit anti-reelin; E: overlay. Scale bars: 1000 µm (A), 200 µm (B), 40 µm (C-E)

3.3. Intracellular amyloid β in calbindin-immunoreactive cells in layer II of entorhinal cortex

To further investigate the specificity of the rabbit reelin antibody and to test whether calbindin-positive cells in EC LII express iAβ, double-immunohistochemical labelling with McSA1 and a rabbit anti-calbindin antibody was done on tissue from one, three, and six month old rats. The quality of the calbindin stains in the one month old rat was not as good as the others, and images of this will not be shown. To investigate potential co-localisation between reelin and calbindin in LII of EC, cells were double-labelled for calbindin and reelin using tissue from a six month old rat.

There was little to no expression of iAβ in calbindin-positive principal cells in LEC at three or six months. Calbindin-immunoreactive cells were generally located deeper in LII than iAβ-immunoreactive cells (Figure 3.16). Double-labelling for reelin and calbindin confirmed that reelin-positive cells were indeed located more superficially and did not co-localise with the calbindin-positive cells (Figure 3.17) in LEC, further indicating that the reelin-positive principal cells of LEC LII selectively express iAβ.

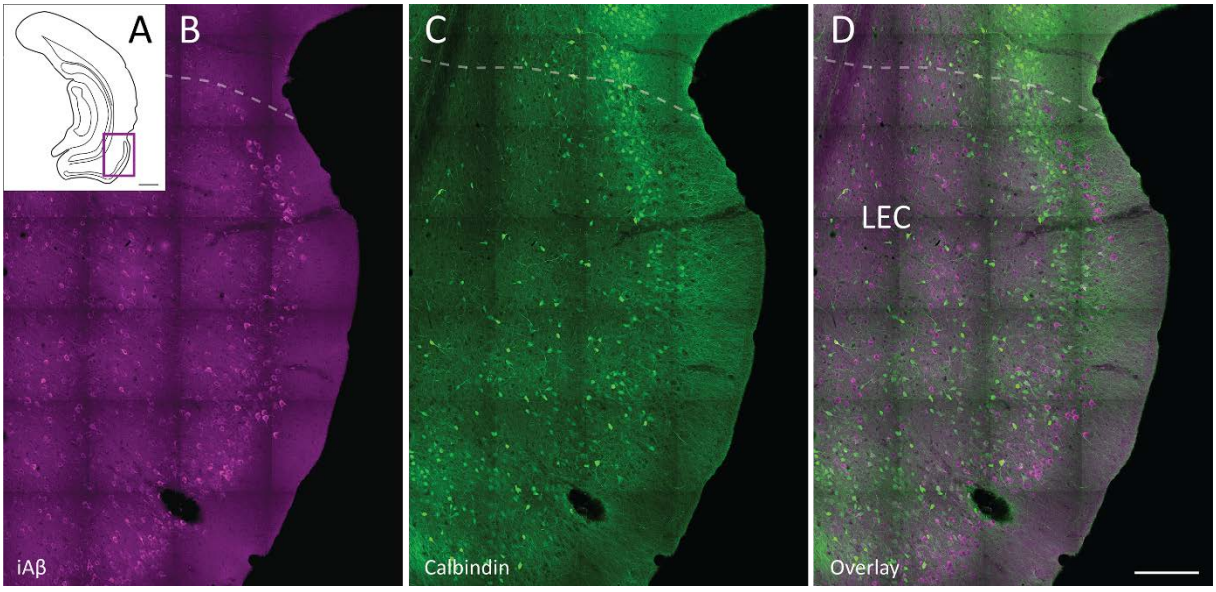

Figure 3.16. Calbindin-positive cells did not co-localise with cells positive for iAβ in LII of lateral entorhinal cortex (LEC, A) in homozygous McGill-R-Thy1-APP transgenic rats, as shown for a six months old animal (ID: 16804). A: Schematic line drawing illustrating the rostro-caudal position of the selected coronal section. The boxed area indicates the extent and position of the high-power images shown in B-D. B: iAβ-positive cells labelled with McSA1 (mouse anti-human Aβ); C: calbindin-positive cells labelled with rabbit anti-calbindin; D: overlay. Scale bars: 1000 µm (A), 200 µm (B-D).

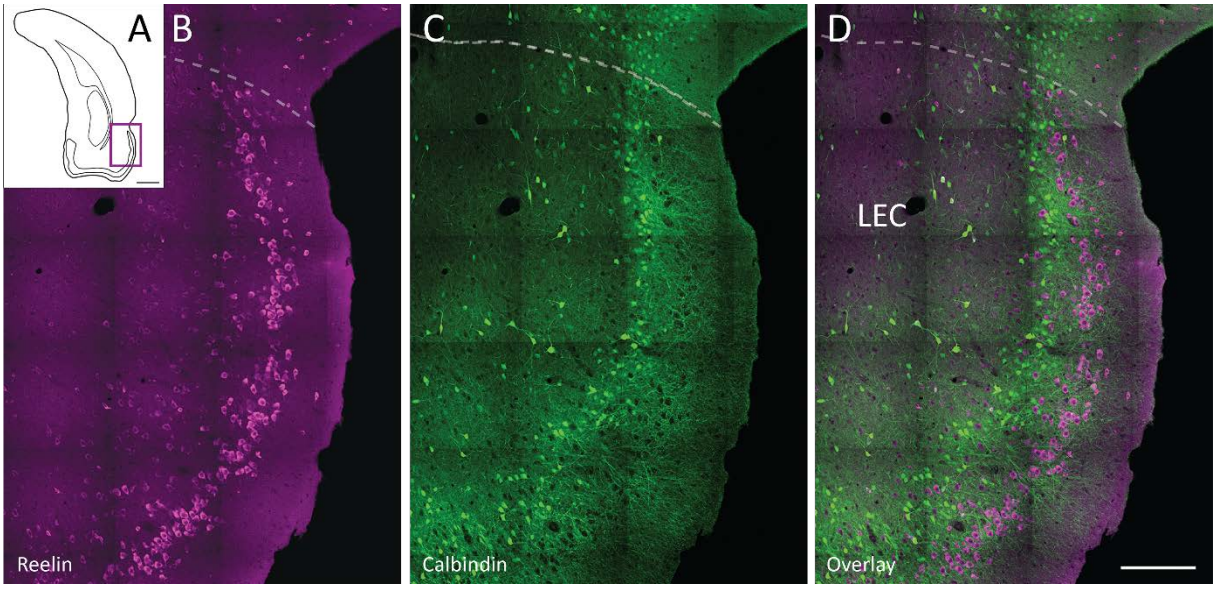

Figure 3.17. Reelin-positive cells were generally located more superficially and did not co-localise with calbindin-positive cells in LII of lateral entorhinal cortex (LEC, A) in homozygous McGill-R-Thy1-APP transgenic rats, as shown for a six months old animal (ID: 16804). A: Schematic line drawing illustrating the rostro-caudal position of the selected coronal section. The boxed area indicates the extent and position of the high-power images shown in B-D. B: reelin-positive cells labelled with mouse anti-reelin; C: calbindin-positive cells labelled with rabbit anti-calbindin; D: overlay. Scale bars: 1000 µm (A), 200 µm (B-D).

A proportion of calbindin-expressing cells were found to be positive for both iAβ (Figure 3.18) and reelin (Figure 3.19) in parts of MEC at three and six months. In particular, there was quite a substantial overlap between iAβ-positive cells and calbindin-positive cells in the most dorsal parts of caudal MEC, where the calbindin-cells were located more superficially in LII (Figure 3.18). Co-localisation with reelin was also observed in more ventral portions of MEC (Figure 3.19).

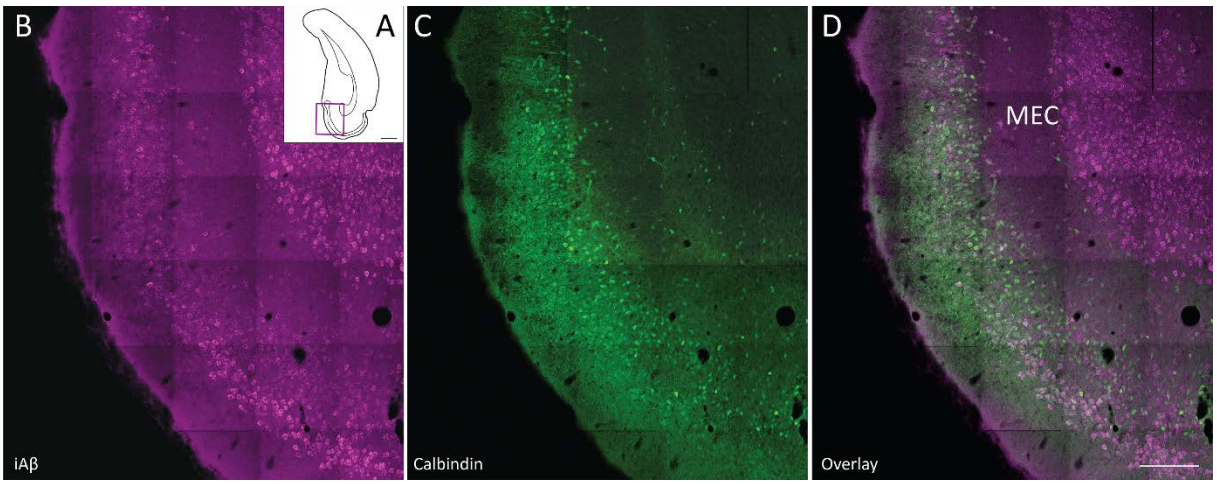

Figure 3.18 (previous). iAβ partially co-localised with calbindin in LII of dorsal and caudal parts of medial entorhinal cortex (MEC, A) in homozygous McGill-R-Thy1-APP transgenic rats, as shown for a six months old animal (ID: 19601). A: Schematic line drawing illustrating the rostro-caudal position of the selected coronal section. The boxed area indicates the extent and position of the high-power images shown in B-D. B: iAβ-positive cells labelled with McSA1 (mouse anti-human Aβ); C: calbindin-positive cells labelled with rabbit anti-calbindin; D: overlay. Scale bars: 1000 µm (A), 200 µm (B-D).

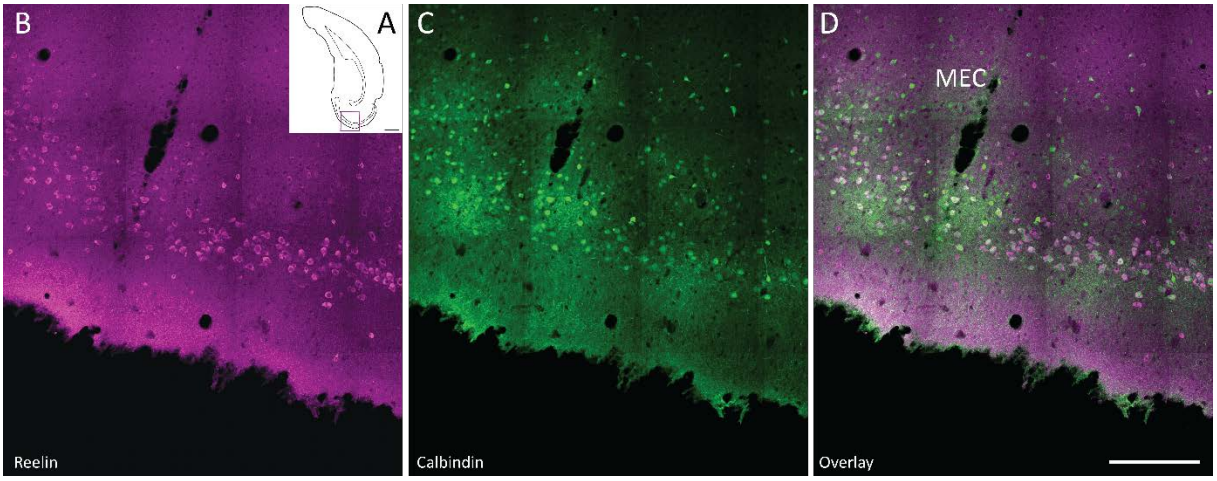

Figure 3.19. Cells double-positive for reelin and calbindin were found in in LII of caudal parts of medial entorhinal cortex (MEC, A) in homozygous McGill-R-Thy1-APP transgenic rats, as shown for a six months old animal (ID: 16804). A: Schematic line drawing illustrating the rostro-caudal position of the selected coronal section. The boxed area indicates the extent and position of the high-power images shown in B-D. B: reelin-positive cells labelled with mouse anti-reelin; C: calbindin-positive cells labelled with rabbit anti-calbindin; D: overlay. Scale bars: 1000 µm (A), 200 µm (B-D).

3.4. Intracellular amyloid β in interneurons in subiculum

10 homozygous McGill-R-Thy1-APP transgenic rats divided into age groups one month and six months old (see Appendix D for details on rats) were used to investigate expression of iAβ in interneurons in subiculum. The preliminary results indicated that a relatively large proportion of interneurons in dorsal subiculum express iAβ, whereas ventral subiculum appeared to have a smaller proportion of iAβ-positive interneurons. Based on this observation, topographic reciprocal connections with EC (Kloosterman et al., 2003), and a dorso-ventral segregation in function (O'Mara, 2005), the difference in the proportion of iAβ-expressing interneurons between dorsal, ventral, and intermediate subiculum, and between one month and six month old rats was investigated.

3.4.1. Control experiments

McSA1 and the GAD67 antibody are both made in mouse. However, as their heavy-chains are of different IgG classes (IgG1 and IgG2a, respectively), double-immunohistochemical labelling is possible with the use of immunoglobulin-specific secondary antibodies. To make sure that the immunoglobulin-specific secondary antibodies did not cross-react, controls with each of the primary antibodies and both secondary antibodies were performed. Neither of the antibodies showed any labelling when incubated with the secondary antibody specific for the other immunoglobulin sub-class, as shown for a representative example in a three month old homozygous rat (Supplementary Figures H.3 and H.4).

3.4.2. 20-40% of interneurons in subiculum express iAβ

The individual percentages of iAβ-immunoreactive interneurons were overall highest in dorsal subiculum and lowest in ventral subiculum, and ranged from 17.29% (ventral subiculum, six month old rat) to 51.33% (intermediate subiculum, one month old rat; Table 3.3). The counts were highly variable between animals, especially in intermediate subiculum of the one month group. However, the proportions were fairly constant within each animal, so that high counts in one area generally meant high counts in the other areas in that animal (Figure 3.20). There was a noticeable difference in mean proportion of iAβ-positive interneurons between dorsal and ventral subiculum, with intermediate subiculum being more similar to dorsal subiculum. In both dorsal and ventral subiculum, interneurons of the molecular layer rarely expressed iAβ (Figures 3.21, 3.23, 3.24, 3.26). More detailed tables with numbers for each individual animal can be found in Appendix F.

Table 3.3. Details from the counts of iAβ in interneurons in dorsal (DS), ventral (VS), and intermediate (IS) subiculum in five one month and five six month old homozygous McGill-R-Thy1-APP transgenic rats.

	1 month			6 months		
	DS	IS	VS	DS	IS	VS
Mean number of sections	11.6	2.0	6.8	12.6	2.4	7.2
Mean GAD67+/iAβ-	432.2	137.6	315.4	306.4	105.2	339.8
Mean GAD67+/iAβ+	237.6	67.0	88.6	201.4	54.8	103.6
Mean % iAβ+	**36.20**	**34.86**	**22.59**	**40.30**	**34.06**	**24.35**
SD	6.54	12.10	5.16	9.04	8.07	7.43

GAD67+/iAβ-: number of cells positive for GAD67 and negative for iAβ; GAD67+/iAβ+: cells positive for both GAD67 and iAβ; % iAβ: percentage of GAD67-postiive cells that also stain positive for iAβ; SD: standard deviation.

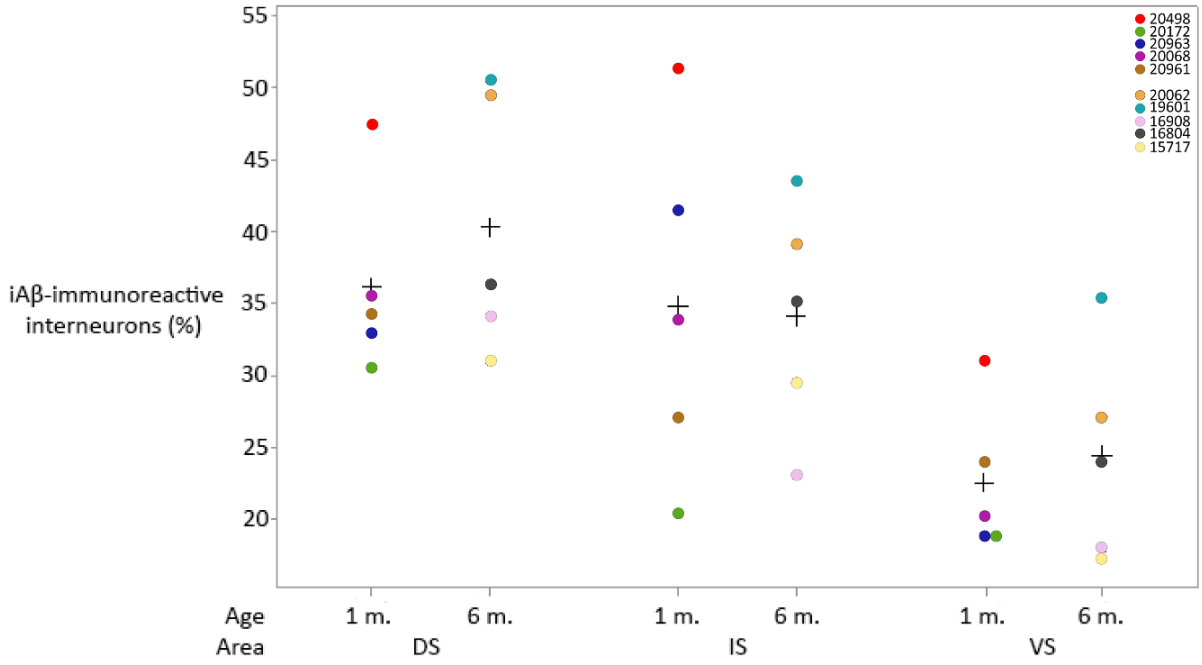

Figure 3.20. Percentages of GAD67-expressing cells that also express iAβ in dorsal (DS), intermediate (IS), and ventral (VS) subiculum in a total of ten homozygous McGill-R-Thy1-APP transgenic rats, separated into age groups one month (1 m.) and six months (6 m.) old. Coloured circles represent counts for individual animals and crosses represent mean values.

The differences in proportions were statistically tested using a multi-way analysis of variance (ANOVA) with the factors rat ID, area, and age by fitting a mixed linear model. The factors area and age were considered as fixed, whereas ID was considered a random factor and included to account for repeated

measures within the same animal. The ANOVA revealed a significant effect of area ($P < 0.000$) and rat ID ($P < 0.000$) on proportions of iAβ-positive GAD67 cells, whereas there was no significant effect of age ($P = 0.735$). There was no interaction between the factors area and age ($P = 0.436$). Post-hoc pairwise comparisons with Bonferroni corrections were performed to investigate specific differences between the three areas. There was a significant difference between dorsal and ventral subiculum ($P < 0.000$) and between ventral and intermediate subiculum ($P < 0.000$), but not between dorsal and intermediate subiculum ($P = 0.162$).

Specific area differences between the age groups were also tested with three separate Welch's t-tests. No significant differences were found (dorsal: $P = 0.437$; ventral: $P = 0.676$; intermediate: $P = 0.906$), indicating that the proportion of interneurons that express iAβ does not change from one to six months in either dorsal, ventral, or intermediate subiculum.

A multi-way ANOVA requires that the data has a normal distribution and that there is homogeneity of variances. Normality of the data was tested using a Shapiro-Wilk test, which revealed that the data set was indeed normally distributed ($P = 0.231$). The residuals were also normally distributed ($P = 0.111$). A Levene's test showed that the variances were equal ($P = 0.599$).

3.4.3. One month group

A total of 7025 GAD67-immunoreactive cells were counted in dorsal, ventral, and intermediate subiculum of five one month old rats. Of the counted GAD67-immunoreactive cells, 2231 (31.8%) were also immunoreactive for iAβ (Table 3.3).

In dorsal subiculum, the number of GAD67-positive cells not expressing iAβ averaged 432.2 per animal, whereas an average of 237.6 GAD67-positive cells also expressed iAβ, as illustrated for a representative case (Figure 3.21 and Supplementary Figures H.5 and H.6). Thus, 36.2% of interneurons was positive for iAβ.

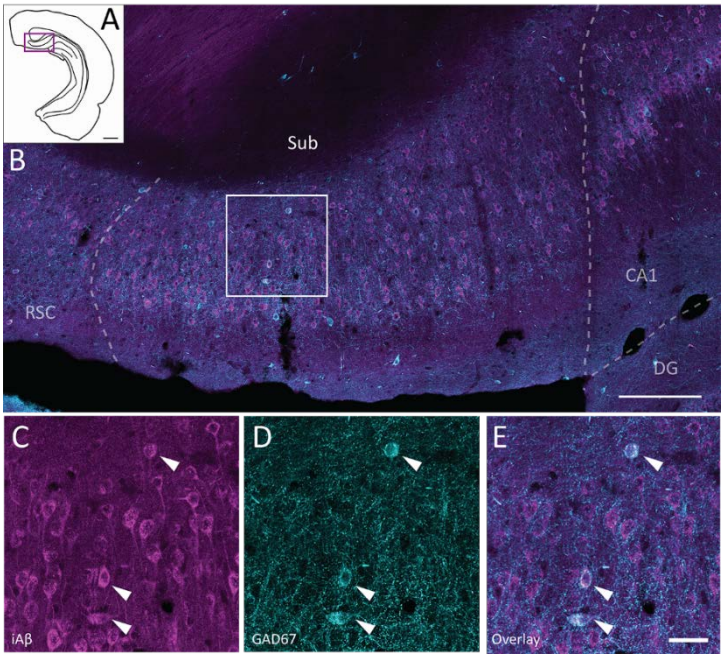

Figure 3.21. GAD67-positive cells expressing iAβ in dorsal subiculum of a one month old homozygous McGill-R-Thy1-APP transgenic rat (ID: 20498). A: Schematic line drawing illustrating the rostro-caudal position of the selected coronal section. The boxed area indicates the extent and position of the high-power image shown in B. B: Co-localisation of GAD67 and iAβ in dorsal subiculum. C: iAβ-positive cells stained with McSA1 (mouse anti-human Aβ); D: interneurons stained with mouse anti-GAD67; E: overlay. Scale bars: 1000 µm (A), 200 µm (B), 40 µm (C-E). CA1: Cornu Ammonis 1; DG: dentate gyrus; RSC: retrosplenial cortex; Sub: subiculum.

In intermediate subiculum, the number of GAD67-positive cells not expressing iAβ averaged 137.6 per animal, whereas an average of 67.0 GAD67-positive cells also expressed iAβ, as illustrated for a representative case (Figure 3.22). Thus, 34.9% of interneurons was positive for iAβ.

In ventral subiculum, the number of GAD67-positive cells not expressing iAβ averaged 315.4 per animal, whereas an average of 88.6 GAD67-positive cells also expressed iAβ, as illustrated for a representative case (Figure 3.23 and Supplementary Figure H.7). Thus, 22.6% of counted interneurons was positive for iAβ.

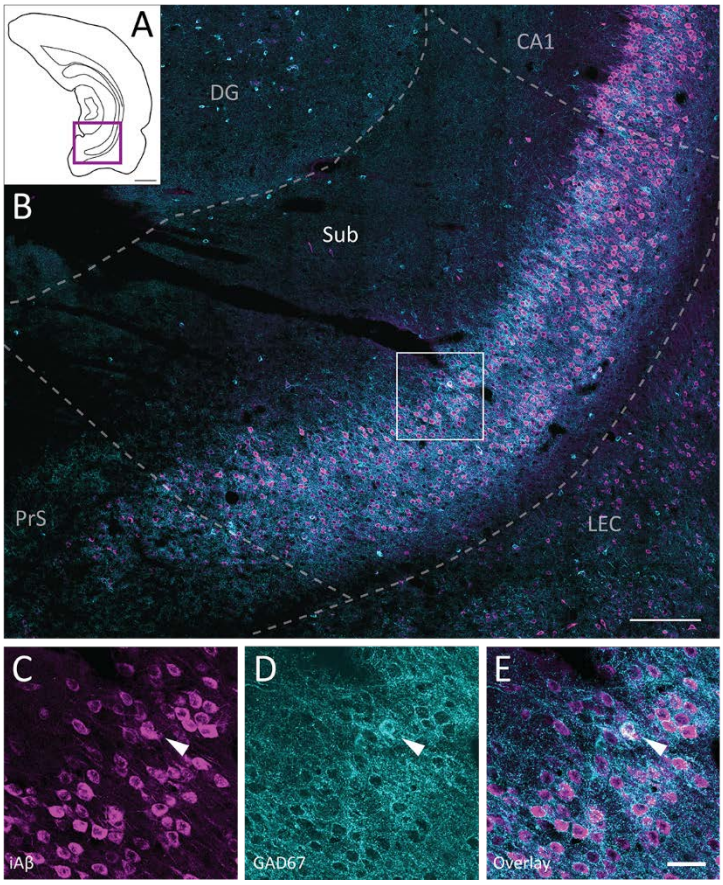

Figure 3.22. GAD67-positive cells expressing iAβ in intermediate subiculum of a one month old homozygous McGill-R-Thy1-APP transgenic rat (ID: 20498). A: Schematic line drawing illustrating the rostro-caudal position of the selected coronal section. The boxed area indicates the extent and position of the high-power image shown in B. B: Co-localisation of GAD67 and iAβ in intermediate subiculum. C: iAβ-positive cells stained with McSA1 (mouse anti-human Aβ); D: interneurons stained with mouse anti-GAD67; E: overlay. Scale bars: 1000 µm (A), 200 µm (B), 40 µm (C-E). PaS: parasubiculum; PrS: presubiculum; Sub: subiculum.

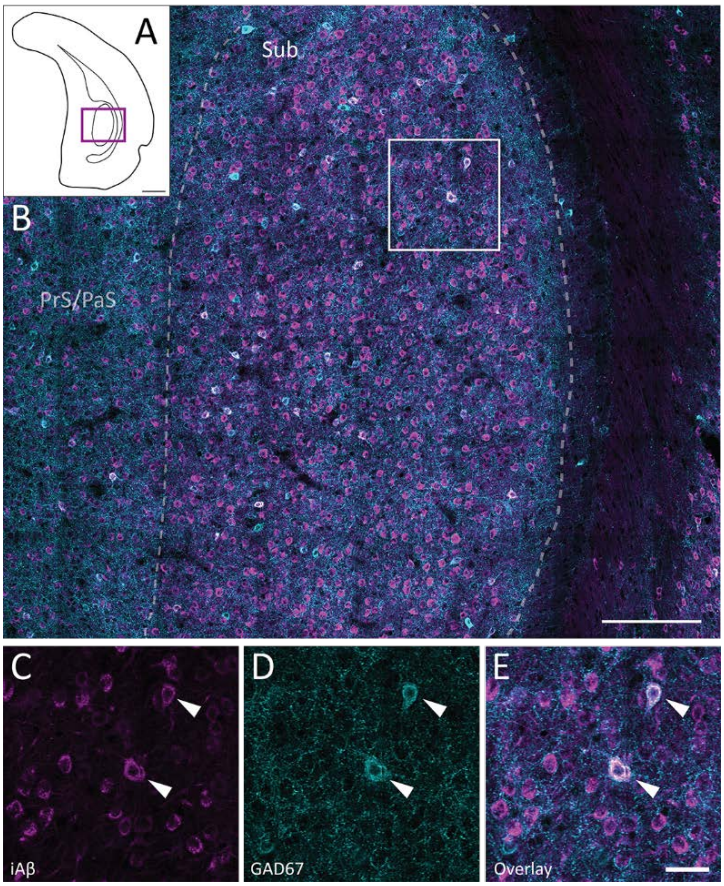

Figure 3.23. GAD67-positive cells expressing iAβ in ventral subiculum of a one month old homozygous McGill-R-Thy1-APP transgenic rat (ID: 20498). A: Schematic line drawing illustrating the rostro-caudal position of the selected coronal section. The boxed area indicates the extent and position of the high-power image shown in B. B: Co-localisation of GAD67 and iAβ in ventral subiculum. C: iAβ-positive cells stained with McSA1 (mouse anti-human Aβ); D: interneurons stained with mouse anti-GAD67; E: overlay. Scale bars: 1000 µm (A), 200 µm (B), 40 µm (C-E). CA1: Cornu Ammonis 1; DG: dentate gyrus; LEC: lateral entorhinal cortex; PrS: presubiculum; Sub: subiculum.

3.4.4. Six months group

A total of 5556 GAD67-immunoreactive cells were counted in dorsal, ventral, and intermediate subiculum of five six month old rats. Of the counted GAD67-immunoreactive cells, 1799 (32.4%) were also immunoreactive for iAβ (Table 3.3).

In dorsal subiculum, the number of GAD67-positive cells not expressing iAβ averaged 306.4 per animal, whereas an average of 201.4 GAD67-positive cells also expressed iAβ, as illustrated for a representative case (Figure 3.24 and Supplementary Figures H.8 and H.9). Thus, 40.3% of the total counted interneurons was positive for iAβ.

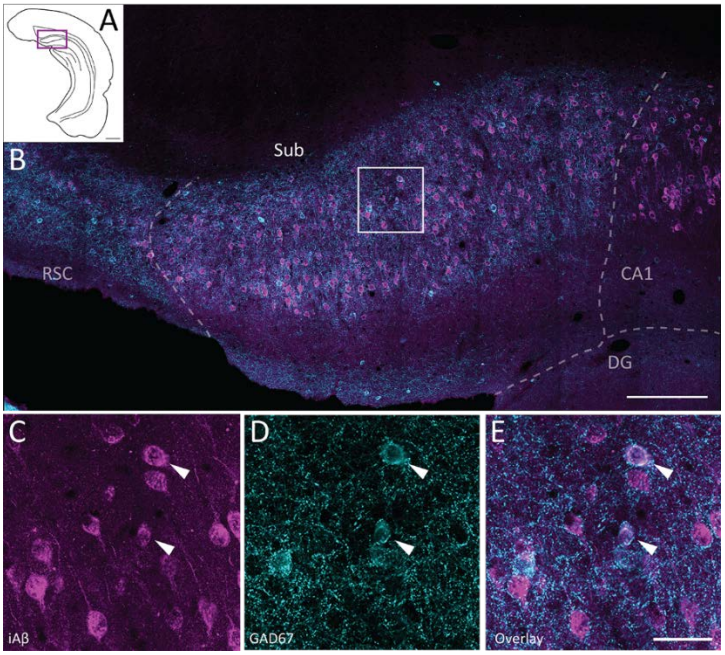

Figure 3.24. GAD67-positive cells expressing iAβ in dorsal subiculum of a six months old homozygous McGill-R-Thy1-APP transgenic rat (ID: 16908). A: Schematic line drawing illustrating the rostro-caudal position of the selected coronal section. The boxed area indicates the extent and position of the high-power image shown in B. B: Co-localisation of GAD67 and iAβ in dorsal subiculum. C: iAβ-positive cells stained with McSA1 (mouse anti-human Aβ); D: interneurons stained with mouse anti-GAD67; E: overlay. Scale bars: 1000 µm (A), 200 µm (B), 40 µm (C-E). CA1: Cornu Ammonis 1; DG: dentate gyrus; RSC: retrosplenial cortex; Sub: subiculum.

In intermediate subiculum, the number of GAD67-positive cells not expressing iAβ averaged 105.2 per animal, whereas an average of 54.8 GAD67-positive cells also expressed iAβ, as illustrated for a representative case (Figure 3.25). Thus, 34.1% of the total counted interneurons was positive for iAβ.

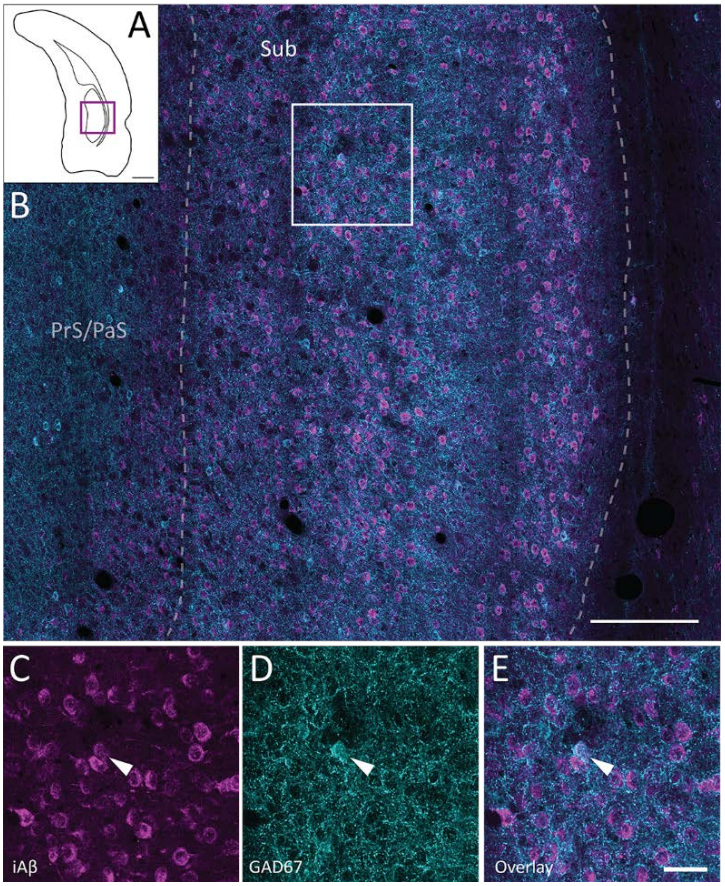

Figure 3.25. GAD67-positive cells expressing iAβ in intermediate subiculum of a six months old homozygous McGill-R-Thy1-APP transgenic rat (ID: 16908). A: Schematic line drawing illustrating the rostro-caudal position of the selected coronal section. The boxed area indicates the extent and position of the high-power image shown in B. B: Co-localisation of GAD67 and iAβ in intermediate subiculum. C: iAβ-positive cells stained with McSA1 (mouse anti-human Aβ); D: interneurons stained with mouse anti-GAD67; E: overlay. Scale bars: 1000 µm (A), 200 µm (B), 40 µm (C-E). PaS: parasubiculum; PrS: presubiculum; Sub: subiculum.

In ventral subiculum, the number of GAD67-positive cells not expressing iAβ averaged 339.8 per animal, whereas an average of 103.6 GAD67-positive cells also expressed iAβ, as illustrated for a representative case (Figure 3.26 and Supplementary Figure H.10). Thus, 24.4% of the total counted interneurons was positive for iAβ.

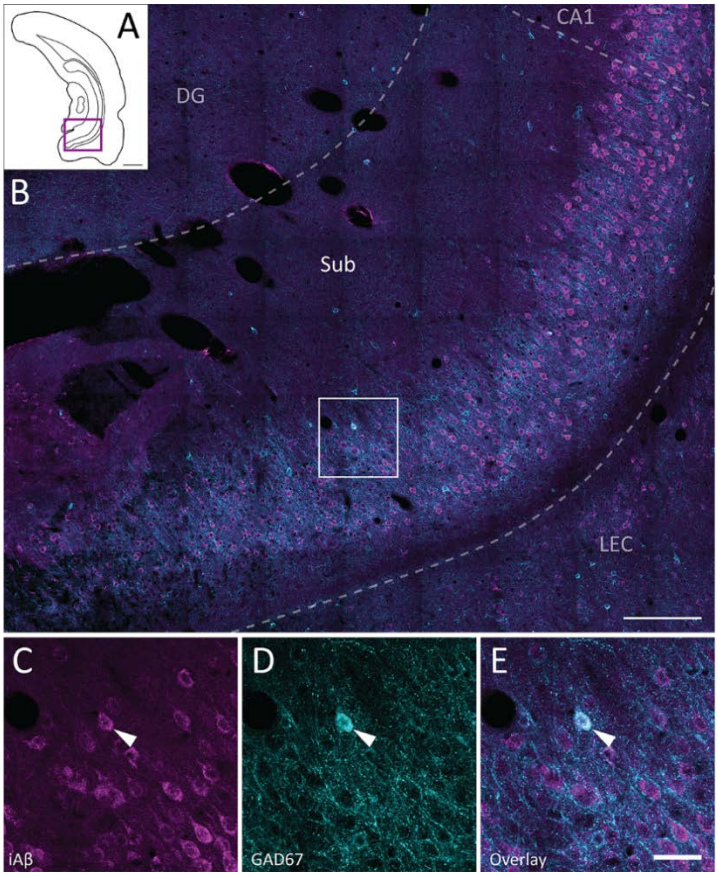

Figure 3.26. GAD67-positive cells expressing iAβ in ventral subiculum of a six months old homozygous McGill-R-Thy1-APP transgenic rat (ID: 16908). A: Schematic line drawing illustrating the rostro-caudal position of the selected coronal section. The boxed area indicates the extent and position of the high-power image shown in B. B: Co-localisation of GAD67 and iAβ in ventral subiculum. C: iAβ-positive cells stained with McSA1 (mouse anti-human Aβ); D: interneurons stained with mouse anti-GAD67; E: overlay. Scale bars: 1000 µm (A), 200 µm (B), 40 µm (C-E). CA1: Cornu Ammonis 1; DG: dentate gyrus; LEC: lateral entorhinal cortex; PrS: presubiculum; Sub: subiculum.

3.5. Intracellular amyloid β in interneurons in other areas of the hippocampal formation and parahippocampal region

The distribution of iAβ in interneurons in other areas of HF and PHR was also investigated in P15, one month, three month, and six month old homozygous McGill-R-Thy1-APP transgenic rats. iAβ-immunoreactive interneurons could be found in all areas and most layers of HF and PHR. Generally, iAβ-immunoreactive interneurons did not seem to be as frequent as iAβ-positive principal cells, and they were not as strongly stained for iAβ. There was no apparent difference between age groups one month, three months, and six months. In the P15 group, there was less overall iAβ-immunoreactivity (see Figure 3.1), which was also evident in the proportion of iAβ-positive interneurons (Supplementary Figure H.11).

3.5.1. Hippocampal formation

In the hippocampus, there was generally stronger iAβ-labelling in the pyramidal layer of CA1 and CA3 than of CA2 with the McSA1 antibody (Supplementary Figures H.12 and H.13). This was mirrored in the proportion of interneurons that were positive for iAβ, although iAβ-positive interneurons were observed in CA2 (Supplementary Figure H.14). Most iAβ-positive interneurons in CA1 and CA3 were found in strata oriens and radiatum. A slightly higher proportion of interneurons appeared to be positive for iAβ in the dorsal than in the ventral CA fields (Supplementary Figure H.15), similar to what was observed for subiculum. In dentate gyrus (DG), most interneurons were not iAβ-positive, although a few could be observed along the hilar border of the granule cell layer (data not shown).

3.5.2. Parahippocampal region

In general, there was less co-localisation in PHR than in HF. iAβ-immunoreactive interneurons seemed to be very sparse rostrally in LEC and perirhinal cortex. When present in rostral LEC, the positive interneurons were mostly located in layer V (Supplementary Figure H.16). In perirhinal cortex, they seemed to also be in superficial layers, although most were found in deep layers as well (Supplementary Figure H.17). The largest proportion of iAβ-positive interneurons was found in caudal EC, mostly close to the rhinal fissure, where co-localisation was frequent in superficial layers (Supplementary Figure H.18). At the caudalmost level, there was also notably more co-localisation in pre- and parasubiculum than seen at more rostral levels (Supplementary Figures H.19 and H.20). In postrhinal cortex, iAβ-positive interneurons were present both in superficial and deep layers (Supplementary Figure H.21).

3.6. Intracellular amyloid β in interneuron subsets

Several studies have identified other subsets of interneurons as selectively vulnerable to accumulation of Aβ and AD-related cell death, including somatostatin-expressing (Saiz-Sanchez et al., 2012) and parvalbumin-expressing interneurons (Takahashi et al., 2010). It was therefore checked whether iAβ was expressed in groups of interneurons identified by presence of parvalbumin in a three month old homozygous rat (ID: 17015) and somatostatin in a six month old homozygous rat (ID: 16908).

3.6.1. Parvalbumin

Parvalbumin-expressing cells make up a fairly large proportion of hippocampal interneurons (Freund and Buzsaki, 1996), and this was reflected in the proportion of cells triple-positive for GAD67, iAβ, and parvalbumin. Many iAβ-expressing interneurons in HF were parvalbumin-immunoreactive, as shown for subiculum (Supplementary Figure H.22), and triple-labelled cells were also found in PHR, as shown for LEC (Supplementary Figure H.23). However, most parvalbumin-positive interneurons were not iAβ-positive, in line with the general observation that the majority of interneurons, as visualised with GAD67-immunoreactivity, did not express iAβ.

3.6.2. Somatostatin

iAβ-expressing somatostatin cells were not abundant, although they could be found in various areas of HF and PHR. In particular, iAβ-expressing somatostatin cells were observed in CA1, CA3, and DG, as shown for CA3 (Supplementary Figure H.24). Few somatostatin-positive cells in subiculum expressed iAβ.

3.6.3. Reelin

Reelin is mostly found in interneurons in the adult rat bran (Pesold et al., 1998). Based on the expression of iAβ in reelin-immunoreactive principal cells of EC LII, it was of interest to investigate whether reelin-positive interneurons also express iAβ. However, as McSA1 and mouse anti-reelin have the same immunoglobulin heavy-chain (IgG1) and rabbit anti-reelin was considered too unreliable to label interneurons (see section 3.2.1), this could not be done without more complicated immunohistochemistry protocols, which for time reasons was not carried out. Double labelling for reelin and GAD67 was done on tissue from a six month old homozygous transgenic McGill-R-Thy1-APP rat (ID: 19601). The pattern of reelin interneurons in HF was compared to the pattern of iAβ-positive interneurons. The distributions of the two populations did not seem to coincide (data not shown).

4. DISCUSSION

4.1. Summary of main findings

The aim of this study was to investigate whether neuronal populations that are selectively vulnerable to accumulation of intracellular amyloid β (iAβ) in the initial stages of Alzheimer's disease (AD) are characterised by the presence of distinct molecular markers, with use of homozygous McGill-R-Thy1-APP transgenic rats. The first part focused on reelin-immunoreactive cells in layer II (LII) of entorhinal cortex (EC), an area that is early and severely affected in AD. We found a near complete overlap between iAβ- and reelin-immunoreactive cells in LII of both lateral (LEC) and medial (MEC) EC. By unbiased stereology we estimated the total number of cells double-positive for iAβ and reelin. Subsequent immunohistochemical analyses indicated that a proportion of reelin/iAβ-expressing cells in MEC LII were also positive for calbindin at six months, whereas in LII of LEC, reelin/iAβ-positive and calbindin-positive cells appeared to represent distinct neuronal populations.

In the second part of this thesis we established that inhibitory cells also express iAβ in the pre-plaque stage in the McGill-R-Thy1-APP rat model. iAβ-positive interneurons were observed in all subareas and most layers of both the hippocampal formation (HF) and parahippocampal region (PHR), but were most numerous in subiculum, CA1, CA3, and caudalmost portions of MEC. A subsequent quantitative analysis of subiculum revealed a significantly higher proportion of iAβ-positive interneurons in dorsal and intermediate than in ventral portions of subiculum.

Lastly, we found that both parvalbumin- and somatostatin-positive interneurons express iAβ in HF and PHR in the McGill-R-Thy1-APP rat model, indicating that iAβ-immunoreactive interneurons are not characterised by expression of one particular molecular marker.

4.2. Methodological considerations

4.2.1. The McGill-R-Thy1-APP rat model of Alzheimer's disease

The McGill-R-Thy1-APP rat model is a comprehensive model for AD amyloidosis. It displays temporal and spatial amyloid progression similar to the human disease condition (Leon et al., 2010), which makes it a suitable animal model for studies of the amyloid pathology of AD. However, to date, no reports on tau pathology in the McGill-R-Thy1-APP rat model have been published. The presence of

neurofibrillary tangles (NFTs) and a potential association between tau and amyloid would make the McGill-R-Thy1-APP rat a more complete model of AD. Both NFTs and cell loss correlate with severity of dementia (Arriagada et al., 1992; Bierer et al., 1995; Giannakopoulos et al., 2003). Thus, it would be of interest to investigate the potential expression of hyperphosphorylated tau proteins in this model using appropriate phospho-tau antibodies. At 18 months, cell death in the McGill-R-Thy1-APP rat model is only observed in subiculum (Heggland et al., 2015), whereas in human AD brains, early cell loss is usually more pronounced in other areas of HF and in EC (Gomez-Isla et al., 1996; West et al., 2004). More prominent cell loss would make the model a more faithful mimic of human AD, though there is still a possibility of cell loss at older ages.

Another potential shortcoming of the McGill-R-Thy1-APP rat model is the high variability in pathology between animals. This is evident both in amount of iAβ (e.g., Figure 3.2 in contrast to Figure 3.16, which show sections from two different six months old homozygous rats) and time of onset of plaque and plaque load (Heggland et al., 2015). For the first part of this study, in which we investigated the co-localisation of reelin and iAβ in LII of EC, entire age groups consisted of rats from the same litter or of the same sex, whereas other groups consisted of a mix of rats with different parents and sex (see section D.1. in Appendix D). Siblings will likely be more similar in pathology than rats from different litters. Thus, in light of the variable amyloid pathology between animals, more consistency in the use of rats with different parents would have improved the quality of the current study. There are no apparent sex differences in plaque pathology in the McGill-R-Thy1-APP rat model (Heggland et al., 2015), but an effect of sex can be seen in metabolite levels (Nilsen et al., 2014). To account for potential sex difference in iAβ-expression, rats in each group should also be mixed with regards to sex. However, as the spatiotemporal progression of pathology is similar between animals, these methodological weaknesses are not considered to have significantly affected the current results.

Finally, rats in our colony show plaque pathology from around nine months of age, whereas rats in the original colony expressed plaques already at six months (Leon et al., 2010). Ergo, our population has drifted slightly from the original. It would be interesting to do behavioural tests to establish whether individuals in our colony of McGill-R-Thy1-APP rats have memory impairments from three months as in the original colony, or if the 'clinical manifestations' of AD are delayed. However, as our rats display iAβ at age P6, and iAβ-accumulation but not plaque load correlates with cognitive deficits in AD (Billings et al., 2005; Knobloch et al., 2007), the delayed plaque accumulation is not considered to make McGill-R-Thy1-APP rats in our colony inferior model systems of AD pathology.

4.2.2. Reelin-immunoreactive cells in layer II of entorhinal cortex

One of the main concerns of the present study was the variability and weak signal-to-noise ratio of the polyclonal rabbit reelin antibody (see section 3.2.1.) and the high estimates of reelin-positive cells in LII of EC. The two filters used to visualise iAβ and reelin showed remarkably similar labelling in the fluorescent microscope, and the cell counts indicated a near complete overlap of iAβ-positive and reelin-positive cells in LII of both LEC and MEC. However, in subsequent confocal images of some of the stained sections, the co-localisation did not seem to be complete.

Imaging multiple fluorophores in one sample involves the possibilities that the excitation and emission signals overlap, i.e., that the fluorophores can be excited by the same wavelength and exhibit overlapping emission. This can cause so-called spectral bleed-through or cross-talk artefacts between the signals, which can be confused with co-localisation (North, 2006). As dyes for the secondary antibodies, we used Alexa fluorophores 488 and 546 for reelin and iAβ, respectively. These two dyes have a clear separation of peak excitation and emission wavelengths, but there is still a moderate level spectral overlap. A BP 450-490 filter was used to visualise Alexa fluorophore 488, and Alexa fluorophore 546 may be excited in this range if the intensity is strong enough, possibly producing emission with various intensity.

It is particularly important to control for bleed-through if the two fluorochromes appear to be nearly completely co-localised, such as was observed in the current study. It cannot be excluded that the Alexa fluorophore 546 was excited by the BP 450-490 filter, and that the signal was partly emission from this dye, particularly in the sections where the reelin-labelling was very poor. This was indicated by control images taken after the main experiments were performed. A single-labelled control with McSA1 and Alexa fluorophore 546 visualised by the BP 450-490 filter also suggested some spectral bleed-through from Alexa fluorophore 546 in the BP 450-490 filter (Figure 3.5). The problem is less pressing with a confocal microscope, as the excitation from the laser beam is close to monochromatic. Thus, the discrepancy between the fluorescent and confocal microscopes could be explained by the BP 450-490 filter showing iAβ-labelled cells instead of cells labelled with rabbit anti-reelin. However, it is likely that a lot of the background labelling is autofluorescence, as the same brightly stained 'spots' were also present in the BP 546/12 filter used to visualise iAβ (Figure 3.4 A, Figure 3.6 C). In the oldest animals, this may be caused by accumulated lipofuscin, which is autofluorescent and known to be a biomarker for ageing (Brunk and Terman, 2002). Nevertheless, fluorophores with well-separated spectral profiles, such as Alexa fluorophore 488 and 594, would have been more optimal.

Double-labelling with rabbit anti-reelin and the G10 clone of mouse anti-reelin, which is monoclonal and known to be specific for reelin (de Bergeyck et al., 1998), showed that there was good overlap between the two antibodies in LII of EC (Figure 3.3 and Supplementary Figure H.1). However, rabbit anti-reelin stained more cells than mouse anti-reelin in deep layers of EC and in other areas of HF and PHR. The full-length reelin peptide is cleaved at two sites, generating a number of different fragments (D'Arcangelo et al., 1995; Lambert de Rouvroit et al., 1999; Jossin et al., 2004). The G10 antibody binds to a portion of the N-terminal fragment of the full peptide (de Bergeyck et al., 1998). Full-length reelin and an additional three fragments are able to bind to ApoER2 and VldlR, and two of the additional fragments do not contain the N-terminus (Jossin et al., 2004). Rabbit anti-reelin is polyclonal and likely binds to epitopes on more fragments than G10. If these fragments include the two biologically active fragments not targeted by G10, rabbit anti-reelin could give a more 'complete' picture of the reelin distribution, although it is unclear how abundant the two additional fragments are. Alternatively, the antibody could bind to epitopes present on other molecules than reelin and thus produce non-specific labelling.

In addition to its possible non-specificity, the variability of the rabbit antibody is noteworthy. As this antibody is polyclonal, some variability due to mixing of immunoglobulin subtypes is expected. Monoclonal antibodies are made from a single clone of B lymphocytes, producing a single IgG subtype of antibodies and guaranteeing reproducibility between experiments. For polyclonal antibodies, immunising a new animal to produce more antibody will give slightly different results (Onley, 2007). This variability should be noticeable between batches of antibody, and not between sections stained simultaneously in the same antibody-containing solution. Pre-absorption of the antibody by incubating it with free reelin could have been done in order to determine possible non-specific labelling.

Previous estimates by unbiased stereological methods have yielded generally lower numbers of cells in LII than the ones obtained in the present study. Gatome et al. (2010) reported 57,900 cells in LII of MEC of one month old Wistar rats, approximately 67% of which were stellate cells. The stellate cell population is often assumed to correspond to the population of reelin-expressing cells in MEC LII, as both populations project to DG and CA3 (Tamamaki and Nojyo, 1993; Varga et al., 2010), in which case the study of Gatome et al. would have yielded approximately 39,000 reelin-positive cells. In other words, our estimate of reelin-positive cells in MEC LII at one month of age exceeds that of Gatome et al. by 72,000. In another study, ~64,600 and ~42,700 cell were reported in LII of MEC and LEC, respectively, of aged rats (Merrill et al., 2001). The latter numbers are comparable to a study by Mulders et al. (1997), in which ~66,000 cells were estimated in MEC LII and ~46,000 were estimated in LEC LII. Cell estimates from our lab of all layers of MEC and LEC are on the high end, with mean

~508,000 in MEC and ~349,000 in LEC of 18 months old wild-type Wistar rats (Heggland et al., 2015). Others have estimated ~380,000 neurons in LEC and ~260,000 in MEC of aged rats (Rapp et al., 2002).

Differences in delineation criteria will most likely have contributed to the discrepancies. Regardless of this, if 50-70% of principal cells in MEC LII are reelin-positive cells or stellate cells, as has been reported (Gatome et al., 2010; Varga et al., 2010; Tang et al., 2014), our estimate of total cell number in MEC LII would still be high. Though unlikely, our large estimate may be explained by reelin being co-localised with calbindin, as we observed for a proportion of cells. As the reelin- and calbindin-expressing populations are considered two separate neuronal populations in EC LII, the co-localisation we observe could be due to alterations in the neurochemical profile of LII principal cells in transgenic McGill-R-Thy1-APP rats. This possibility will be discussed in greater detail in the sections below. One alternative explanation to the high estimate is that we included the most superficial portions of layer III in the delineation of MEC. Our high estimates may also indicate that the rabbit antibody labelled more than reelin-positive cells, or that we in some instances have experienced spectral bleed-through or included autofluorescence as cells. For LEC LII, our cell estimates are more comparable to the above studies. Others have reported that all LII principal cells are reelin-positive (Ramos-Moreno et al., 2006), although this is probably attributable to a more conservative delineation of LII, as we and others have observed calbindin-positive and reelin-negative cells in deep portions of LEC LII (Wouterlood, 2002; our own unpublished observations). If the proportion of principal cells positive for reelin is similar between LEC and MEC, our cell estimate for the reelin-positive cells in LEC is still higher than what others estimate. This could again be explained by delineation criteria or that we generally estimate more cells than other groups in EC as a whole.

Based on the above arguments, we should have eliminated the brains in which the reelin-labelling was poor and only counted cells in tissue with good reelin-labelling. With all rounds of immunohistochemistry, we should have included control tissue with single-staining for iAβ and reelin to test for spectral bleed-through. To get a clear impression of the distribution of reelin- and calbindin-expression in LII, it would be beneficial to perform stereological estimations of these two populations in LEC and MEC using our delineation criteria, both in McGill-R-Thy1-APP transgenic rats and in wild-type controls.

When labelled using mouse anti-reelin, reelin-immunoreactive cells in EC LII show a similar distribution pattern to that of iAβ in LII of both LEC and MEC. Further, the two reelin antibodies show a substantial overlap in EC LII, indicating co-localisation between iAβ reelin in this layer. Thus, despite some

methodological drawbacks, our results suggest that reelin-positive principal cells in LII of EC express iAβ in homozygous McGill-R-Thy1-APP rats of ages P15 to six months.

4.3. Role of principal cells in layer II of entorhinal cortex in Alzheimer's disease

4.3.1. Reelin is involved in synaptic plasticity and associates with amyloid β

Numerous studies have emphasised the potential interaction between reelin and Aβ, and an early co-localisation of the two proteins in EC LII principal cells could have important consequences for the entorhinal-hippocampal network. Reelin deficiency has been found in human AD cases, including in principal cells in LII of EC (Chin et al., 2007; Herring et al., 2012). The deficiency has been suggested as a cause of amyloidosis (Kocherhans et al., 2010), in line with recent evidence that overexpression of reelin reduces the toxicity of Aβ42 and rescues cognitive impairment in transgenic mice (Pujadas et al., 2014). Increased levels of reelin has been found in the frontal cortex of AD patients (Botella-Lopez et al., 2006), and increased levels of the 180-kDa fragment has been found in cerebrospinal fluid of AD patients (Saez-Valero et al., 2003) . A late upregulation of reelin could be a compensatory mechanism to account for less active reelin in other areas of the brain. Alternatively, as the 180-kDa fragment is unable to bind to the two reelin receptors, ApoER2 and VldlR (Jossin et al., 2004), higher levels of this isoform could indicate an accumulation of dysfunctional reelin. Further, reelin does not form physiologically active dimers and has decreased binding capacity to ApoER2 in the presence of Aβ (Cuchillo-Ibanez et al., 2013), and glycosylation patterns of reelin are altered in human AD brains (Botella-Lopez et al., 2010). This poses the question whether iAβ accumulation in reelin-positive cells, as indicated by the present study, disrupt the properties of reelin, ultimately resulting in reduced levels of the biologically active forms and an inability of reelin to protect against Aβ toxicity.

Principal cells in EC LII are the main origin of cells of the perforant path, the main input from EC to HF (Witter, 2010). Altered properties of reelin in LII of EC, induced by accumulation of potentially toxic iAβ, could lead to disrupted synaptic signalling from LII to downstream targets in dentate gyrus (DG) and CA3. Reelin signalling and its activity at synapses is linked to the activity of Aβ and apolipoprotein E (ApoE; Herz and Chen, 2006), and reelin increases LTP by regulating trafficking of both NMDA and AMPA receptors (Weeber et al., 2002; Beffert et al., 2005), while Aβ oligomers inhibit LTP (Walsh et al., 2002). Thus, based on the role of reelin in synaptic plasticity and the association between Aβ and reelin, along with the expression of reelin in principal cells in LII of EC, plasticity of the entorhinal-hippocampal network could initially change in AD as a consequence of pathology arising in reelin-

positive cells in LII of EC. Mechanistic interaction of Aβ and reelin at the subcellular level in principal cells in LII of EC, including in their presynaptic terminals, should be studied in order to determine this.

Interestingly, reelin-positive plaques are present in healthy aged rodents and primates, and co-localise with non-fibrillary Aβ in triple transgenic AD mice (Knuesel et al., 2009) and in aged wild-type mice (Doehner et al., 2010). It would be of interest to investigate potential changes in reelin levels or the formation of reelin plaques in EC LII of older McGill-R-Thy1-APP rats, and whether they associate with Aβ. This would shed light on the potential alteration in reelin in EC and the consequence this could have for disruption of the entorhinal-hippocampal network.

4.3.2. Calbindin-expression could be altered in Alzheimer's disease

We found co-localisation between reelin and calbindin and between iAβ and calbindin in a subset of cells in LII of MEC, suggesting that iAβ is not strictly restricted to the reelin-positive cells in LII. According to other studies, the reelin- and calbindin-expressing cells largely represent two separate neuronal populations, with little overlap between them (Varga et al., 2010; Berndtsson, 2013; Tang et al., 2014). More tests as well as comparisons with age-matched controls were not performed in this project due to time constraints, but this should have been done in order to validate our observations. Increased staining intensity of calbindin in LII and LIII of EC has been reported in human AD brains compared to control subjects, along with morphological changes in interneurons expressing calbindin (Mikkonen et al., 1999). Thus, the observed co-localisation between iAβ and calbindin could be due to alterations in the neurochemical profile of LII principal cells in transgenic McGill-R-Thy1-APP rats and in AD in general.

Decreased levels of calbindin in granule cells of DG has been found in human AD cases (Stefanits et al., 2014) and in hAPP mice, in the latter case correlated with Aβ42 levels (Palop et al., 2003). Neurons expressing high levels of calbindin and other calcium-binding proteins are less affected in AD (Moon et al., 2012; but see section 4.4.1). Further, calbindin can protect neurons against Aβ-induced toxicity (Guo et al., 1998), and in 5XFAD mice crossed with calbindin knock-out mice, there was a reduction in number of NeuN-positive cells[4] in subiculum compared to 5XFAD littermates (Kook et al., 2014). Calbindin is a calcium-binding protein and thus has an important role in controlling calcium homeostasis. Calcium signalling is tightly related to synaptic plasticity and likely to learning and memory (Berridge, 1998). Upregulation of calcium signalling in AD has been suggested as a

[4] Neuronal nuclei (NeuN) is a neuron-specific protein that can be used as a biomarker for neurons.

consequence of Aβ toxicity and to contribute to cell death and decline in memory (Berridge, 2011), and altered calbindin expression could be involved in this. Hypothetically, reduced or altered reelin activity in EC LII in early AD could lead to reduced plasticity in the entorhinal-hippocampal network, as discussed above, which in turn could induce upregulation or alteration of the cellular distribution of calbindin as a compensatory mechanism. The role of calbindin-positive cells in LII of EC is still under investigation, and it is still unknown where the majority of calbindin-expressing cells in MEC LII project. Varga et al. (2010) proposed that calbindin-expressing MEC LII cells project to the contralateral MEC, results that have not been reproducible by our group (Berndtsson, 2013; Gianatti, 2015). In addition to influencing the local cellular environment, an alteration in the calbindin composition or an accumulation of iAβ in calbindin-immunoreactive cells in MEC LII could have important implications for the communication of MEC with other areas in AD, whatever areas these may be.

4.4. Interneurons in Alzheimer's disease

The current study found that iAβ-immunoreactivity is not restricted to principal cells in HF and PHR in the McGill-R-Thy1-APP rat model and is thus the first to report amyloid-related pathology in interneurons in this model. Aβ-immunoreactive interneurons have been identified in the cortex of human AD cases (Mochizuki et al., 2000), and studies have found accumulation of iAβ in interneurons in piriform cortex and LEC of transgenic mice and human AD subjects (Saiz-Sanchez et al., 2012; Saiz-Sanchez et al., 2014).

4.4.1. Relevance for network dysfunctions

The finding that both principal cells and interneurons are affected by amyloid pathology has important implications for network dysfunctions and destabilisation. Interneurons exert tight inhibitory control of networks of principal cells, and have long been recognised to be involved in maintaining stable states in neural networks and producing synchrony of principal cells. Within HF, interneuron firing is coupled to network oscillations (Mann and Paulsen, 2007). Interneurons probably play an important role in learning and memory (Andrews-Zwilling et al., 2012), and loss of interneurons in transgenic AD mice along with memory impairments has been observed (Krantic et al., 2012; Loreth et al., 2012). Loss of inhibition, either by loss of interneurons or by dysfunctional properties of interneurons, could induce increased excitability as well as destabilisation of neural networks. In relation to this, development of AD in humans is accompanied by an increased risk of epileptic activity (Palop and Mucke, 2009), and hyperexcitability has also been identified in transgenic hAPP mice (Palop et al., 2007; Busche et al.,

2008; Minkeviciene et al., 2009). Aged transgenic mice have impaired short-term plasticity accompanied by hyperexcitability and inability of interneurons to fire action potentials in DG (Hazra et al., 2013). Instability of networks is likely also related to destabilisation and degradation of synapses, which has been suggested as a toxic effect of soluble Aβ (Gouras et al., 2010). Accumulation of iAβ in interneurons in the pre-plaque stage in AD will possibly contribute to changes in interneuron properties, which could lead to hyperexcitability, synapse pathology, and destabilisation of cellular networks, ultimately resulting in impairments in memory and cognition.

Interestingly, the ε4 allele of the *APOE* gene, the strongest genetic risk factor for sporadic AD, has been suggested to be linked to epileptic activity (Ponomareva et al., 2008; Palop and Mucke, 2009). The ApoE4 protein has been found to cause interneuron loss in hilus of DG along with spatial learning impairments (Andrews-Zwilling et al., 2010; Knoferle et al., 2014), and to induce GABAergic dysfunction, leading to impaired hippocampal neurogenesis (Li et al., 2009a). The association between ApoE4 and AD is still under investigation, and it may or may not involve Aβ (Mahley et al., 2006). ApoE4 is well known to disrupt the ability of reelin to bind to its receptors (D'Arcangelo et al., 1999; Chen et al., 2010). Thus, ApoE4 is an interesting link between reelin, interneurons, and network dysfunctions in early AD. We were not able to investigate the potential expression of iAβ in reelin-expressing interneurons, but this and the mechanisms by which reelin, Aβ and ApoE4 interact in interneurons warrant further study.

4.4.2. Interneuron subtypes could have different vulnerability in Alzheimer's disease

Interneurons express a wide range of neurochemical characteristics, and subtypes can be identified by the presence of certain proteins, such as neuropeptides or calcium-binding proteins. The current study found that iAβ is expressed in both parvalbumin- and somatostatin-positive interneurons in HF and PHR. The involvement of calcium-binding protein-expressing neurons in AD is somewhat undetermined, and conflicting reports exist regarding whether calcium-binding proteins protect against (Hof et al., 1993; Iritani et al., 2001; Moon et al., 2012) or increase vulnerability (Brady and Mufson, 1997; Popovic et al., 2008; Baglietto-Vargas et al., 2010; Takahashi et al., 2010) to AD and amyloid pathology. Our findings that iAβ-immunoreactivity is present in parvalbumin-positive interneurons in several areas and that calbindin-positive cells in LII of MEC express iAβ supports the view that the presence of calcium-binding proteins does not fully protect against the neuropathological changes of AD. Parvalbumin-expressing interneurons represent the largest class of interneurons in HF, PHR, and the neocortex, and they have various properties and functions (Hu et al., 2014). Generally, their morphology is basket- or chandelier-like, and they are fast-spiking and exert tight precision in the

control of their targets. Loss of this, perhaps as a result of accumulation of iAβ in parvalbumin-positive cells, could contribute to destabilised networks in AD. Indeed, Verret et al. (2012) suggested that dysfunction of parvalbumin-positive interneurons contribute to spontaneous oscillatory activity and reduced gamma oscillatory activity, leading to network dysfunctions in hAPP mice. In addition to parvalbumin and calbindin, the third major calcium-binding protein present in interneurons is calretinin. Due to time constraints, we did not investigate the potential expression of iAβ in calbindin- or calretinin-positive interneurons in the McGill-R-Thy-1-APP model, but this would be of interest in order to determine whether there is a difference in the abilities of the calcium-binding proteins to protect against Aβ.

iAβ also co-localised with somatostatin in HF and PHR in the current study, although less so than parvalbumin. It should be noted that parvalbumin is present in a larger proportion of interneurons, and this may yield a biased impression of the relative expression of iAβ in the two interneuron populations. Quantitative assessments should be carried out in order to determine the exact vulnerability to iAβ-accumulation of parvalbumin- or somatostatin-expressing interneurons, respectively. Lower levels of somatostatin in the cerebral cortex and cerebrospinal fluid has long been known to be a typical feature of AD patients, and somatostatin is a key regulator of neprilysin, a degrading enzyme of Aβ activity (Hama and Saido, 2005). Our findings of co-localisation between somatostatin and Aβ confirm what has been found in transgenic mice models and human AD tissue (Saiz-Sanchez et al., 2010; Saiz-Sanchez et al., 2012; Saiz-Sanchez et al., 2014), and support the impression that somatostatin is involved in early AD pathology.

4.5. Amyloid pathology in the entorhinal-hippocampal network

4.5.1. The role of subiculum and subicular interneurons in Alzheimer's disease

In the McGill-R-Thy1-APP rat model, dorsal subiculum is the first area to express amyloid plaques at approximately nine months, and it is also the area that shows the highest plaque load at later ages. Additionally, at 18 months, there is a reduction in neuron number in subiculum compared to control rats (Heggland et al., 2015). The current thesis found strong iAβ-labelling in subiculum, both in principal cells and interneurons, at all ages investigated and present already at P6. Subiculum has also been found to be early affected by Aβ pathology and cell loss in transgenic mice models of AD (Oakley et al., 2006; Trujillo-Estrada et al., 2014), and lesioning subiculum in six week old transgenic mice resulted in reduced Aβ pathology in connected areas at three and six months of age (George et al., 2014). Together

with the current findings, this suggests subiculum as an important structure in early AD, and additional experiments, such as *in vivo* electrophysiological recordings, should be performed in order to determine the extent of pathological changes in this area.

Compared to other areas of HF, both microcircuits and functions of subiculum are not as well described in the literature. Subiculum represents an important output structure of HF, and it has been suggested that it integrates, segregates, and distributes information flow through its parallel and reciprocal connections with areas of PHR (Naber et al., 2000; Kloosterman et al., 2003). Subpopulations of interneurons in subiculum appear to be similar to interneuron types in CA1 (Cappaert et al., 2015). Although not much is known about their properties, interneurons of subiculum are likely involved in restraining and modulating hippocampal output (Menendez de la Prida, 2003; Panuccio et al., 2012). Loss of subicular interneurons is correlated with temporal lobe epilepsy in rats (Knopp et al., 2008). If iAβ accumulation leads to dysfunctional interneurons in subiculum, this could have important implications for the epileptiform activity seen in transgenic animals and human patients of AD, as well as for the ability of subiculum to segregate and distribute incoming and outgoing information.

4.5.2. Topographical segregation of functions and projections in the entorhinal-hippocampal network

Our quantitative investigation showed that the proportion of iAβ-positive interneurons in dorsal-intermediate portions of subiculum was significantly higher than ventral portions at both one and six months in homozygous McGill-R-Thy1-APP rats. Similarly, qualitative assessments indicated more iAβ in interneurons in dorsal than ventral CA1 and CA3. Several studies imply a dorso-ventral segregation of function, both in subiculum (O'Mara, 2005) and in HF as a whole (Moser and Moser, 1998). It was early found that lesions in antero-dorsal but not postero-ventral HF results in reduced maze learning in rats (Hughes, 1965), observations that were confirmed later (Moser et al., 1995). Lesions in ventral subiculum results in impaired conditional freezing in rats (Maren, 1999). These and other studies have promoted the view that the dorsal part of HF (posterior in primates) is mostly involved in spatial learning, whilst the ventral part (anterior in primates) plays a major role in neuroendocrine and autonomic responses, including anxiety-related behaviour (Moser and Moser, 1998; Bannerman et al., 2004; O'Mara et al., 2009). It has also been suggested that dorsal and ventral portions perform different analyses and use different computational algorithms to process information (Moser and Moser, 1998). Our finding that dorsal subiculum and dorsal HF in general is more severely affected by Aβ pathology than ventral HF in the McGill-R-Thy1-APP rat model may indicate that some intrinsic characteristics or properties of the dorsally located cells render them more vulnerable to accumulation

of Aβ. In relation to the present study, lower levels of both GABA and glutamate has been found in dorsal HF in the McGill-R-Thy1-APP rat model (Nilsen et al., 2012). The dorsal, intermediate, and ventral portions of the CA fields differ in their expression of several genes, suggesting that they may be genetically destined to serve different functions (Dong et al., 2009; Fanselow and Dong, 2010). Consequently, the presence of distinct proteins may make the dorsal, intermediate, and ventral portions differently susceptible to disease, emphasising the need for characterisation of molecular markers that can help identify selective vulnerability.

Alternatively, the increased vulnerability of dorsal subiculum and HF could be due to connections with other areas. In addition to genetic and functional segregation within HF, connectivity between HF and PHR shows segregation along the various topographical axes. EC is commonly divided into three bands or zones of connections, and the different portions along the long axis of HF are connected to the distinct bands (Canto et al., 2008). Dorsal subiculum and HF reciprocally connects to lateral and dorsal parts of EC (Kloosterman et al., 2003), also referred to as the dorsolateral band, an area of EC with strong iAβ-labelling in the McGill-R-Thy1-APP rat model. Lateral areas of EC are also affected by pathology earlier than medial in human AD brains (Braak et al., 2006; Khan et al., 2014). Together, the abovementioned studies and the current findings suggests increased vulnerability of these areas and is in line with the impairment in learning and retaining new information that are amongst the first clinical manifestations of AD.

In relation to this, our group has recently described a spatiotemporal progression of plaque pathology in the McGill-R-Thy1-APP rat model, which follows anatomically interconnected regions (Heggland et al., 2015). Similar anatomical progression of amyloid pathology has been observed in transgenic mice models of AD (Ronnback et al., 2012; George et al., 2014). As such, the strong iAβ-labelling we see in dorsal subiculum and HF and in dorsolateral EC could be due to transsynaptic spread of Aβ between these areas, as has been shown to occur in other AD models (Buxbaum et al., 1998; Harris et al., 2010; Nath et al., 2012). Some authors speculate whether cell-to-cell propagation of misfolded Aβ42 follows a prion-like mechanism, whereby increased extracellular Aβ42 from degenerated synapses or neurites can upregulate or 'seed' intracellular Aβ42 in nearby cells (Gouras et al., 2005; Gouras et al., 2010). However, this does not explain why Aβ increases intracellularly in the first place, nor does it explain whether certain properties of some cell populations render them more vulnerable to Aβ uptake and accumulation or if it is a stochastic process.

4.6. Translational value and future directions

The ultimate reason for using transgenic animals as disease models is to gain insight into pathological mechanisms that can be translated into the human condition and shed light on potential therapeutic interventions. The relevance of the McGill-R-Thy1-APP rat model has been discussed in the beginning of this section. Importantly, unpublished results from our lab indicate that iAβ is expressed in reelin-positive principal cells in LII of EC in human AD brains at Braak stages I-III, suggesting that this is also a feature of AD and illustrating the value of the McGill-R-Thy1-APP rat model. Since the neuropathological changes in the human AD brain are very severe by the time the disease starts to manifest itself clinically, early detection of disease processes is crucial for potential therapeutic inventions to be effective. Identifying cellular markers that render cells vulnerable to the early pathology is a vital part of this.

The present thesis focuses on specific cell types as early targets of amyloid pathology in HF and PHR, and presents evidence that iAβ accumulates in principal cells and interneurons that cannot be characterised by the expression of a single molecular marker. However, it could be that although iAβ accumulates in cells characterised by a number of different markers, pathological changes such as disruption of synapses only occur in the presence of certain proteins, both in the McGill-R-Thy1-APP rat model and in the human AD brain. For example, reelin has been shown to be associated with Aβ in several studies. In LII of EC, the reelin-positive cell population could be more vulnerable to disease than the calbindin-positive cells simply because they express reelin, even if calbindin cells also accumulate iAβ. The mere presence of iAβ does not necessarily mean that a cell undergoes pathological changes, especially since it has been suggested that the effect of soluble Aβ is concentration-dependent (Palop and Mucke, 2010). In order to establish this, mechanisms of interaction between Aβ and other molecules would need to be studied.

It could also be that certain other cellular characteristics, such as morphology or electrophysiological properties, or the local cellular environment, render some cells more vulnerable to undergoing physiological changes than others. Interneurons in HF and in the cortex are not solely defined by their molecular markers, and the presence of markers alone does not identify an interneuron class (Somogyi and Klausberger, 2005). Interneurons show incredible diversity in regards to morphology, electrophysiology, and connectivity, and at least 21 distinct types are recognised in CA1 (Somogyi, 2010). As such, it would be interesting to know whether interneurons that are particularly vulnerable to early amyloid pathology can be distinguished based on something other than chemical markers, for instance their electrophysiological properties or their innervation of principal cells. This could shed

new light on destabilisation of neural networks in AD. Thus, assessing the presence of iAβ by immunohistochemistry should be combined with other experimental techniques such as electrophysiological recordings or characterisations of morphology. Based on the findings that dorsal HF is more severely affected by iAβ, further investigations into this area would be a natural starting point.

Another natural follow up to this study would be to investigate potential changes in the neurochemical profiles of the cell populations investigated in this study. Loss of both principal cell and interneuron markers have been described in transgenic mice models and human subjects of AD. Although we have assessed cell loss in the McGill-R-Thy1-APP rat model (Heggland et al., 2015), we have not looked at the loss of markers. Identification of the potential up- or downregulation of proteins would also be useful in order to facilitate early detection of AD.

It appears that the portions of the hippocampal-entorhinal network that are most important for memory and spatial learning are more heavily affected by amyloid-related pathology in early-phase AD in the McGill-R-Thy1-APP rat model, similar to what we know from human studies. The presence of iAβ and the possible transmission of amyloid pathology between interconnected anatomical areas does not explain what renders cells vulnerable to iAβ accumulation in the first place. It is reasonable to assume that differential genetic expression patterns in dorsal HF and dorsolateral portions of EC are involved. Since we and others (Leon et al., 2010) observe iAβ at one week postnatal in the McGill-R-Thy1-APP rat model, it could be interesting to investigate potential iAβ even earlier, perhaps even during *in utero* development, in order to establish when and where – and in which cell types – the very first AD-related changes occur in this rat model.

5. CONCLUSIONS

The results of this study suggests that the reelin-positive principal cells in LII of EC are heavily immunoreactive to iAβ in the pre-plaque stage in homozygous McGill-R-Thy1-APP rats. As the reelin-expressing cells project to hippocampus and reelin plays an important role in synaptic plasticity, we postulate that iAβ-accumulation in this neuronal population could have important effects on plasticity in the entorhinal-hippocampal network. We also found iAβ-immunoreactivity in calbindin-positive cells in LII of caudal and dorsal portions of MEC, which may be indicative of altered neurochemical profiles of principal cells in this area in AD.

We have further shown that interneurons in all subareas of HF and PHR express iAβ at the pre-plaque stage in the McGill-R-Thy1-APP rat model, and that a significantly larger portion of interneurons in dorsal and intermediate regions of subiculum are immunoreactive to iAβ than in ventral regions. This suggests particular vulnerability to iAβ of cells in dorsal parts of HF, and could also be linked to topography of connections in the entorhinal-hippocampal network. The finding that both principal cells and interneurons are affected heavily by iAβ in HF and PHR supports the already established idea that AD not only affects single cells or synapses, but also local assemblies and larger networks of neurons.

Taken together, the results suggest that iAβ is expressed in a large number of principal cells and interneurons in HF and PHR at early ages in the McGill-R-Thy1-APP rat model of AD, and that the interneurons cannot be singled out based on the presence of the molecular markers investigated. Thus, it may be that early affected cells are heterogeneous in regards to their neurochemical profiles and that some other properties are critical to their vulnerability to iAβ. The results of the present study shed light on neurons that are vulnerable to pathology in the early stages of AD, which is an important step to explain how some functions and areas of the brain are severely altered later in the disease whilst the functionality of other areas persist.

REFERENCES

Alonso, A. & Klink, R. 1993. Differential electroresponsiveness of stellate and pyramidal-like cells of medial entorhinal cortex layer II. *Journal of Neurophysiology,* 70:1**,** 128-43.

Andersen, B. B. & Gundersen, H. J. 1999. Pronounced loss of cell nuclei and anisotropic deformation of thick sections. *Journal of Microscopy,* 196:1**,** 69-73.

Andrews-Zwilling, Y., Bien-Ly, N., Xu, Q., Li, G., Bernardo, A., Yoon, S. Y., Zwilling, D., Yan, T. X., Chen, L. & Huang, Y. 2010. Apolipoprotein E4 causes age- and Tau-dependent impairment of GABAergic interneurons, leading to learning and memory deficits in mice. *Journal of Neuroscience,* 30:41**,** 13707-17.

Andrews-Zwilling, Y., Gillespie, A. K., Kravitz, A. V., Nelson, A. B., Devidze, N., Lo, I., Yoon, S. Y., Bien-Ly, N., Ring, K., Zwilling, D., Potter, G. B., Rubenstein, J. L., Kreitzer, A. C. & Huang, Y. 2012. Hilar GABAergic interneuron activity controls spatial learning and memory retrieval. *PloS one,* 7:7**,** e40555.

Arriagada, P. V., Growdon, J. H., Hedley-Whyte, E. T. & Hyman, B. T. 1992. Neurofibrillary tangles but not senile plaques parallel duration and severity of Alzheimer's disease. *Neurology,* 42:3**,** 631-9.

Baglietto-Vargas, D., Moreno-Gonzalez, I., Sanchez-Varo, R., Jimenez, S., Trujillo-Estrada, L., Sanchez-Mejias, E., Torres, M., Romero-Acebal, M., Ruano, D., Vizuete, M., Vitorica, J. & Gutierrez, A. 2010. Calretinin interneurons are early targets of extracellular amyloid-beta pathology in PS1/AbetaPP Alzheimer mice hippocampus. *Journal of Alzheimer's disease,* 21:1**,** 119-32.

Bannerman, D. M., Rawlins, J. N., Mchugh, S. B., Deacon, R. M., Yee, B. K., Bast, T., Zhang, W. N., Pothuizen, H. H. & Feldon, J. 2004. Regional dissociations within the hippocampus--memory and anxiety. *Neuroscience and Biobehavioral Reviews,* 28:3**,** 273-83.

Beffert, U., Weeber, E. J., Durudas, A., Qiu, S., Masiulis, I., Sweatt, J. D., Li, W. P., Adelmann, G., Frotscher, M., Hammer, R. E. & Herz, J. 2005. Modulation of synaptic plasticity and memory by Reelin involves differential splicing of the lipoprotein receptor Apoer2. *Neuron,* 47:4**,** 567-79.

Berndtsson, C. H. 2013. *The Specificity of Output from Medial Entorhinal Cortex.* MSc in Neuroscience Master Thesis, Norwegian University of Science and Technology (NTNU).

Berridge, M. J. 1998. Neuronal calcium signaling. *Neuron,* 21:1**,** 13-26.

Berridge, M. J. 2011. Calcium signalling and Alzheimer's disease. *Neurochemical Research,* 36:7**,** 1149-56.

Bierer, L. M., Hof, P. R., Purohit, D. P., Carlin, L., Schmeidler, J., Davis, K. L. & Perl, D. P. 1995. Neocortical neurofibrillary tangles correlate with dementia severity in Alzheimer's disease. *Archives of Neurology,* 52:1**,** 81-8.

Billings, L. M., Oddo, S., Green, K. N., Mcgaugh, J. L. & Laferla, F. M. 2005. Intraneuronal Abeta causes the onset of early Alzheimer's disease-related cognitive deficits in transgenic mice. *Neuron,* 45:5**,** 675-88.

Botella-Lopez, A., Burgaya, F., Gavin, R., Garcia-Ayllon, M. S., Gomez-Tortosa, E., Pena-Casanova, J., Urena, J. M., Del Rio, J. A., Blesa, R., Soriano, E. & Saez-Valero, J. 2006. Reelin expression and glycosylation patterns are altered in Alzheimer's disease. *Proceedings of the National Academy of Sciences of the United States of America,* 103:14**,** 5573-8.

Botella-Lopez, A., Cuchillo-Ibanez, I., Cotrufo, T., Mok, S. S., Li, Q. X., Barquero, M. S., Dierssen, M., Soriano, E. & Saez-Valero, J. 2010. Beta-amyloid controls altered Reelin expression and processing in Alzheimer's disease. *Neurobiology of Disease,* 37:3**,** 682-91.

Braak, H., Alafuzoff, I., Arzberger, T., Kretzschmar, H. & Del Tredici, K. 2006. Staging of Alzheimer disease-associated neurofibrillary pathology using paraffin sections and immunocytochemistry. *Acta Neuropathologica,* 112:4**,** 389-404.

Braak, H. & Braak, E. 1985. On areas of transition between entorhinal allocortex and temporal isocortex in the human brain. Normal morphology and lamina-specific pathology in Alzheimer's disease. *Acta Neuropathologica,* 68:4**,** 325-32.

Brady, D. R. & Mufson, E. J. 1997. Parvalbumin-immunoreactive neurons in the hippocampal formation of Alzheimer's diseased brain. *Neuroscience,* 80:4**,** 1113-25.

Brunk, U. T. & Terman, A. 2002. Lipofuscin: mechanisms of age-related accumulation and influence on cell function. *Free Radical Biology & Medicine,* 30:5, 611-619.

Busche, M. A., Eichhoff, G., Adelsberger, H., Abramowski, D., Wiederhold, K. H., Haass, C., Staufenbiel, M., Konnerth, A. & Garaschuk, O. 2008. Clusters of hyperactive neurons near amyloid plaques in a mouse model of Alzheimer's disease. *Science,* 321:5896**,** 1686-9.

Buxbaum, J. D., Thinakaran, G., Koliatsos, V., O'callahan, J., Slunt, H. H., Price, D. L. & Sisodia, S. S. 1998. Alzheimer amyloid protein precursor in the rat hippocampus: transport and processing through the perforant path. *Journal of Neuroscience,* 18:23**,** 9629-37.

Canto, C. B. & Witter, M. P. 2012a. Cellular properties of principal neurons in the rat entorhinal cortex. I. The lateral entorhinal cortex. *Hippocampus,* 22:6**,** 1256-76.

Canto, C. B. & Witter, M. P. 2012b. Cellular properties of principal neurons in the rat entorhinal cortex. II. The medial entorhinal cortex. *Hippocampus,* 22:6**,** 1277-99.

Canto, C. B., Wouterlood, F. G. & Witter, M. P. 2008. What does the anatomical organization of the entorhinal cortex tell us? *Neural Plasticity,* 2008**,** 381243.

Cappaert, N. L. M., Van Strien, N. M. & Witter, M. P. 2015. Hippocampal Formation. *In:* Paxinos, G. (ed.) *The Rat Nervous System.* 4 ed.: Academic Press, Elsevier.

Casas, C., Sergeant, N., Itier, J. M., Blanchard, V., Wirths, O., Van Der Kolk, N., Vingtdeux, V., Van De Steeg, E., Ret, G., Canton, T., Drobecq, H., Clark, A., Bonici, B., Delacourte, A., Benavides, J., Schmitz, C., Tremp, G., Bayer, T. A., Benoit, P. & Pradier, L. 2004. Massive CA1/2 neuronal loss with intraneuronal and N-terminal truncated Abeta42 accumulation in a novel Alzheimer transgenic model. *The American Journal of Pathology,* 165:4**,** 1289-300.

Cenci, M. A., Whishaw, I. Q. & Schallert, T. 2002. Animal models of neurological deficits: how relevant is the rat? *Nature reviews. Neuroscience,* 3:7**,** 574-9.

Chen, Y., Durakoglugil, M. S., Xian, X. & Herz, J. 2010. ApoE4 reduces glutamate receptor function and synaptic plasticity by selectively impairing ApoE receptor recycling. *Proceedings of the National Academy of Sciences of the United States of America,* 107:26**,** 12011-6.

Chin, J., Massaro, C. M., Palop, J. J., Thwin, M. T., Yu, G. Q., Bien-Ly, N., Bender, A. & Mucke, L. 2007. Reelin depletion in the entorhinal cortex of human amyloid precursor protein transgenic mice and humans with Alzheimer's disease. *Journal of Neuroscience,* 27:11**,** 2727-33.

Cohen, R. M., Rezai-Zadeh, K., Weitz, T. M., Rentsendorj, A., Gate, D., Spivak, I., Bholat, Y., Vasilevko, V., Glabe, C. G., Breunig, J. J., Rakic, P., Davtyan, H., Agadjanyan, M. G., Kepe, V., Barrio, J. R., Bannykh, S., Szekely, C. A., Pechnick, R. N. & Town, T. 2013. A transgenic Alzheimer rat with plaques, tau pathology, behavioral impairment, oligomeric abeta, and frank neuronal loss. *Journal of Neuroscience,* 33:15**,** 6245-56.

Couey, J. J., Witoelar, A., Zhang, S. J., Zheng, K., Ye, J., Dunn, B., Czajkowski, R., Moser, M. B., Moser, E. I., Roudi, Y. & Witter, M. P. 2013. Recurrent inhibitory circuitry as a mechanism for grid formation. *Nature Neuroscience,* 16:3**,** 318-24.

Crowther, R. A. 1991. Straight and paired helical filaments in Alzheimer disease have a common structural unit. *Proceedings of the National Academy of Sciences of the United States of America,* 88:6**,** 2288-92.

Cuchillo-Ibanez, I., Balmaceda, V., Botella-Lopez, A., Rabano, A., Avila, J. & Saez-Valero, J. 2013. Beta-amyloid impairs reelin signaling. *PloS one,* 8:8**,** e72297.

D'arcangelo, G., Homayouni, R., Keshvara, L., Rice, D. S., Sheldon, M. & Curran, T. 1999. Reelin is a ligand for lipoprotein receptors. *Neuron,* 24:2**,** 471-9.

D'arcangelo, G., Miao, G. G., Chen, S. C., Soares, H. D., Morgan, J. I. & Curran, T. 1995. A protein related to extracellular matrix proteins deleted in the mouse mutant reeler. *Nature,* 374:6524**,** 719-23.

De Bergeyck, V., Naerhuyzen, B., Goffinet, A. M. & Lambert De Rouvroit, C. 1998. A panel of monoclonal antibodies against reelin, the extracellular matrix protein defective in reeler mutant mice. *Journal of Neuroscience Methods,* 82**,** 17-24.

De Calignon, A., Polydoro, M., Suarez-Calvet, M., William, C., Adamowicz, D. H., Kopeikina, K. J., Pitstick, R., Sahara, N., Ashe, K. H., Carlson, G. A., Spires-Jones, T. L. & Hyman, B. T. 2012. Propagation of tau pathology in a model of early Alzheimer's disease. *Neuron,* 73:1**,** 685-97.

deToledo-Morrell, L., Stoub, T. R., Bulgakova, M., Wilson, R. S., Bennett, D. A., Leurgans, S., Wuu, J. & Turner, D. A. 2004. MRI-derived entorhinal volume is a good predictor of conversion from MCI to AD. *Neurobiology of Aging,* 25:9**,** 1197-1203.

Do Carmo, S. & Cuello, A. C. 2013. Modeling Alzheimer's disease in transgenic rats. *Molecular Neurodegeneration,* 8**,** 37.

Doehner, J., Madhusudan, A., Konietzko, U., Fritschy, J. M. & Knuesel, I. 2010. Co-localization of Reelin and proteolytic AbetaPP fragments in hippocampal plaques in aged wild-type mice. *Journal of Alzheimer's Disease,* 19:4**,** 1339-57.

Dong, H. W., Swanson, L. W., Chen, L., Fanselow, M. S. & Toga, A. W. 2009. Genomic-anatomic evidence for distinct functional domains in hippocampal field CA1. *Proceedings of the National Academy of Sciences of the United States of America,* 106:28**,** 11794-9.

Duffy, A. M., Morales-Corraliza, J., Bermudez-Hernandez, K. M., Schaner, M. J., Magagna-Poveda, A., Mathews, P. M. & Scharfman, H. E. 2015. Entorhinal cortical defects in Tg2576 mice are present as early as 2-4 months of age. *Neurobiology of Aging,* 36:1**,** 134-48.

Durakoglugil, M. S., Chen, Y., White, C. L., Kavalali, E. T. & Herz, J. 2009. Reelin signaling antagonizes beta-amyloid at the synapse. *Proceedings of the National Academy of Sciences of the United States of America,* 106:37**,** 15938-43.

Duyckaerts, C., Delatour, B. & Potier, M. C. 2009. Classification and basic pathology of Alzheimer disease. *Acta Neuropathologica,* 118:1**,** 5-36.

Fanselow, M. S. & Dong, H. W. 2010. Are the dorsal and ventral hippocampus functionally distinct structures? *Neuron,* 65:1**,** 7-19.

Ferri, C. P., Prince, M., Brayne, C., Brodaty, H., Fratiglioni, L., Ganguli, M., Hall, K., Hasegawa, K., Hendrie, H., Huang, Y., Jorm, A., Mathers, C., Menezes, P. R., Rimmer, E., Scazufca, M. & Alzheimer's Disease, I. 2005. Global prevalence of dementia: a Delphi consensus study. *Lancet,* 366:9503**,** 2112-7.

Flood, D. G., Lin, Y. G., Lang, D. M., Trusko, S. P., Hirsch, J. D., Savage, M. J., Scott, R. W. & Howland, D. S. 2009. A transgenic rat model of Alzheimer's disease with extracellular Abeta deposition. *Neurobiology of Aging,* 30:7**,** 1078-90.

Forstl, H. & Kurz, A. 1999. Clinical features of Alzheimer's disease. *European Archives of Psychiatry and Clinical Neuroscience,* 249:6**,** 288-90.

Freund, T. F. & Buzsaki, G. 1996. Interneurons of the hippocampus. *Hippocampus,* 6:4**,** 347-470.

Galeano, P., Martino Adami, P. V., Do Carmo, S., Blanco, E., Rotondaro, C., Capani, F., Castano, E. M., Cuello, A. C. & Morelli, L. 2014. Longitudinal analysis of the behavioral phenotype in a novel transgenic rat model of early stages of Alzheimer's disease. *Frontiers in Behavioral Neuroscience,* 8**,** 321.

Gatome, C. W., Slomianka, L., Lipp, H. P. & Amrein, I. 2010. Number estimates of neuronal phenotypes in layer II of the medial entorhinal cortex of rat and mouse. *Neuroscience,* 170:1**,** 156-65.

George, S., Ronnback, A., Gouras, G. K., Petit, G. H., Grueninger, F., Winblad, B., Graff, C. & Brundin, P. 2014. Lesion of the subiculum reduces the spread of amyloid beta pathology to interconnected brain regions in a mouse model of Alzheimer's disease. *Acta Neuropathologica Communications,* 2**,** 17.

Gianatti, M. 2015. *Projections of calbindin expressing neurons in layer II of the entorhinal cortex.* MSc in Neuroscience Master Thesis, Norwegian University of Science and Technology (NTNU).

Giannakopoulos, P., Herrmann, F. R., Bussiere, T., Bouras, C., Kovari, E., Perl, D. P., Morrison, J. H., Gold, G. & Hof, P. R. 2003. Tangle and neuron numbers, but not amyloid load, predict cognitive status in Alzheimer's disease. *Neurology,* 60:9**,** 1495-500.

Gomez-Isla, T., Price, J. L., Mckeel, D. W., Jr., Morris, J. C., Growdon, J. H. & Hyman, B. T. 1996. Profound loss of layer II entorhinal cortex neurons occurs in very mild Alzheimer's disease. *Journal of Neuroscience,* 16:14**,** 4491-500.

Gouras, G. K., Almeida, C. G. & Takahashi, R. H. 2005. Intraneuronal Abeta accumulation and origin of plaques in Alzheimer's disease. *Neurobiology of Aging,* 26:9**,** 1235-44.

Gouras, G. K., Tampellini, D., Takahashi, R. H. & Capetillo-Zarate, E. 2010. Intraneuronal beta-amyloid accumulation and synapse pathology in Alzheimer's disease. *Acta neuropathologica,* 119:5**,** 523-41.

Gouras, G. K., Tsai, J., Naslund, J., Vincent, B., Edgar, M., Checler, F., Greenfield, J. P., Haroutunian, V., Buxbaum, J. D., Xu, H., Greengard, P. & Relkin, N. R. 2000. Intraneuronal Abeta42 accumulation in human brain. *The American Journal of Pathology,* 156:1**,** 15-20.

Graeber, M. B. & Mehraein, P. 1999. Reanalysis of the first case of Alzheimer's disease. *European Archives of Psychiatry and Clinical Neuroscience,* 249 Suppl 3**,** 10-3.

Grand, J. & Feldman, H. H. 2007. Historical concepts of Alzheimer's disease and dementia. *In:* Feldman, H. H. (ed.) *Atlas of Alzheimer's disease.* London, UK: Informa Healthcare.

Gundersen, H. J. 1986. Stereology of arbitrary particles. A review of unbiased number and size estimators and the presentation of some new ones, in memory of William R. Thompson. *Journal of Microscopy,* 143:1**,** 3-45.

Gundersen, H. J., Jensen, E. B., Kieu, K. & Nielsen, J. 1999. The efficiency of systematic sampling in stereology--reconsidered. *Journal of Microscopy,* 193:3**,** 199-211.

Guo, Q., Christakos, S., Robinson, N. & Mattson, M. P. 1998. Calbindin D28k blocks the proapoptotic actions of mutant presenilin 1: reduced oxidative stress and preserved mitochondrial function. *Proceedings of the National Academy of Sciences of the United States of America,* 95:6**,** 3227-32.

Haass, C. & Selkoe, D. J. 2007. Soluble protein oligomers in neurodegeneration: lessons from the Alzheimer's amyloid beta-peptide. *Nature Reviews. Molecular Cell Biology,* 8:2**,** 101-12.

Hafting, T., Fyhn, M., Molden, S., Moser, M. B. & Moser, E. I. 2005. Microstructure of a spatial map in the entorhinal cortex. *Nature,* 436:7052**,** 801-6.

Hama, E. & Saido, T. C. 2005. Etiology of sporadic Alzheimer's disease: somatostatin, neprilysin, and amyloid beta peptide. *Medical Hypotheses,* 65:3**,** 498-500.

Hardy, J. A. & Higgins, G. A. 1992. Alzheimer's disease: the amyloid cascade hypothesis. *Science,* 256:5054**,** 184-5.

Harris, J. A., Devidze, N., Verret, L., Ho, K., Halabisky, B., Thwin, M. T., Kim, D., Hamto, P., Lo, I., Yu, G. Q., Palop, J. J., Masliah, E. & Mucke, L. 2010. Transsynaptic progression of amyloid-beta-induced neuronal dysfunction within the entorhinal-hippocampal network. *Neuron,* 68:3**,** 428-41.

Hazra, A., Gu, F., Aulakh, A., Berridge, C., Eriksen, J. L. & Ziburkus, J. 2013. Inhibitory neuron and hippocampal circuit dysfunction in an aged mouse model of Alzheimer's disease. *PloS one,* 8:5**,** e64318.

Heggland, I., Storkaas, I. S., Soligard, H. T., Kobro-Flatmoen, A. & Witter, M. P. 2015. Stereological estimation of neuron number and plaque load in the hippocampal region of a transgenic rat model of Alzheimer's disease. *The European Journal of Neuroscience,* 41:9**,** 1245-62.

Herring, A., Donath, A., Steiner, K. M., Widera, M. P., Hamzehian, S., Kanakis, D., Kolble, K., Elali, A., Hermann, D. M., Paulus, W. & Keyvani, K. 2012. Reelin depletion is an early phenomenon of Alzheimer's pathology. *Journal of Alzheimer's disease,* 30:4**,** 963-79.

Herz, J. & Beffert, U. 2000. Apolipoprotein E receptors: linking brain development and Alzheimer's disease. *Nature reviews. Neuroscience,* 1:1**,** 51-8.

Herz, J. & Chen, Y. 2006. Reelin, lipoprotein receptors and synaptic plasticity. *Nature reviews. Neuroscience,* 7:11**,** 850-9.

Hiesberger, T., Trommsdorff, M., Howell, B. W., Goffinet, A., Mumby, M. C., Cooper, J. A. & Herz, J. 1999. Direct binding of Reelin to VLDL receptor and ApoE receptor 2 induces tyrosine phosphorylation of disabled-1 and modulates tau phosphorylation. *Neuron,* 24:2**,** 481-9.

Hiltunen, M., Van Groen, T. & Jolkkonen, J. 2009. Functional roles of amyloid-beta protein precursor and amyloid-beta peptides: evidence from experimental studies. *Journal of Alzheimer's disease,* 18:2**,** 401-12.

Hoe, H. S., Lee, K. J., Carney, R. S., Lee, J., Markova, A., Lee, J. Y., Howell, B. W., Hyman, B. T., Pak, D. T., Bu, G. & Rebeck, G. W. 2009. Interaction of reelin with amyloid precursor protein promotes neurite outgrowth. *Journal of Neuroscience,* 29:23**,** 7459-73.

Hof, P. R. & Morrison, J. H. 1991. Neocortical neuronal subpopulations labeled by a monoclonal antibody to calbindin exhibit differential vulnerability in Alzheimer's disease. *Experimental Neurology,* 111:3**,** 293-301.

Hof, P. R., Nimchinsky, E. A., Celio, M. R., Bouras, C. & Morrison, J. H. 1993. Calretinin-immunoreactive neocortical interneurons are unaffected in Alzheimer's disease. *Neuroscience Letters,* 152:1-2**,** 145-8.

Hsieh, H., Boehm, J., Sato, C., Iwatsubo, T., Tomita, T., Sisodia, S. & Malinow, R. 2006. AMPAR removal underlies Abeta-induced synaptic depression and dendritic spine loss. *Neuron,* 52:5**,** 831-43.

Hu, H., Gan, J. & Jonas, P. 2014. Interneurons. Fast-spiking, parvalbumin(+) GABAergic interneurons: from cellular design to microcircuit function. *Science,* 345:6196**,** 1255263.

Hughes, K. R. 1965. Dorsal and ventral hippocampus lesions and maze learning: influence of preoperative environment. *Canadian Journal of Psychology,* 19:4**,** 325-32.

Insausti, R., Herrero, M. T. & Witter, M. P. 1997. Entorhinal cortex of the rat: cytoarchitectonic subdivisions and the origin and distribution of cortical efferents. *Hippocampus,* 7:2**,** 146-83.

Iritani, S., Niizato, K. & Emson, P. C. 2001. Relationship of calbindin D28K-immunoreactive cells and neuropathological changes in the hippocampal formation of Alzheimer's disease. *Neuropathology: Official Journal of the Japanese Society of Neuropathology,* 21:3**,** 162-7.

Jarrett, J. T., Berger, E. P. & Lansbury, P. T., Jr. 1993. The C-terminus of the beta protein is critical in amyloidogenesis. *Annals of the New York Academy of Sciences,* 695**,** 144-8.

Jin, M., Shepardson, N., Yang, T., Chen, G., Walsh, D. & Selkoe, D. J. 2011. Soluble amyloid beta-protein dimers isolated from Alzheimer cortex directly induce Tau hyperphosphorylation and neuritic degeneration. *Proceedings of the National Academy of Sciences of the United States of America,* 108:14**,** 5819-24.

Jossin, Y., Ignatova, N., Hiesberger, T., Herz, J., Lambert De Rouvroit, C. & Goffinet, A. M. 2004. The central fragment of Reelin, generated by proteolytic processing in vivo, is critical to its function during cortical plate development. *Journal of Neuroscience,* 24:2**,** 514-21.

Juottonen, K., Laakso, M. P., Insausti, R., Lehtovirta, M., Pitkanen, A., Partanen, K. & Soininen, H. 1998. Volumes of the entorhinal and perirhinal cortices in Alzheimer's disease. *Neurobiology of Aging,* 19:1**,** 15-22.

Khan, U. A., Liu, L., Provenzano, F. A., Berman, D. E., Profaci, C. P., Sloan, R., Mayeux, R., Duff, K. E. & Small, S. A. 2014. Molecular drivers and cortical spread of lateral entorhinal cortex dysfunction in preclinical Alzheimer's disease. *Nature Neuroscience,* 17:2**,** 304-11.

Kjonigsen, L. J., Leergaard, T. B., Witter, M. P. & Bjaalie, J. G. 2011. Digital atlas of anatomical subdivisions and boundaries of the rat hippocampal region. *Frontiers in Neuroinformatics,* 5**,** 2.

Klein, W. L., Krafft, G. A. & Finch, C. E. 2001. Targeting small Abeta oligomers: the solution to an Alzheimer's disease conundrum? *Trends in Neurosciences,* 24:4**,** 219-24.

Klink, R. & Alonso, A. 1997. Morphological characteristics of layer II projection neurons in the rat medial entorhinal cortex. *Hippocampus,* 7:5**,** 571-83.

Kloosterman, F., Witter, M. P. & Van Haeften, T. 2003. Topographical and laminar organization of subicular projections to the parahippocampal region of the rat. *The Journal of Comparative Neurology,* 455:2**,** 156-71.

Knobloch, M., Konietzko, U., Krebs, D. C. & Nitsch, R. M. 2007. Intracellular Abeta and cognitive deficits precede beta-amyloid deposition in transgenic arcAbeta mice. *Neurobiology of Aging,* 28:9**,** 1297-306.

Knoferle, J., Yoon, S. Y., Walker, D., Leung, L., Gillespie, A. K., Tong, L. M., Bien-Ly, N. & Huang, Y. 2014. Apolipoprotein E4 produced in GABAergic interneurons causes learning and memory deficits in mice. *Journal of Neuroscience,* 34:42**,** 14069-78.

Knopp, A., Frahm, C., Fidzinski, P., Witte, O. W. & Behr, J. 2008. Loss of GABAergic neurons in the subiculum and its functional implications in temporal lobe epilepsy. *Brain: a Journal of Neurology,* 131:6**,** 1516-27.

Knuesel, I., Nyffeler, M., Mormede, C., Muhia, M., Meyer, U., Pietropaolo, S., Yee, B. K., Pryce, C. R., Laferla, F. M., Marighetto, A. & Feldon, J. 2009. Age-related accumulation of Reelin in amyloid-like deposits. *Neurobiology of Aging,* 30:5**,** 697-716.

Kocherhans, S., Madhusudan, A., Doehner, J., Breu, K. S., Nitsch, R. M., Fritschy, J. M. & Knuesel, I. 2010. Reduced Reelin expression accelerates amyloid-beta plaque formation and tau pathology in transgenic Alzheimer's disease mice. *Journal of Neuroscience,* 30:27**,** 9228-40.

Kook, S. Y., Jeong, H., Kang, M. J., Park, R., Shin, H. J., Han, S. H., Son, S. M., Song, H., Baik, S. H., Moon, M., Yi, E. C., Hwang, D. & Mook-Jung, I. 2014. Crucial role of calbindin-D28k in the pathogenesis of Alzheimer's disease mouse model. *Cell Death and Differentiation,* 21:10**,** 1575-87.

Kordower, J. H., Chu, Y. P., Stebbins, G. T., Dekosky, S. T., Cochran, E. J., Bennett, D. & Mufson, E. J. 2001. Loss and atrophy of layer II entorhinal cortex neurons in elderly people with mild cognitive impairment. *Annals of Neurology,* 49:2**,** 202-213.

Krantic, S., Isorce, N., Mechawar, N., Davoli, M. A., Vignault, E., Albuquerque, M., Chabot, J. G., Moyse, E., Chauvin, J. P., Aubert, I., Mclaurin, J. & Quirion, R. 2012. Hippocampal GABAergic neurons are susceptible to amyloid-beta toxicity in vitro and are decreased in number in the Alzheimer's disease TgCRND8 mouse model. *Journal of Alzheimer's disease,* 29:2**,** 293-308.

Laferla, F. M., Green, K. N. & Oddo, S. 2007. Intracellular amyloid-beta in Alzheimer's disease. *Nature Reviews. Neuroscience,* 8:7**,** 499-509.

Lambert De Rouvroit, C., De Bergeyck, V., Cortvrindt, C., Bar, I., Eeckhout, Y. & Goffinet, A. M. 1999. Reelin, the extracellular matrix protein deficient in reeler mutant mice, is processed by a metalloproteinase. *Experimental Neurology,* 156:1**,** 214-7.

Lambert, M. P., Barlow, A. K., Chromy, B. A., Edwards, C., Freed, R., Liosatos, M., Morgan, T. E., Rozovsky, I., Trommer, B., Viola, K. L., Wals, P., Zhang, C., Finch, C. E., Krafft, G. A. & Klein, W. L. 1998. Diffusible, nonfibrillar ligands derived from Abeta1-42 are potent central nervous system neurotoxins. *Proceedings of the National Academy of Sciences of the United States of America,* 95:11**,** 6448-53.

Lazarov, O., Lee, M., Peterson, D. A. & Sisodia, S. S. 2002. Evidence that synaptically released beta-amyloid accumulates as extracellular deposits in the hippocampus of transgenic mice. *Journal of Neuroscience,* 22:22**,** 9785-93.

Leon, W. C., Canneva, F., Partridge, V., Allard, S., Ferretti, M. T., Dewilde, A., Vercauteren, F., Atifeh, R., Ducatenzeiler, A., Klein, W., Szyf, M., Alhonen, L. & Cuello, A. C. 2010. A novel transgenic rat model with a full Alzheimer's-like amyloid pathology displays pre-plaque intracellular amyloid-beta-associated cognitive impairment. *Journal of Alzheimer's disease,* 20:1**,** 113-26.

Li, G., Bien-Ly, N., Andrews-Zwilling, Y., Xu, Q., Bernardo, A., Ring, K., Halabisky, B., Deng, C., Mahley, R. W. & Huang, Y. 2009a. GABAergic interneuron dysfunction impairs hippocampal neurogenesis in adult apolipoprotein E4 knockin mice. *Cell Stem Cell,* 5:6**,** 634-45.

Li, S., Hong, S., Shepardson, N. E., Walsh, D. M., Shankar, G. M. & Selkoe, D. 2009b. Soluble oligomers of amyloid Beta protein facilitate hippocampal long-term depression by disrupting neuronal glutamate uptake. *Neuron,* 62:6**,** 788-801.

Liao, M. Q., Tzeng, Y. J., Chang, L. Y., Huang, H. B., Lin, T. H., Chyan, C. L. & Chen, Y. C. 2007. The correlation between neurotoxicity, aggregative ability and secondary structure studied by sequence truncated Abeta peptides. *FEBS letters,* 581:6**,** 1161-5.

Liu, L., Drouet, V., Wu, J. W., Witter, M. P., Small, S. A., Clelland, C. & Duff, K. 2012. Trans-synaptic spread of tau pathology in vivo. *PloS one,* 7:2**,** e31302.

Livak, K. J. & Schmittgen, T. D. 2001. Analysis of relative gene expression data using real-time quantitative PCR and the 2(-Delta Delta C(T)) Method. *Methods,* 25:4**,** 402-8.

Loreth, D., Ozmen, L., Revel, F. G., Knoflach, F., Wetzel, P., Frotscher, M., Metzger, F. & Kretz, O. 2012. Selective degeneration of septal and hippocampal GABAergic neurons in a mouse model of amyloidosis and tauopathy. *Neurobiology of Disease,* 47:1**,** 1-12.

Mahley, R. W., Weisgraber, K. H. & Huang, Y. 2006. Apolipoprotein E4: a causative factor and therapeutic target in neuropathology, including Alzheimer's disease. *Proceedings of the National Academy of Sciences of the United States of America,* 103:15**,** 5644-51.

Mandelkow, E.-M. & Mandelkow, E. 2012. Biochemistry and Cell Biology of Tau Protein in Neurofibrillary Degeneration. *In:* Selkoe, D., Mandelkow, E. & Holtzman, D. M. (eds.) *The Biology of Alzheimer's Disease*. New York, NY, USA: Cold Spring Harbor Laboratory Press.

Mann, E. O. & Paulsen, O. 2007. Role of GABAergic inhibition in hippocampal network oscillations. *Trends in Neurosciences,* 30:7**,** 343-9.

Maren, S. 1999. Neurotoxic or electrolytic lesions of the ventral subiculum produce deficits in the acquisition and expression of Pavlovian fear conditioning in rats. *Behavioral Neuroscience,* 113:2**,** 283-90.

Maurer, K., Volk, S. & Gerbaldo, H. 1997. Auguste D and Alzheimer's disease. *Lancet,* 349:9064**,** 1546-9.

McGowan, E., Eriksen, J. & Hutton, M. 2006. A decade of modeling Alzheimer's disease in transgenic mice. *Trends in Genetics,* 22:5**,** 281-9.

Menendez De La Prida, L. 2003. Control of bursting by local inhibition in the rat subiculum in vitro. *The Journal of Physiology,* 549:1**,** 219-30.

Merrill, D. A., Chiba, A. A. & Tuszynski, M. H. 2001. Conservation of neuronal number and size in the entorhinal cortex of behaviorally characterized aged rats. *The Journal of Comparative Neurology,* 438:4**,** 445-56.

Mikkonen, M., Alafuzoff, I., Tapiola, T., Soininen, H. & Miettinen, R. 1999. Subfield- and layer-specific changes in parvalbumin, calretinin and calbindin-D28K immunoreactivity in the entorhinal cortex in Alzheimer's disease. *Neuroscience,* 92:2**,** 515-32.

Minkeviciene, R., Rheims, S., Dobszay, M. B., Zilberter, M., Hartikainen, J., Fulop, L., Penke, B., Zilberter, Y., Harkany, T., Pitkanen, A. & Tanila, H. 2009. Amyloid beta-induced neuronal hyperexcitability triggers progressive epilepsy. *Journal of Neuroscience,* 29:11**,** 3453-62.

Mochizuki, A., Tamaoka, A., Shimohata, A., Komatsuzaki, Y. & Shoji, S. 2000. Abeta42-positive non-pyramidal neurons around amyloid plaques in Alzheimer's disease. *Lancet,* 355:9197**,** 42-3.

Moon, M., Hong, H. S., Nam, D. W., Baik, S. H., Song, H., Kook, S. Y., Kim, Y. S., Lee, J. & Mook-Jung, I. 2012. Intracellular amyloid-beta accumulation in calcium-binding protein-deficient neurons leads to amyloid-beta plaque formation in animal model of Alzheimer's disease. *Journal of Alzheimer's disease,* 29:3**,** 615-28.

Moreno-Gonzalez, I., Baglietto-Vargas, D., Sanchez-Varo, R., Jimenez, S., Trujillo-Estrada, L., Sanchez-Mejias, E., Del Rio, J. C., Torres, M., Romero-Acebal, M., Ruano, D., Vizuete, M., Vitorica, J. & Gutierrez, A. 2009. Extracellular amyloid-beta and cytotoxic glial activation induce significant entorhinal neuron loss in young PS1(M146L)/APP(751SL) mice. *Journal of Alzheimer's disease,* 18:4**,** 755-76.

Moser, M. B. & Moser, E. I. 1998. Functional differentiation in the hippocampus. *Hippocampus,* 8:6**,** 608-19.

Moser, M. B., Moser, E. I., Forrest, E., Andersen, P. & Morris, R. G. 1995. Spatial learning with a minislab in the dorsal hippocampus. *Proceedings of the National Academy of Sciences of the United States of America,* 92:21**,** 9697-701.

Mucke, L. & Selkoe, D. 2012. Neurotoxicity of Amyloid beta-Protein: Synaptic and Network Dysfunction. *In:* Selkoe, D., Mandelkow, E. & Holtzman, D. M. (eds.) *The Biology of Alzheimer's Disease.* New York, NY, USA: Cold Spring Harbor Laboratory Press.

Mulders, W. H., West, M. J. & Slomianka, L. 1997. Neuron numbers in the presubiculum, parasubiculum, and entorhinal area of the rat. *The Journal of Comparative Neurology,* 385:1**,** 83-94.

Naber, P. A., Witter, M. P. & Lopes Silva, F. H. 2000. Networks of the hippocampal memory system of the rat. The pivotal role of the subiculum. *Annals of the New York Academy of Sciences,* 911**,** 392-403.

Nath, S., Agholme, L., Kurudenkandy, F. R., Granseth, B., Marcusson, J. & Hallbeck, M. 2012. Spreading of neurodegenerative pathology via neuron-to-neuron transmission of beta-amyloid. *Journal of Neuroscience,* 32:26**,** 8767-77.

Nilsen, L. H., Melo, T. M., Saether, O., Witter, M. P. & Sonnewald, U. 2012. Altered neurochemical profile in the McGill-R-Thy1-APP rat model of Alzheimer's disease: a longitudinal in vivo 1 H MRS study. *Journal of Neurochemistry,* 123:4**,** 532-41.

Nilsen, L. H., Melo, T. M., Witter, M. P. & Sonnewald, U. 2014. Early differences in dorsal hippocampal metabolite levels in males but not females in a transgenic rat model of Alzheimer's disease. *Neurochemical Research,* 39:2**,** 305-12.

Nixon, R. A. 2007. Autophagy, amyloidogenesis and Alzheimer disease. *Journal of cell science,* 120:23**,** 4081-91.

North, A. J. 2006. Seeing is believing? A beginners' guide to practical pitfalls in image acquisition. *The Journal of Cell Biology,* 172:1**,** 9-18.

O'Mara, S. 2005. The subiculum: what it does, what it might do, and what neuroanatomy has yet to tell us. *Journal of Anatomy,* 207:3**,** 271-82.

O'Mara, S. M., Sanchez-Vives, M. V., Brotons-Mas, J. R. & O'hare, E. 2009. Roles for the subiculum in spatial information processing, memory, motivation and the temporal control of behaviour. *Progress in Neuro-psychopharmacology & Biological Psychiatry,* 33:5**,** 782-90.

Oakley, H., Cole, S. L., Logan, S., Maus, E., Shao, P., Craft, J., Guillozet-Bongaarts, A., Ohno, M., Disterhoft, J., Van Eldik, L., Berry, R. & Vassar, R. 2006. Intraneuronal beta-amyloid aggregates, neurodegeneration, and neuron loss in transgenic mice with five familial Alzheimer's disease mutations: potential factors in amyloid plaque formation. *Journal of Neuroscience,* 26:40**,** 10129-40.

Oddo, S., Caccamo, A., Shepherd, J. D., Murphy, M. P., Golde, T. E., Kayed, R., Metherate, R., Mattson, M. P., Akbari, Y. & Laferla, F. M. 2003. Triple-transgenic model of Alzheimer's disease with plaques and tangles: intracellular Abeta and synaptic dysfunction. *Neuron,* 39:3**,** 409-21.

Onley, C. 2007. Antibodies for immunohistochemistry. *In:* Renshaw, S. (ed.) *Immunohistochemistry.* Bloxham, Oxfordshire, UK: Scion Publishing, Ltd.

Palop, J. J., Chin, J., Roberson, E. D., Wang, J., Thwin, M. T., Bien-Ly, N., Yoo, J., Ho, K. O., Yu, G. Q., Kreitzer, A., Finkbeiner, S., Noebels, J. L. & Mucke, L. 2007. Aberrant excitatory neuronal activity and compensatory remodeling of inhibitory hippocampal circuits in mouse models of Alzheimer's disease. *Neuron,* 55:5**,** 697-711.

Palop, J. J., Jones, B., Kekonius, L., Chin, J., Yu, G. Q., Raber, J., Masliah, E. & Mucke, L. 2003. Neuronal depletion of calcium-dependent proteins in the dentate gyrus is tightly linked to Alzheimer's disease-related cognitive deficits. *Proceedings of the National Academy of Sciences of the United States of America,* 100:16**,** 9572-7.

Palop, J. J. & Mucke, L. 2009. Epilepsy and cognitive impairments in Alzheimer disease. *Archives of Neurology,* 66:4**,** 435-40.

Palop, J. J. & Mucke, L. 2010. Amyloid-beta-induced neuronal dysfunction in Alzheimer's disease: from synapses toward neural networks. *Nature Neuroscience,* 13:7**,** 812-8.

Panuccio, G., Vicini, S. & Avoli, M. 2012. Cell type-specific properties of subicular GABAergic currents shape hippocampal output firing mode. *PloS one,* 7:12**,** e50241.

Pennanen, C., Kivipelto, M., Tuomainen, S., Hartikainen, P., Hanninen, T., Laakso, M. P., Hallikainen, M., Vanhanen, M., Nissinen, A., Helkala, E. L., Vainio, P., Vanninen, R., Partanen, K. & Soininen, H. 2004. Hippocampus and entorhinal cortex in mild cognitive impairment and early AD. *Neurobiology of Aging,* 25:3**,** 303-10.

Pesold, C., Impagnatiello, F., Pisu, M. G., Uzunov, D. P., Costa, E., Guidotti, A. & Caruncho, H. J. 1998. Reelin is preferentially expressed in neurons synthesizing gamma-aminobutyric acid in cortex and hippocampus of adult rats. *Proceedings of the National Academy of Sciences of the United States of America,* 95:6**,** 3221-6.

Pike, C. J. & Cotman, C. W. 1993. Cultured GABA-immunoreactive neurons are resistant to toxicity induced by beta-amyloid. *Neuroscience,* 56:2**,** 269-74.

Ponomareva, N. V., Korovaitseva, G. I. & Rogaev, E. I. 2008. EEG alterations in non-demented individuals related to apolipoprotein E genotype and to risk of Alzheimer disease. *Neurobiology of Aging,* 29:6**,** 819-27.

Popovic, M., Caballero-Bleda, M., Kadish, I. & Van Groen, T. 2008. Subfield and layer-specific depletion in calbindin-D28K, calretinin and parvalbumin immunoreactivity in the dentate gyrus of amyloid precursor protein/presenilin 1 transgenic mice. *Neuroscience,* 155:1**,** 182-91.

Pujadas, L., Rossi, D., Andres, R., Teixeira, C. M., Serra-Vidal, B., Parcerisas, A., Maldonado, R., Giralt, E., Carulla, N. & Soriano, E. 2014. Reelin delays amyloid-beta fibril formation and rescues cognitive deficits in a model of Alzheimer's disease. *Nature Communications,* 5**,** 3443.

Qi, Y., Klyubin, I., Harney, S. C., Hu, N., Cullen, W. K., Grant, M. K., Steffen, J., Wilson, E. N., Do Carmo, S., Remy, S., Fuhrmann, M., Ashe, K. H., Cuello, A. C. & Rowan, M. J. 2014. Longitudinal testing of hippocampal plasticity reveals the onset and maintenance of endogenous human Ass-induced synaptic dysfunction in individual freely behaving pre-plaque transgenic rats: rapid reversal by anti-Ass agents. *Acta Neuropathologica Communications,* 2**,** 175.

Querfurth, H. W. & Laferla, F. M. 2010. Mechanisms of Disease Alzheimer's Disease. *New England Journal of Medicine,* 362:4**,** 329-344.

Ramos-Moreno, T., Galazo, M. J., Porrero, C., Martinez-Cerdeno, V. & Clasca, F. 2006. Extracellular matrix molecules and synaptic plasticity: immunomapping of intracellular and secreted Reelin in the adult rat brain. *The European Journal of Neuroscience,* 23**,** 401-22.

Ramos, B., Baglietto-Vargas, D., Del Rio, J. C., Moreno-Gonzalez, I., Santa-Maria, C., Jimenez, S., Caballero, C., Lopez-Tellez, J. F., Khan, Z. U., Ruano, D., Gutierrez, A. & Vitorica, J. 2006. Early neuropathology of somatostatin/NPY GABAergic cells in the hippocampus of a PS1xAPP transgenic model of Alzheimer's disease. *Neurobiology of Aging,* 27:2**,** 1658-72.

Rapp, P. R., Deroche, P. S., Mao, Y. & Burwell, R. D. 2002. Neuron number in the parahippocampal region is preserved in aged rats with spatial learning deficits. *Cerebral Cortex,* 12:11**,** 1171-9.

Ronnback, A., Sagelius, H., Bergstedt, K. D., Naslund, J., Westermark, G. T., Winblad, B. & Graff, C. 2012. Amyloid neuropathology in the single Arctic APP transgenic model affects interconnected brain regions. *Neurobiology of Aging,* 33:4**,** 831 e11-9.

Saez-Valero, J., Costell, M., Sjogren, M., Andreasen, N., Blennow, K. & Luque, J. M. 2003. Altered levels of cerebrospinal fluid reelin in frontotemporal dementia and Alzheimer's disease. *Journal of Neuroscience Research,* 72:1**,** 132-6.

Saiz-Sanchez, D., De La Rosa-Prieto, C., Ubeda-Banon, I. & Martinez-Marcos, A. 2014. Interneurons, tau and amyloid-beta in the piriform cortex in Alzheimer's disease. *Brain Structure & Function*.

Saiz-Sanchez, D., Ubeda-Banon, I., De La Rosa-Prieto, C., Argandona-Palacios, L., Garcia-Munozguren, S., Insausti, R. & Martinez-Marcos, A. 2010. Somatostatin, tau, and beta-amyloid within the anterior olfactory nucleus in Alzheimer disease. *Experimental Neurology,* 223:2**,** 347-50.

Saiz-Sanchez, D., Ubeda-Banon, I., De La Rosa-Prieto, C. & Martinez-Marcos, A. 2012. Differential expression of interneuron populations and correlation with amyloid-beta deposition in the olfactory cortex of an

AbetaPP/PS1 transgenic mouse model of Alzheimer's disease. *Journal of Alzheimer's disease,* 31:1**,** 113-29.

Sargolini, F., Fyhn, M., Hafting, T., Mcnaughton, B. L., Witter, M. P., Moser, M. B. & Moser, E. I. 2006. Conjunctive representation of position, direction, and velocity in entorhinal cortex. *Science,* 312:5774**,** 758-62.

Schmechel, D. E., Saunders, A. M., Strittmatter, W. J., Crain, B. J., Hulette, C. M., Joo, S. H., Pericak-Vance, M. A., Goldgaber, D. & Roses, A. D. 1993. Increased amyloid beta-peptide deposition in cerebral cortex as a consequence of apolipoprotein E genotype in late-onset Alzheimer disease. *Proceedings of the National Academy of Sciences of the United States of America,* 90:20**,** 9649-53.

Schwartz, S. P. & Coleman, P. D. 1981. Neurons of origin of the perforant path. *Experimental Neurology,* 74:1**,** 305-12.

Serrano-Pozo, A., Frosch, M. P., Masliah, E. & Hyman, B. 2012. Neuropathological Alterations in Alzheimer's Disease. *In:* Selkoe, D., Mandelkow, E. & Holtzman, D. M. (eds.) *The Biology of Alzheimer's Disease.* New York, NY, USA: Cold Spring Harbor Laboratory Press.

Siegelbaum, S. A. & Kandel, E. R. 2013. Prefrontal Cortex, Hippocampus, and the Biology of Explicit Memory Storage. *In:* Kandel, E. R., Schwartz, J. H., Jessell, T. M., Siegelbaum, S. A. & Hudspeth, A. J. (eds.) *Principles of Neural Science* 5ed. USA: McGraw-Hill Companies.

Snyder, E. M., Nong, Y., Almeida, C. G., Paul, S., Moran, T., Choi, E. Y., Nairn, A. C., Salter, M. W., Lombroso, P. J., Gouras, G. K. & Greengard, P. 2005. Regulation of NMDA receptor trafficking by amyloid-beta. *Nature Neuroscience,* 8:8**,** 1051-8.

Somogyi, P. 2010. Hippocampus: Intrinsic Organization. *In:* Shepherd, G. M. & Grillner, S. (eds.) *Handbook of Brain Microcircuits.* New York, New York, USA: Oxford University Press, Inc.

Somogyi, P. & Klausberger, T. 2005. Defined types of cortical interneurone structure space and spike timing in the hippocampus. *The Journal of Physiology,* 562:1**,** 9-26.

Stefanits, H., Wesseling, C. & Kovacs, G. G. 2014. Loss of Calbindin immunoreactivity in the dentate gyrus distinguishes Alzheimer's disease from other neurodegenerative dementias. *Neuroscience Letters,* 566**,** 137-41.

Stereology.Info. *Selecting the Area and Thickness Sub-Fractions* [Online]. Williston, VT, USA: MBF Bioscience, MicroBrightField Inc. Available: http://www.stereology.info/selecting-the-xy-fraction-of-the-section/ [Accessed 10.05.2015].

Takahashi, H., Brasnjevic, I., Rutten, B. P., Van Der Kolk, N., Perl, D. P., Bouras, C., Steinbusch, H. W., Schmitz, C., Hof, P. R. & Dickstein, D. L. 2010. Hippocampal interneuron loss in an APP/PS1 double mutant mouse and in Alzheimer's disease. *Brain Structure & Function,* 214:2-3**,** 145-60.

Tamamaki, N. & Nojyo, Y. 1993. Projection of the entorhinal layer II neurons in the rat as revealed by intracellular pressure-injection of neurobiotin. *Hippocampus,* 3:4**,** 471-80.

Tang, Q., Burgalossi, A., Ebbesen, C. L., Ray, S., Naumann, R., Schmidt, H., Spicher, D. & Brecht, M. 2014. Pyramidal and stellate cell specificity of grid and border representations in layer 2 of medial entorhinal cortex. *Neuron,* 84:6**,** 1191-7.

Tanzi, R. E. & Bertram, L. 2005. Twenty years of the Alzheimer's disease amyloid hypothesis: a genetic perspective. *Cell,* 120:4**,** 545-55.

Terry, R. D., Masliah, E., Salmon, D. P., Butters, N., Deteresa, R., Hill, R., Hansen, L. A. & Katzman, R. 1991. Physical basis of cognitive alterations in Alzheimer's disease: synapse loss is the major correlate of cognitive impairment. *Annals of Neurology,* 30:4**,** 572-80.

Tesson, L., Cozzi, J., Menoret, S., Remy, S., Usal, C., Fraichard, A. & Anegon, I. 2005. Transgenic modifications of the rat genome. *Transgenic Research,* 14:5**,** 531-46.

Thal, D. R., Rub, U., Orantes, M. & Braak, H. 2002. Phases of A beta-deposition in the human brain and its relevance for the development of AD. *Neurology,* 58:12**,** 1791-800.

Tomiyama, T., Matsuyama, S., Iso, H., Umeda, T., Takuma, H., Ohnishi, K., Ishibashi, K., Teraoka, R., Sakama, N., Yamashita, T., Nishitsuji, K., Ito, K., Shimada, H., Lambert, M. P., Klein, W. L. & Mori, H. 2010. A mouse model of amyloid beta oligomers: their contribution to synaptic alteration, abnormal tau phosphorylation, glial activation, and neuronal loss in vivo. *Journal of Neuroscience,* 30:14**,** 4845-56.

Tong, L. M., Djukic, B., Arnold, C., Gillespie, A. K., Yoon, S. Y., Wang, M. M., Zhang, O., Knoferle, J., Rubenstein, J. L., Alvarez-Buylla, A. & Huang, Y. 2014. Inhibitory interneuron progenitor transplantation restores

normal learning and memory in ApoE4 knock-in mice without or with Abeta accumulation. *Journal of Neuroscience,* 34:29**,** 9506-15.

Trujillo-Estrada, L., Davila, J. C., Sanchez-Mejias, E., Sanchez-Varo, R., Gomez-Arboledas, A., Vizuete, M., Vitorica, J. & Gutierrez, A. 2014. Early neuronal loss and axonal/presynaptic damage is associated with accelerated amyloid-beta accumulation in AbetaPP/PS1 Alzheimer's disease mice subiculum. *Journal of Alzheimer's disease,* 42:2**,** 521-41.

Van Strien, N. M., Cappaert, N. L. & Witter, M. P. 2009. The anatomy of memory: an interactive overview of the parahippocampal-hippocampal network. *Nature reviews. Neuroscience,* 10:4**,** 272-82.

Varga, C., Lee, S. Y. & Soltesz, I. 2010. Target-selective GABAergic control of entorhinal cortex output. *Nature Neuroscience,* 13:7**,** 822-4.

Verret, L., Mann, E. O., Hang, G. B., Barth, A. M., Cobos, I., Ho, K., Devidze, N., Masliah, E., Kreitzer, A. C., Mody, I., Mucke, L. & Palop, J. J. 2012. Inhibitory interneuron deficit links altered network activity and cognitive dysfunction in Alzheimer model. *Cell,* 149:3**,** 708-21.

Walsh, D. M., Klyubin, I., Fadeeva, J. V., Cullen, W. K., Anwyl, R., Wolfe, M. S., Rowan, M. J. & Selkoe, D. J. 2002. Naturally secreted oligomers of amyloid beta protein potently inhibit hippocampal long-term potentiation in vivo. *Nature,* 416:6880**,** 535-9.

Weeber, E. J., Beffert, U., Jones, C., Christian, J. M., Forster, E., Sweatt, J. D. & Herz, J. 2002. Reelin and ApoE receptors cooperate to enhance hippocampal synaptic plasticity and learning. *The Journal of Biological Chemistry,* 277:42**,** 39944-52.

Wei, W., Nguyen, L. N., Kessels, H. W., Hagiwara, H., Sisodia, S. & Malinow, R. 2010. Amyloid beta from axons and dendrites reduces local spine number and plasticity. *Nature Neuroscience,* 13:2**,** 190-6.

West, M. J., Kawas, C. H., Stewart, W. F., Rudow, G. L. & Troncoso, J. C. 2004. Hippocampal neurons in pre-clinical Alzheimer's disease. *Neurobiology of Aging,* 25:9**,** 1205-12.

West, M. J., Slomianka, L. & Gundersen, H. J. 1991. Unbiased stereological estimation of the total number of neurons in thesubdivisions of the rat hippocampus using the optical fractionator. *The Anatomical Record,* 231:4**,** 482-97.

Whishaw, I. Q., Metz, G. A., Kolb, B. & Pellis, S. M. 2001. Accelerated nervous system development contributes to behavioral efficiency in the laboratory mouse: a behavioral review and theoretical proposal. *Developmental Psychobiology,* 39:3**,** 151-70.

Wirths, O., Multhaup, G., Czech, C., Blanchard, V., Tremp, G., Pradier, L., Beyreuther, K. & Bayer, T. A. 2001. Reelin in plaques of beta-amyloid precursor protein and presenilin-1 double-transgenic mice. *Neuroscience Letters,* 316:3**,** 145-8.

Witter, M. P. 2010. Connectivity of the Hippocampus. *In:* Cutsuridis, V., Graham, B., Cobb, S. & Vida, I. (eds.) *Hippocampal Microcircuits.* New York, NY, USA: Springer.

World Health Organization. 2015. *Dementia, Fact sheet N°362* [Online]. Available: http://www.who.int/mediacentre/factsheets/fs362/en/ [Accessed 10.05.2015].

Wouterlood, F. G. 2002. Spotlight on the neurones (I): cell types, local connectivity, microcircuits, and distribution of markers. *In:* Witter, M. P. & Wouterlood, F. G. (eds.) *The Parahippocampal Region: Organization and Role in Cognitive Function.* New York, NY, USA: Oxford University Press.

Yankner, B. A., Duffy, L. K. & Kirschner, D. A. 1990. Neurotrophic and neurotoxic effects of amyloid beta protein: reversal by tachykinin neuropeptides. *Science,* 250:4978**,** 279-82.

Yankner, B. A. & Lu, T. 2009. Amyloid beta-protein toxicity and the pathogenesis of Alzheimer disease. *The Journal of Biological Chemistry,* 284:8**,** 4755-9.

Youmans, K. L., Tai, L. M., Kanekiyo, T., Stine, W. B., Jr., Michon, S. C., Nwabuisi-Heath, E., Manelli, A. M., Fu, Y., Riordan, S., Eimer, W. A., Binder, L., Bu, G., Yu, C., Hartley, D. M. & Ladu, M. J. 2012. Intraneuronal Abeta detection in 5xFAD mice by a new Abeta-specific antibody. *Molecular Neurodegeneration,* 7**,** 8.

Zahorsky-Reeves, J., Lawson, G., Chu, D. K., Schimmel, A., Ezell, P. C., Dang, M. & Couto, M. 2007. Maintaining longevity in a triple transgenic rat model of Alzheimer's disease. *Journal of the American Association for Laboratory Animals,* 46:4**,** 124-124.

APPENDIX A – LIST OF ANTIBODIES, SERUMS, AND CHEMICALS

Antibodies

Primary antibodies

Antibody	**Manufacturer**	**Type**
Goat anti-somatostatin	Santa Cruz Biotechnology, Inc., Dallas, TX, USA	Polyclonal IgG
McSA1 (mouse anti-Aβ)	MédiMabs, Montreal, Canada	Monoclonal IgG1
MOAB-2 (mouse anti-Aβ)	Biosensis, Thebarton, SA, Australia	Monoclonal IgG2b
Mouse anti-GAD67	Merck Millipore, Merck kGaA, Darmstadt, Germany	Monoclonal IgG2a
Mouse anti-reelin	Merck Millipore, Merck kGaA, Darmstadt, Germany	Monoclonal IgG1
Rabbit anti-calbindin		Polyclonal IgG
Rabbit anti-parvalbumin	Swant, Marly, Switzerland	Polyclonal IgG
Rabbit anti-reelin	Biorbyt, Cambridge, UK	Polyclonal IgG

Secondary antibodies

Antibody	**Manufacturer**
Donkey anti-goat IgG	Sigma-Aldrich, St. Louis, MO, USA
Goat anti-mouse IgG biotin	Sigma-Aldrich, St. Louis, MO, USA
Goat anti-mouse IgG A488	Invitrogen, ThermoFisher Scientific, Waltham, MA, USA
Goat anti mouse IgG A546	Invitrogen, ThermoFisher Scientific, Waltham, MA, USA
Goat anti-mouse IgG1 A555	Invitrogen, ThermoFisher Scientific, Waltham, MA, USA
Goat anti-mouse IgG2a A647	Invitrogen, ThermoFisher Scientific, Waltham, MA, USA

Goat anti-rabbit IgG A488	Invitrogen, ThermoFisher Scientific, Waltham, MA, USA
Goat anti-rabbit IgG A546	Invitrogen, ThermoFisher Scientific, Waltham, MA, USA

Third antibodies

Antibody	**Manufacturer**
Avidin-biotin complex (ABC)	Vectastain ABC kit, Vector Laboratories, Burlingame, CA, USA

Serums

Serum	**Manufacturer**
Normal donkey serum	Sigma-Aldrich, St. Louis, MO, USA
Normal goat serum	Abcam, Cambridge, UK

Chemicals

Chemical	**Manufacturer**
Citric acid	Merck-Schuchardt, Hohenbrunn, Germany
3,3'-diaminobenzidine (DAB)	Sigma-Aldrich, St. Louis, MO, USA
Dimethyl sulfoxide (DMSO)	VWR International, Radnor, PA, USA
Entellan	Merck kGaA, Darmstadt, Germany
Formic acid	VWR International, Radnor, PA, USA
Gelatine	Oxoid Ltd., Basingstoke, UK
H_2O_2	Sigma-Aldrich, St. Louis, MO, USA
HCl	Merck kGaA, Darmstadt, Germany

KCl	Merck kGaA, Darmstadt, Germany
NaCl	VWR International, Radnor, PA, USA
$NaHCO_2$	Merck kGaA, Darmstadt, Germany
Paraformaldehyde (PFA)	Merck kGaA, Darmstadt, Germany
Phosphate buffer (PB)	Merck kGaA, Darmstadt, Germany
Sucrose	VWR International, Radnor, PA, USA
Tris(hydroxymethyl)aminomethane	Merck KGaA, Darmstadt, Germany
Triton X-100	Merck kGaA, Darmstadt, Germany
Toluene	VWR International, Radnor, PA, USA

PCR equipment

Equipment	**Manufacturer**
High Pure PCR Template Preparation Kit	Roche Diagnostics, Basel, Switzerland
RT^2 qPCR Primer Assays	Qiagen, Venlo, Netherlands
FastStart Universal SYBR Green Master	Roche Diagnostics, Basel, Switzerland

APPENDIX B – SOLUTIONS

Citrate buffer

10 mM citric acid, 0.05% Tween 20, pH 6.0

1.92 g citric acid (anhydrous)
1000 ml distilled water
Mix to dissolve. Adjust pH to 6.0 with 1N NaOH and then add 0.5 ml of Tween 20 and mix well. Store this solution at room temperature for 3 months or at 4 C for longer storage.

DMSO

100 ml

31.25 ml 400 mM phosphate buffer
46.75 ml H_2O
20 ml glycerine
2 ml DMSO

Phosphate buffer 400 mM pH 7.4

A: $NaH_2PO_4H_2O$ 27.6 g/500 ml H_2O
B: $Na_2HPO_4H_2O$ 35.6 g/500 ml H_2O

Make solutions A and B (start with B as it needs longer time). Add solution A to solution B until the pH is 7.4 (= 400 mM). Store in a dark place at room temperature for up to 1 month.

Phosphate buffer 125 mM pH 7.4

Dilute 400 mM phosphate buffer. Store in refrigerator for up to 1 week.

100 ml: 31.25 ml 400 mM phosphate buffer + 68.75 ml H_2O

500 ml: 156 mL 400 mM phosphate buffer + 344 mL H_2O

PFA 10%

Heat 200 ml of H_2O to 60°C in the microwave oven. Measure 20 g of paraformaldehyde and add the water. Add a few drops of NaOH and leave the solution on a hot stirrer until the solution is clear. Everything should be carefully carried out in a ventilated hood.

PFA 4%

200 ml 10% paraformaldehyde (see above)

156 ml 400 mM phosphate buffer

144 ml H_2O

Set the pH to 7.4 using HCl and filtrate. Make new fixative for every perfusion. Everything should be carefully carried out in a ventilated hood.

Ringer

0.85% NaCl	(4.25 g / 500 ml H_2O)
0.025% KCl	(0.125 g / 500 ml H_2O)
0.02% $NaHCO_3$	(0.1 g / 500 ml H_2O)

Filtrate. Heat to about 40°C before use. Set the pH to 6.9 using O_2.

Make fresh ringer before every perfusion.

Sucrose/saccharose

Dissolve 30 g sucrose in 31.25 ml 400 mM phosphate buffer and 68.75 ml H_2O (or in 100 ml 125 mM phosphate buffer).

TBS-TX buffer (0.5%) pH 8.0

Tris	3.03 g/500 ml H_2O
NaCl	4.48 g/500 ml H_2O
Triton X-100	2.5 ml/500 ml H_2O

Use HCl to adjust the pH. Store in refrigerator for up to one week.

Tris HCl

Tris	3.03 g/500 ml H_2O

Use HCl to adjust the pH to 7.6. Store in refrigerator for up to 1 week.

Tris HCl-gelatine

Heat Tris-HCl to 60°C in the microwave oven. Add 0.2 g gelatine per 100 ml Tris-HCl and put on stirrer until the gelatine has dissolved. Store in refrigerator for up to 1 week.

APPENDIX C – IMMUNOHISTOCHEMISTRY PROTOCOLS

For unsuccessful tested protocols for MOAB-2 and rabbit anti-reelin, see Appendix G.

General immunofluorescence protocol

1. HIER in 125 mM phosphate buffer (PB) at 60 ˚C for 2 hours if necessary
2. Wash sections 1 x 10 min in PB
3. Wash sections 3 x 10 min in PB with 0.5% Triton X-100 (PBT)
4. Incubate for 2 hours with 10% normal goat serum (NGS) in PBT
5. Incubate with primary antibody in PBT overnight on shaker at 4 ˚C
6. Wash sections 3 x 10 min in PBT
7. Incubate with secondary antibody in PBT for 2 hours on shaker in room temperature, protected from light
8. Wash sections 3 x 10 min in PB
9. Wash sections 2 x 5 min in Tris-HCl
10. Mount in Tris-HCl gelatine and dry overnight, protected from light
11. Coverslip in Toluene and Entellan and dry overnight

General peroxidase/DAB protocol

1. HIER in 125 mM 125 mM phosphate buffer (PB) at 60 ˚C for 2 hours if needed
2. Wash sections 2 x 10 min in PB
3. Wash sections 3 x 10 min in Tris-buffered saline with Triton X-100 (TBS-Tx)
4. Incubate for 30 min with 10% normal goat serum (NGS) in TBS-Tx
5. Draw off excess solution (do not wash)
6. Incubate with primary antibody in TBS-Tx overnight at 4 ˚C
7. Wash 3 x 10 min in TBS-Tx
8. Incubate with secondary antibody in TBS-Tx for 90 min in room temperature
9. Wash 3 x 10 min in TBS-Tx
10. Incubate with ABC for 90 min in room temperature
11. Wash 3 x 10 min in TBS-Tx

12. Wash 2 x 5 min in Tris-HCl
13. Incubate with DAB until the sections have the right colour
14. Wash 2 x 10 min in Tris-HCl
15. Mount in Tris-HCl gelatine and dry overnight
16. Coverslip in Toluene and Entellan and dry overnight

ABC:

From the ABC-kit, put 1 drop of solution A and 1 drop of solution B in 5 mL TBS-Tx. Mix well and leave on the bench for 30 min before use.

DAB:

Dissolve 1 tablet (10 mg) in 15 mL Tris-HCl by leaving it on a stirrer with heat (max 50˚C) for about 2 hours. Add 12 µL H_2O_2 just before use and filtrate.

Single immunohistochemistry protocols

McSA1

1. HIER in 125 mM phosphate buffer (PB) at 60 ˚C for 2 hours
2. Wash sections 1 x 10 min in PB
3. Wash sections 3 x 10 min in PB with 0.5% Triton X-100 (PBT)
4. Incubate for 2 hours with 10% normal goat serum (NGS) in PBT
5. Incubate with primary antibody, McSA1 from MédiMabs (1:1000), in PBT overnight on shaker at 4 ˚C
6. Wash sections 3 x 10 min in PBT
7. Incubate with secondary antibody, goat anti-mouse A546 (1:200), in PBT for 2 hours on shaker in room temperature, protected from light
8. Wash sections 3 x 10 min in PB
9. Wash sections 2 x 5 min in Tris-HCl
10. Mount in Tris-HCl gelatine and dry overnight, protected from light
11. Coverslip in Toluene and Entellan and dry overnight

Mouse anti-Reelin

1. HIER in 125 mM phosphate buffer (PB) at 60 ˚C for 2 hours
2. Wash sections 1 x 10 min in PB
3. Wash sections 3 x 10 min in PB with 0.5% Triton X-100 (PBT)
4. Incubate for 2 hours with 10% normal goat serum (NGS) in PBT
5. Incubate with primary antibody, mouse anti-Reelin from Merck Millipore (1:1000), in PBT overnight on shaker at 4 ˚C
6. Wash sections 3 x 10 min in PBT
7. Incubate with secondary antibody, goat anti-mouse A546 (1:200), in PBT for 2 hours on shaker in room temperature, protected from light
8. Wash sections 3 x 10 min in PB
9. Wash sections 2 x 5 min in Tris-HCl
10. Mount in Tris-HCl gelatine and dry overnight, protected from light
11. Coverslip in Toluene and Entellan and dry overnight

Double immunohistochemistry protocols

McSA1 and calbindin

1. HIER in 125 mM phosphate buffer (PB) at 60 ˚C for 2 hours
2. Wash sections 1 x 10 min in 125 mM phosphate PB
3. Wash sections 3 x 10 min in PB with 0.5% Triton X-100 (PBT)
4. Incubate for 2 hours with 10% normal goat serum (NGS) in PBT
5. Incubate with first primary antibody: rabbit anti-calbindin (Swant), 1:5000, in PBT for 48 hours on shaker at 4 ˚C
6. Wash sections 3 x 10 min in PBT
7. Incubate with first secondary antibody: goat anti-rabbit A546 (1:800), in PBT for 24 hours on shaker at 4 ˚C
8. Wash sections 3 x 10 min in PB
9. Wash sections 3 x 10 min in PBT
10. Incubate with second primary antibody: McSA1 (MédiMabs), 1:1000, in PBT for 24 hours on shaker at 4 ˚C

11. Wash sections 3 x 10 min in PBT
12. Incubate with second secondary antibody: goat anti-mouse A488 (1:200), in PBT for 2 hours on shaker in room temperature, protected from light
13. Wash sections 3 x 10 min in PB
14. Wash sections 2 x 5 min in Tris-HCl
15. Mount in Tris-HCl gelatine and dry overnight, protected from light
16. Coverslip in Toluene and Entellan and dry overnight

McSA1 and GAD67

1. HIER in 125 mM phosphate buffer (PB) at 60 ˚C for 2 hours
2. Wash sections 1 x 10 min in PB
3. Wash sections 3 x 10 min in PB with 0.5% Triton X-100-100 (PBT)
4. Incubate for 2 hours with 10% normal goat serum (NGS) in PBT
5. Incubate with primary antibodies, mouse anti-GAD67 from Merck Millipore (1:2000) and McSA1 from MédiMabs (1:1000), in PBT overnight on shaker at 4 ˚C
6. Wash sections 3 x 10 min in PBT
7. Incubate with secondary antibodies, goat anti-mouse IgG1 A555 (1:200) and goat anti-mouse IgG2a A647 (1:200), in PBT for 2 hours on shaker in room temperature, protected from light
8. Wash sections 3 x 10 min in PB
9. Wash sections 2 x 5 min in Tris-HCl
10. Mount in Tris-HCl gelatine and dry overnight, protected from light
11. Coverslip in Toluene and Entellan and dry overnight

McSA1 and reelin

1. HIER in 125 mM phosphate buffer (PB) at 60 ˚C for 3 hours
2. Wash sections 1 x 5 min in PB
3. Wash sections 3 x 10 min in PB with 0.5% Triton X-100 (PBT)
4. Incubate for 2 hours with 5% normal goat serum (NGS) in PBT
5. Incubate with primary antibodies, rabbit anti-reelin from Biorbyt (1:50) and McSA1 from MédiMabs (1:1000), in PBT with 5% NGS overnight (approximately 20 hours) on shaker at 4 ˚C
6. Wash sections 3 x 10 min in PBT

7. Incubate with secondary antibodies, goat anti-rabbit A488 (1:350) and goat anti-mouse A546 (1:350), in PBT with 5% NGS for 2 hours on shaker in room temperature, protected from light
8. Wash sections 3 x 10 min in PB
9. Wash sections 1 x 10 min in Tris-HCl
10. Mount in Tris-HCl gelatine and dry overnight, protected from light
11. Coverslip in Toluene and Entellan, and dry overnight

McSA1 and somatostatin

1. HIER in 125 mM phosphate buffer (PB) at 60 ˚C for 2 hours
2. Wash sections 1 x 10 min in 125 mM phosphate PB
3. Wash sections 3 x 10 min in PB with 0.5% Triton X-100 (PBT)
4. Incubate for 2 hours with 10% normal donkey serum in PBT
5. Incubate with first primary antibody: goat anti-somatostatin, 1:200, in PBT for 48 hours on shaker at 4 ˚C
6. Wash sections 3 x 10 min in PBT
7. Incubate with first secondary antibody: donkey anti-goat A546 (1:200), in PBT for 24 hours on shaker at 4 ˚C
8. Wash sections 3 x 10 min in PB
9. Wash sections 3 x 10 min in PBT
10. Incubate for 2 hours with 10% normal goat serum (NGS) in PBT
11. Incubate with second primary antibody: McSA1 (MédiMabs), 1:1000, in PBT for 24 hours on shaker at 4 ˚C
12. Wash sections 3 x 10 min in PBT
13. Incubate with second secondary antibody: goat anti-mouse A488 (1:200), in PBT for 2 hours on shaker in room temperature, protected from light
14. Wash sections 3 x 10 min in PB
15. Wash sections 2 x 5 min in Tris-HCl
16. Mount in Tris-HCl gelatine and dry overnight, protected from light
17. Coverslip in Toluene and Entellan and dry overnight

Rabbit anti-reelin and mouse anti-reelin

1. HIER in 125 mM phosphate buffer (PB) at 60 ˚C for 2 hours
2. Wash sections 1 x 10 min in PB
3. Wash sections 3 x 10 min in PB with 0.5% Triton X-100 (PBT)
4. Incubate for 2 hours with 10% normal goat serum (NGS) in PBT
5. Incubate with primary antibodies, mouse anti-reelin from Merck Millipore (1:1000) and rabbit anti-reelin from Biorbyt (1:150), in PBT overnight on shaker at 4 ˚C
6. Wash sections 3 x 10 min in PBT
7. Incubate with secondary antibodies, goat anti-mouse IgG A488 (1:400) and goat anti-rabbit IgG A546 (1:400), in PBT for 2 hours on shaker in room temperature, protected from light
8. Wash sections 3 x 10 min in PB
9. Wash sections 1 x 10 min in Tris-HCl
10. Mount in Tris-HCl gelatine and dry overnight, protected from light
11. Coverslip in Toluene and Entellan, and dry overnight

Reelin and calbindin

1. HIER in 125 mM phosphate buffer (PB) at 60 ˚C for 2 hours
2. Wash sections 1 x 10 min in 125 mM phosphate PB
3. Wash sections 3 x 10 min in PB with 0.5% Triton X-100 (PBT)
4. Incubate for 2 hours with 10% normal goat serum (NGS) in PBT
5. Incubate with first primary antibody: rabbit anti-calbindin (Swant), 1:5000, in PBT for 48 hours on shaker at 4 ˚C
6. Wash sections 3 x 10 min in PBT
7. Incubate with first secondary antibody: goat anti-rabbit A546 (1:800), in PBT for 24 hours on shaker at 4 ˚C
8. Wash sections 3 x 10 min in PB
9. Wash sections 3 x 10 min in PBT
10. Incubate with second primary antibody: mouse anti-reelin (Merck Millipore), 1:1000, in PBT for 24 hours on shaker at 4 ˚C
11. Wash sections 3 x 10 min in PBT
12. Incubate with second secondary antibody: goat anti-mouse A488 (1:200), in PBT for 2 hours on shaker in room temperature, protected from light

13. Wash sections 3 x 10 min in PB
14. Wash sections 2 x 5 min in Tris-HCl
15. Mount in Tris-HCl gelatine and dry overnight, protected from light
16. Coverslip in Toluene and Entellan and dry overnight

Triple immunohistochemistry protocols

McSA1, GAD67, and parvalbumin

1. HIER in 125 mM phosphate buffer (PB) at 60 ˚C for 2 hours
2. Wash sections 1 x 10 min in PB
3. Wash sections 3 x 10 min in PB with 0.5% Triton X-100 (PBT)
4. Incubate for 2 hours with 10% normal goat serum (NGS) in PBT
5. Incubate with primary antibodies:
   - McSA1 (1:1000)
   - Mouse anti-GAD67 (1:2000)
   - Rabbit anti-parvalbumin (1:1000)

   in PBT overnight on shaker at 4 ˚C
6. Wash sections 3 x 10 min in PBT
7. Incubate with secondary antibodies:
   - Goat anti-mouse IgG1 A555 (1:200)
   - Goat anti-mouse IgG2a A647 (1:200)
   - Goat anti-rabbit IgG A488 (1:200)

   in PBT for 2 hours on shaker in room temperature, protected from light
8. Wash sections 3 x 10 min in PB
9. Wash sections 2 x 5 min in Tris-HCl
10. Mount in Tris-HCl gelatine and dry overnight, protected from light
11. Coverslip in Toluene and Entellan and dry overnight

APPENDIX D – ANIMAL DETAILS

D.1. Rats used for reelin project

ID	Zygosity	Age	Sex
15231	+/+	6 months	Male
15234	+/+	6 months	Male
15238	+/+	6 months	Female
15301	+/+	6 months	Female
15305	+/+	6 months	Male
17015	+/+	3 months	Male
17016	+/+	3 months	Male
17017	+/+	3 months	Male
17018	+/+	3 months	Female
17019	+/+	3 months	Female
19872	+/+	P15	Male
19873	+/+	P15	Male
19874	+/+	P15	Male
19875	+/+	P15	Male
19876	+/+	P15	Male
19189	+/+	1 month (P41)	Male
19191	+/+	1 month (P41)	Male
20061	+/+	1 month	Male
20068	+/+	1 month	Female
20069	+/+	1 month	Female

D.2. Rats used for interneuron project

ID	Zygosity	Age	Sex	Comment
14212	+/+	18 months	Female	
15455	+/+	9 months	Female	
15717	+/+	6 months	Male	Subiculum counts
16118	-/-	6 months	Female	
16120	-/-	6 months	Female	
16804	+/+	6 months	Male	Subiculum counts
16908	+/+	6 months	Female	Subiculum counts
17019	+/+	3 months	Female	
17676	-/-	3 months	Male	
18462	-/-	1 month	Female	
18464	-/-	1 month	Male	
19601	+/+	6 months	Female	Subiculum counts
19873	+/+	P15	Male	
19874	+/+	P15	Male	
19942	+/+	3 months	Male	
20062	+/+	6 months	Male	Subiculum counts
20068	+/+	1 month	Female	Subiculum counts
20172	+/+	1 month	Female	Subiculum counts
20498	+/+	1 month	Female	Subiculum counts
20695	-/-	P15	Female	
20961	+/+	1 month	Male	Subiculum counts
20963	+/+	1 month	Male	Subiculum counts

D.3. Rats used for other experiments

ID	Zygosity	Age	Sex	Used for
13064	+/+	16 months	Male	MOAB-2 testing
14208	-/-	9 months	Male	MOAB-2 testing
15455	+/+	9 months	Female	Reelin double-staining
15717	+/+	6 months	Male	Mouse anti-reelin staining, reelin double-staining
16804	+/+	6 months	Male	McSA1/somatostatin double-staining, McSA1/calbindin double-staining, reelin/calbindin double-staining
16121	-/-	6 months	Female	Mouse anti-reelin staining, reelin/GAD67 double-staining
17015	+/+	3 months	Male	McSA1/GAD67/parvalbumin triple-staining
17016	+/+	3 months	Male	MOAB-2 testing
17017	+/+	3 months	Male	Reelin double-staining, McSA1/calbindin double-staining
17018	+/+	3 months	Female	MOAB-2 testing, reelin double-staining
19601	+/+	6 months	Female	Reelin/GAD67 double-staining
19875	+/+	P15	Male	Mouse anti-reelin staining
19601	+/+	6 months	Female	McSA1/calbindin double-staining
19942	+/+	3 months	Male	McSA1/calbindin double-staining
20061	+/+	1 month	Male	Reelin double-staining
20334	+/+	P6	Male	McSA1 staining
20498	-/-	1 month	Female	McSA1/calbindin double-staining
20694	-/-	P15	Female	Mouse anti-reelin staining

Table E.1. Details from the Optical Fractionator probe runs used to estimate the total number of cells double-positive for iAβ and reelin in LII of lateral and medial entorhinal cortex (LEC and MEC, respectively) of all animals in the P15 group.

Rat ID		Number of sections	Mean section thickness	Number of probes	Reelin+/ iAβ+	Estimated total reelin+/iAβ+	CE (m=1)	Reelin+/ iAβ-	Reelin-/ iAβ+	Comments
19872	LEC	11	14.7	173	77	24,409	0.11	2		
	MEC	6	14.1	160	112	53,257	0.10	4	1	
19873	LEC	12	15.5	118	71	32,334	0.12			
	MEC	6	14.6	118	85	47,808	0.11			1 left
19874	LEC	10	14.2	166	108	33,149	0.10	4		
	MEC	8	15.2	199	166	95,602	0.08	2		1 missing
19875	LEC	13	15.0	167	100	44,140	0.10	2		2 left
	MEC	6	15.3	149	112	65,728	0.10	1		2 left; 1 missing
19876	LEC	12	15.6	123	87	39,826	0.11	1		
	MEC	9	14.7	164	147	82,849	0.08			

Mean section thickness: number weighted mean section thickness (µm); Reelin+/iAβ+: number of counted cells double-positive for reelin and iAβ; CE: coefficient of error; Reelin+/iAβ-: number of counted cells positive for reelin and negative for iAβ.

Table E.2. Details from the Optical Fractionator probe runs used to estimate the total number of cells double-positive for iAβ and reelin in LII of lateral and medial entorhinal cortex (LEC and MEC, respectively) of all animals in the one month group.

Rat ID		Number of sections	Mean section thickenss	Number of probes	Reelin+/ iAβ+	Estimated total reelin+/ iAβ+	CE (m=1)	Reelin+/ iAβ-	Reelin-/ iAβ+	Comments
19189	LEC	11	15.5	162	85	38,615	0.11			1 left
	MEC	10	15.4	213	153	90,606	0.08			1 left
19191	LEC	14	14.7	188	128	55,438	0.09			
	MEC	12	14.7	257	219	123,615	0.07			
20061	LEC	10	15.7	203	127	42,940	0.09			
	MEC	12	16.1	302	212	115,087	0.07			
20068	LEC	10	15.7	144	114	38,688	0.09			
	MEC	7	15.4	304	217	112,434	0.07			
20069	LEC	12	13.9	192	133	39,912	0.09			
	MEC	10	15.4	270	222	115,669	0.07			

Mean section thickness: number weighted mean section thickness (µm); Reelin+/iAβ+: number of counted cells double-positive for reelin and iAβ; CE: coefficient of error; Reelin+/iAβ-: number of counted cells positive for reelin and negative for iAβ.

Table E.3. Details from the Optical Fractionator probe runs used to estimate the total number of cells double-positive for iAβ and reelin in LII of lateral and medial entorhinal cortex (LEC and MEC, respectively) of all animals in the three month group.

Rat ID		Number of sections	Mean section thickness	Number of probes	Reelin+/ iAβ+	Estimated total reelin+/ iAβ+	CE (m=1)	Reelin+/ iAβ-	Reelin-/ iAβ+	Comments
17015	LEC	16	15.3	244	173	77,567	0.08			
	MEC	10	15.3	212	174	101,925	0.08			
17016	LEC	13	15.3	163	117	52,600	0.09			
	MEC	9	14.4	275	241	132,992	0.07			
17017	LEC	10	15.7	97	74	34,184	0.12			
	MEC	6	14.9	186	148	84,895	0.09		2	
17018	LEC	14	14.3	148	90	37,815	0.11			
	MEC	9	15.4	242	214	126,230	0.07			
17019	LEC	17	13.8	189	136	55,036	0.09		1	
	MEC	11	13.2	243	219	110,926	0.07			

Mean section thickness: number weighted mean section thickness (μm); Reelin+/iAβ+: number of counted cells double-positive for reelin and iAβ; CE: coefficient of error; Reelin+/iAβ-: number of counted cells positive for reelin and negative for iAβ.

Table E.4. Details from the Optical Fractionator probe runs used to estimate the total number of cells double-positive for iAβ and reelin in LII of lateral and medial entorhinal cortex (LEC and MEC, respectively) of all animals in the six month group.

Rat ID		Number of sections	Mean section thickness	Number of probes	Reelin+/ iAβ+	Estimated total reelin+/ iAβ+	CE (m=1)	Reelin+/ iAβ-	Reelin-/ iAβ+	Comments
15231	LEC	11	16.6	144	71	29,902	0.12			
	MEC	7	15.9	321	249	133,396	0.07			
15234	LEC	15	14.7	188	113	48,834	0.09		1	
	MEC	10	16.2	337	234	145,249	0.07			
15238	LEC	14	16.4	205	124	43,793	0.09			
	MEC	7	16.1	283	214	116,189	0.07			
15301	LEC	19	12.3	139	63	37,802	0.13	4	2	3 left
	MEC	10	12.8	252	184	114,908	0.07	4	1	
15305	LEC	12	16.9	201	116	42,292	0.09			1 left
	MEC	9	17.4	296	211	140,864	0.07			1 left

Mean section thickness: number weighted mean section thickness (μm); Reelin+/iAβ+: number of counted cells double-positive for reelin and iAβ; CE: coefficient of error; Reelin+/iAβ-: number of counted cells positive for reelin and negative for iAβ.

APPENDIX F – SUBICULUM COUNTS

Table F.1. Details about counts of iAβ-expression in interneurons in dorsal (DS), intermediate (IS), and ventral (VS) subiculum of each animal in the one month group.

Rat ID	Sex		DS	IS	VS
20068	Female	GAD67+/iAβ+	326	60	68
		GAD67+/iAβ-	588	117	269
		Total GAD67+	914	177	337
		Number of sections	13	2	6
20172	Female	GAD67+/iAβ+	223	52	93
		GAD67+/iAβ-	504	203	400
		Total GAD67+	727	255	493
		Number of sections	13	2	8
20498	Female	GAD67+/iAβ+	277	77	94
		GAD67+/iAβ-	307	73	209
		Total GAD67+	584	150	303
		Number of sections	11	2	6
20961	Male	GAD67+/iAβ+	167	70	96
		GAD67+/iAβ-	320	188	304
		GAD67+	487	258	400
		Number of sections	10	2	7
20963	Male	GAD67+/iAβ+	195	76	92
		GAD67+/iAβ-	397	107	395
		Total GAD67+	592	183	487
		Number of sections	11	2	7

GAD67+/iAβ+: number of cells double-positive for GAD67 and iAβ; GAD67+/iAβ-: number of cells positive for GAD67 and negative for iAβ; Total GAD67+: total number of cells positive for GAD67.

Table F.2. Details about counts of iAβ-expression in interneurons in dorsal (DS), intermediate (IS), and ventral (VS) subiculum of each animal in the six month group.

Rat ID	Sex		DS	IS	VS
15717	Male	GAD67+	570	190	746
		GAD67+/iAβ+	177	56	129
		GAD67+/iAβ-	393	134	617
		Number of sections	15	3	10
16804	Male	GAD67+	451	148	338
		GAD67+/iAβ+	164	52	81
		GAD67+/iAβ-	287	96	257
		Number of sections	12	3	6
16908	Female	GAD67+	586	139	384
		GAD67+/iAβ+	200	32	69
		GAD67+/iAβ-	386	107	315
		Number of sections	12	2	6
19601	Female	GAD67+	487	172	432
		GAD67+/iAβ+	246	75	153
		GAD67+/iAβ-	241	97	279
		Number of sections	12	2	7
20062	Male	GAD67+	445	151	317
		GAD67+/iAβ+	220	59	86
		GAD67+/iAβ-	225	92	231
		Number of sections	12	2	7

GAD67+/iAβ+: number of cells double-positive for GAD67 and iAβ; GAD67+/iAβ-: number of cells positive for GAD67 and negative for iAβ; Total GAD67+: total number of cells positive for GAD67.

APPENDIX G – TESTING OF ANTIBODIES

G.1. MOAB-2

G.1.1. Methods

MOAB-2 (Biosensis, Australia), a purified mouse monoclonal antibody to amyloid-β 40/42, was tested by immunohistochemical staining of tissue from two three month old homozygous (+/+) McGill-R-Thy1-APP rats (one male, one female). The antibody is reported to be specific for Aβ40 and Aβ42 and not detect APP or APP-CTFs in 5XFAD mice (Youmans et al., 2012). All variations except for four tests were carried out in parallel with tissue from two control animals: one homozygous 16 months old male and one nine months old wild-type (WT) male. Tissue was subjected to various pre-treatments and incubated with different concentrations of antibody (Table G.1). All IHC procedures were done according to the following general procedures.

General protocol, immunofluorescence (IF):

1. Pre-treatment (Table G.1)
2. Wash sections 1 x 10 minutes in 125 mM phosphate buffer (PB)
3. Wash sections 3 x 10 min in PB with 0.5% Triton X-100 (PBT)
4. Incubate for 2 hours with 10% normal goat serum (NGS) in PBT
5. Incubate with primary antibody, MOAB-2, overnight on shaker at 4 ˚C
6. Wash sections 3 x 10 minutes in PBT
7. Incubate with secondary antibody, Alexa fluorophore goat anti-mouse 488/546 (1:200), in PBT for 2 hours on shaker in room temperature, protected from light
8. Wash sections 3 x 10 minutes in PB
9. Wash sections 2 x 5 minutes in Tris-HCl
10. Mount in Tris-HCl gelatine and dry overnight, protected from light
11. Coverslip with Toluene and Entellan and dry overnight

General protocol, peroxidase/DAB:

1. Pre-treatment (Table G.1)
2. Wash sections 1 x 10 minutes in 125 mM phosphate buffer (PB)
3. Wash sections 3 x 10 minutes in PB with 0.5% Triton-X (PBT)
4. Incubate for 2 hours with 10% normal goat serum (NGS) in PBT

5. Incubate with primary antibody, MOAB-2 (1:500), overnight on shaker at 4 ˚C
6. Wash sections 3 x 10 minutes in PBT
7. Incubate with secondary antibody, biotinylated goat anti-mouse (1:200), in PBT for 2 hours on shaker in room temperature
8. Wash sections 3 x 10 minutes in PBT
9. Incubate with ABC 90 minutes in room temperature
10. Wash sections 3 x 10 minutes in PBT
11. Wash sections 2 x 5 minutes in Tris-HCl
12. Incubate with DAB for 30 minutes
13. Wash sections 2 x 5 minutes in Tris-HCl
14. Mount in Tris-HCl gelatine and dry overnight, protected from light
15. Coverslip with Toluene and Entellan and dry overnight

Table G.1. Tested pre-treatments and concentrations for MOAB-2 (mouse anti-amyloid β).

Pre-treatment	Rat ID	Method	Concentration	Controls
None	17016	IF	1:200	Yes
	17016	IF	1:500	Yes
	17016	IF	1:1000	Yes
	17018	DAB	1:500	Yes
PB 60 ˚C, 2 hours	17018	IF*	1:500	No
PB 60 ˚C, 3 hours	17016	IF	1:200	Yes
	17016	IF	1:500	Yes
	17016	IF	1:1000	Yes
	17018	DAB	1:500	Yes
CB 60 ˚C, 20 minutes	17016	IF	1:200	Yes
	17016	IF	1:500	Yes
	17016	IF	1:1000	Yes
	17018	IF*	1:500	No
CB 95 ˚C, 20 minutes	17018	DAB	1:500	Yes
CB 95 ˚C, 40 minutes	17018	DAB	1:500	Yes
FA 60 ˚C, 8 minutes	17018	IF*	1:500	No
FA 22 ˚C, 8 minutes	17018	IF*	1:500	No

CB = citrate buffer; DAB = 3,3'-diaminobenzidine; FA = formic acid; IF = immunofluorescence; PB = 125 mM phosphate buffer; * = tris-buffered saline (TBX; pH 8.0) instead of PB (pH 7.4) during washing and incubation.

G.1.2. Results

There was strong staining of amyloid plaques in the tissue from the 16 months old homozygous control rat with all variations tested (data not shown). No pre-treatment and heat-induced epitope retrieval (HIER) in 125 mM PB resulted in no staining in any of the sections from the homozygous rat with the DAB/peroxidase protocol (Figure G.1 A, C). Further, no staining was observed in the sections from the WT control (Figure G.1 B, D). HIER in citrate buffer (CB) at 95 ˚C for 20 minutes resulted in very weak, likely unspecific staining in all areas in tissue from the homozygous rat, with the strongest signal in layer II (LII) of lateral entorhinal cortex (LEC; Figure G.1 E). The same could be observed in the control tissue, but the cells were more strongly stained (Figure G.1 F). Increasing the incubation time to 40 minutes resulted in widespread staining, both in the sections from the homozygous rat (Figure G.1 G) and the negative control (Figure G.1 H), with stronger staining in the latter.

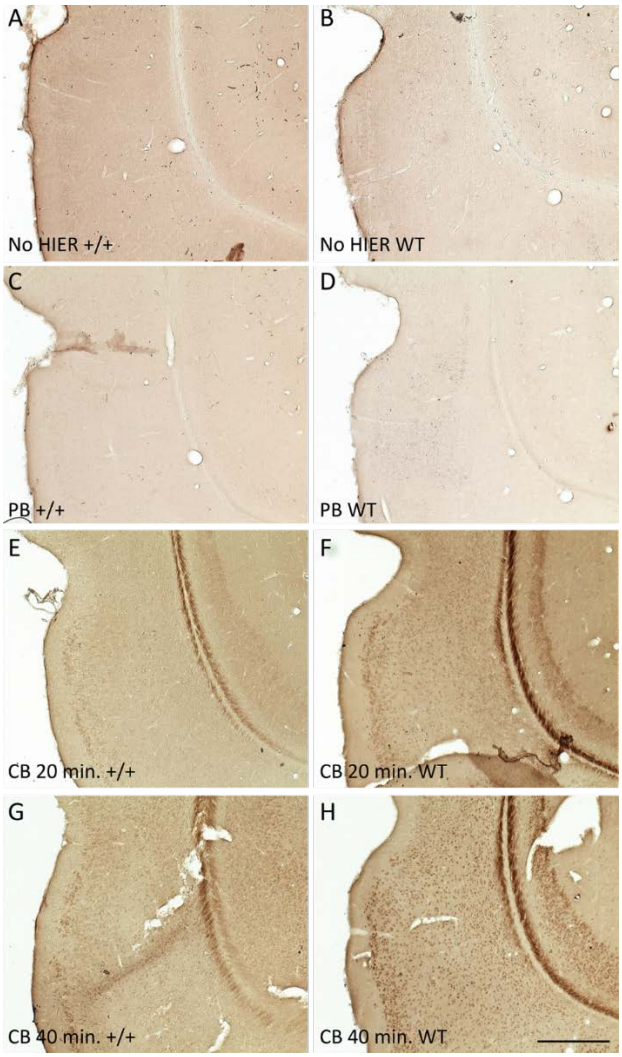

Figure G.1. Incubation with DAB with no pre-treatment and heat-induced epitope retrieval (HIER) in 125 mM phosphate buffer (PB) at 60 ˚C for three hours resulted in no iAβ-labelling with MOAB-2 in any areas. HIER in citrate buffer (CB) at 95 ˚C with subsequent staining with DAB resulted in weak, unspecific labelling in all areas in tissue from the homozygous rat, both with 20 and 40 minutes HIER. The labelling was stronger in the wild-type (WT) control with both 20 and 40 minutes HIER. A, B: No pre-treatment; C, D: Three hours HIER in 125 mM PB at 60 ˚C; E, F: HIER in CB at 95 ˚C for 20 minutes; G, H: HIER in CB at 95 ˚C for 40 minutes. A, C, E, G: Tissue from a three months old homozygous McGill-R-Thy-APP rat (ID: 17018); B, D, F, H: Tissue from a nine months old WT control rat (ID: 14208). Scale bar: 500 µm.

In general, fluorescent staining resulted in either no labelling, or weak, likely unspecific labelling in most of the tissue. Surprisingly, the signal was stronger and brighter in the WT control, where most cells appeared to be labelled when the tissue was pre-treated with heat.

No staining could be observed when the tissue was not subjected to any pre-treatments (Figure G.2 A, C, E). There was weak labelling in the negative control tissue at dilutions 1:500 (Figure G.3 D) and 1:1000 (Figure G.3 F), and stronger labelling at 1:200 (Figure G.2 B).

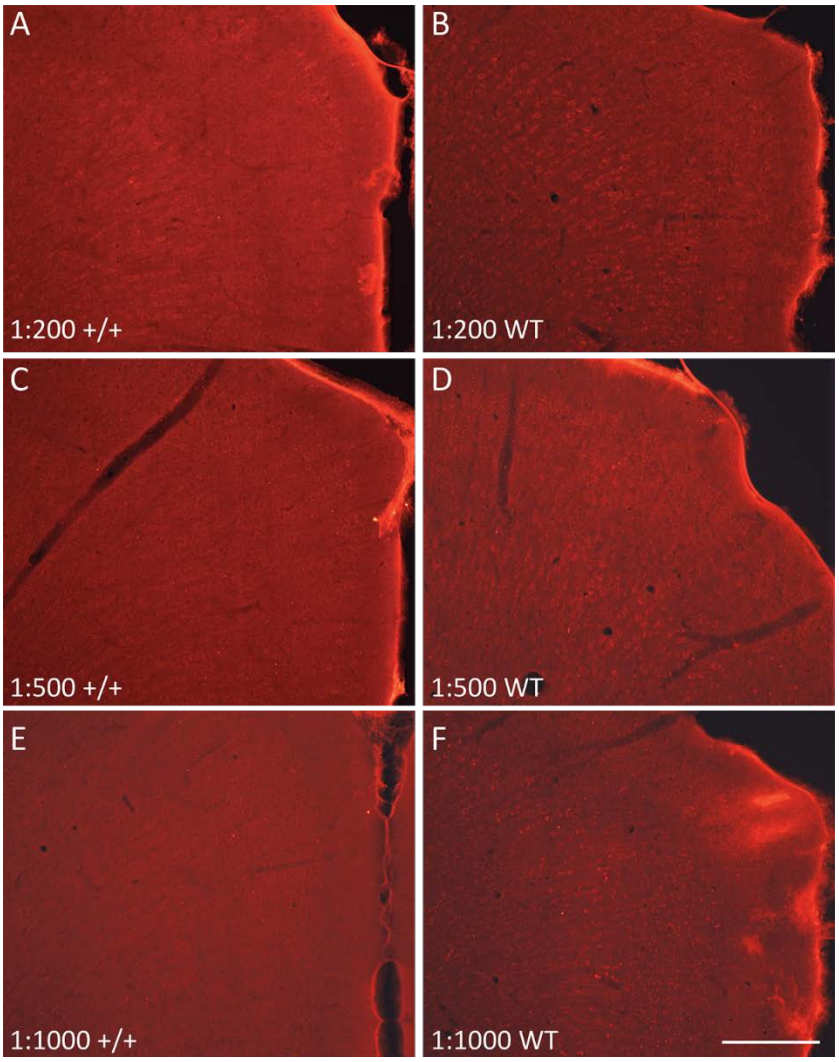

Figure G.2. No pre-treatment resulted in no staining of iAβ with MOAB-2 in the tissue from the homozygous McGill-R-Thy1-APP rat and weak, unspecific staining in tissue from the WT control, as shown for parts of retrosplenial cortex in all cases. A, C, E: Tissue from a three months old homozygous McGIll-R-Thy1-APP rat (ID: 17016); B, D, F: Tissue from a nine months old WT control rat (ID: 14208). A, B: 1:200, C, D: 1:500. E, F: 1:1000. Scale bar: 500 µm.

HIER at 60 ˚C for three hours in 125 mM PB resulted in no labelling in most areas in the homozygous positive rat, with perhaps weak labelling of cells in LII of LEC (Figure G.3 A, C, E). There was weak, unspecific labelling in the tissue from the WT control (Figure G.3 B, D, F).

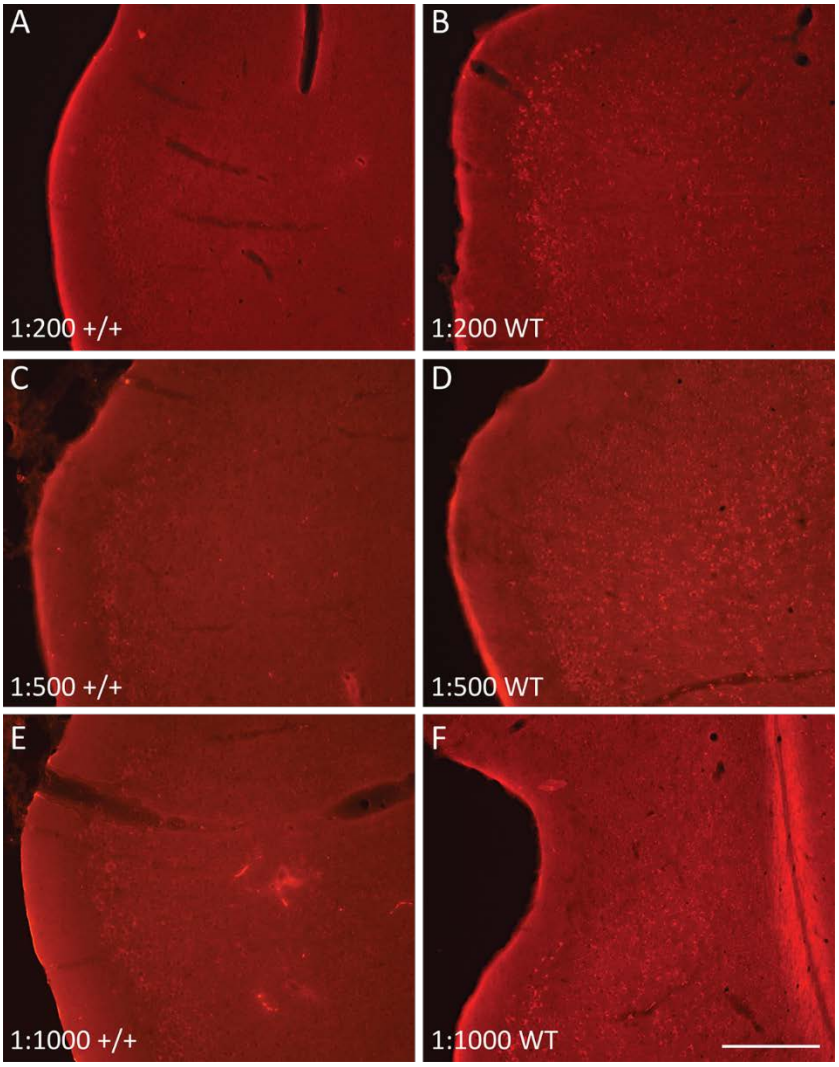

Figure G.3. HIER in 125 mM phosphate buffer at 60 ˚C for three hours resulted in little to no labelling of iAβ with MOAB-2 in sections from the homozygous McGill-R-Thy1-APP rat and weak, unspecific labelling in sections from the WT control, as shown for parts of lateral entorhinal cortex (A-C, E) and perirhinal cortex (D, F). A, C, E: Tissue from a three months old homozygous McGIII-R-Thy1-APP rat (ID: 17016); B, D, F: Tissue from a nine months old WT control rat (ID: 14208). A, B: 1:200, C, D: 1:500. E, F: 1:1000. Scale bar: 500 µm.

HIER at 60 ˚C in CB for 20 minutes resulted in similar staining as HIER in PB. The signal was weak in the sections from the homozygous positive animal using all three dilutions of the antibody, with perhaps some visible staining in LII of LEC (Figure G.4 A, C, E). Again, there was strong, unspecific labelling in the control tissue, with strongest signal in LEC LII (Figure G.4 B, D, F).

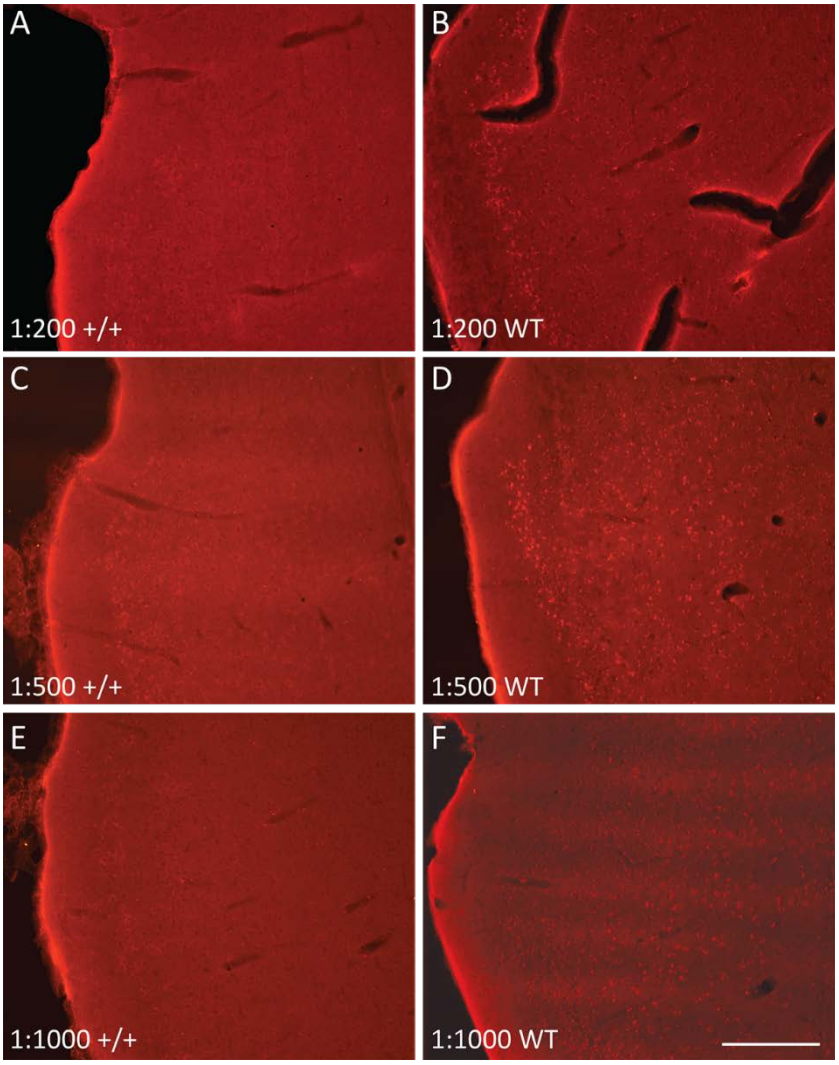

Figure G.4. HIER in citrate buffer at 60 ˚C for 20 minutes resulted in little to no iAβ-labelling with MOAB-2 in sections from the homozygous rat and unspecific labelling that was strongest in layer II of lateral entorhinal cortex in sections from the control, as shown for parts of lateral entorhinal cortex (A-E) and perirhinal cortex (F). A, C, E: Tissue from a three months old homozygous McGIII-R-Thy1-APP rat (ID: 17016); B, D, F: Tissue from a nine months old WT control rat (ID: 14208). A, B: 1:200, C, D: 1:500. E, F: 1:1000. Scale bar: 500 µm.

Pre-incubation with 88% formic acid (FA) for eight minutes in room temperature (Figure G.5 A) and at 60 ˚C (Figure G.5 B) resulted in wide-spread labelling of cells in all areas.

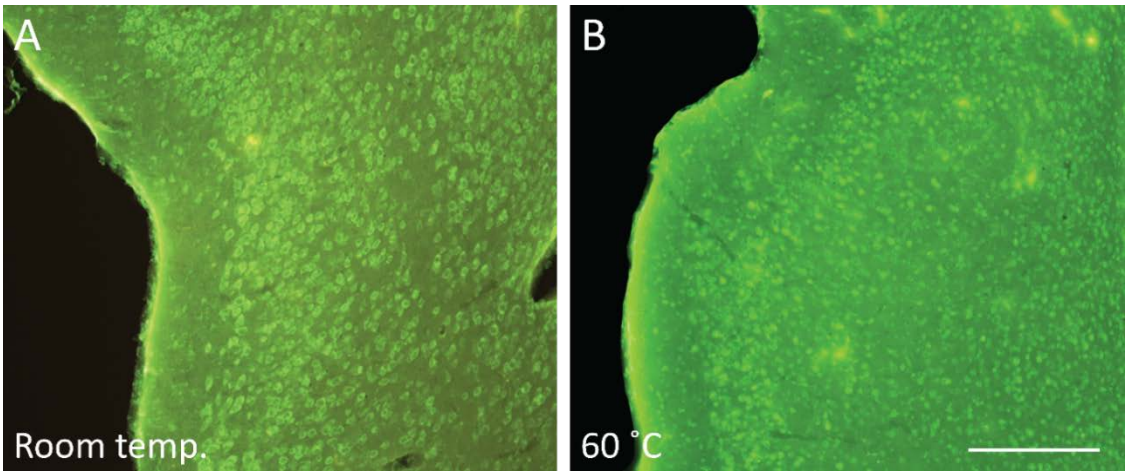

Figure G.5 (previous). Almost every cell was stained with MOAB-2 when the tissue was pre-incubated for eight minutes in 88% formic acid. A: incubation in room temperature; B: incubation at 60 ˚C. Areas shown are parts of lateral entorhinal and perirhinal cortices. Both sections are from a three months old homozygous McGill-R-Thy1-APP rat (ID: 17018) and the primary antibody was diluted 1:500. Scale bar: 500 µm.

G.2. Rabbit anti-reelin

G.2.1. Methods

As we obtained variable results with the rabbit anti-reelin antibody (Birobyt, Cambridge, UK), numerous tests were carried out in order to optimise the immunohistochemistry protocol. Most of the tests were done prior to this project and will not be shown here.

In all instances the tissue was co-incubated with rabbit anti-reelin and the G10 clone of mouse anti-reelin (Merck Millipore, Merck kGaA, Darmstadt, Germany) for comparison with this widely used antibody (not shown). The general double-immunohistochemistry protocol can be found in Appendix C.

For blocking variations, tissue from a one month old homozygous McGill-R-Thy1-APP rat was used. The protocol in Appendix C was followed from step 6. Steps 1-5 were as follows:

1. HIER in 125 mM phosphate buffer (PB) at 60 ˚C for 2 hours
2. Wash sections 1 x 5 min in PB
3. Wash sections 3 x 10 min in PB with 0.5% Triton X-100 (PBT)
4. a) Incubate for 2 hours with 10% normal goat serum (NGS) in PBT
   b) No blocking
5. Incubate with primary antibodies, mouse anti-reelin from Merck Millipore (1:1000) and rabbit anti-reelin from Biorbyt (1:150), overnight on shaker at 4 ˚C
   a) In PBT with 5% NGS with prior blocking (step 4)
   b) In PBT with prior blocking (step 4)
   c) In PBT without prior blocking (step 4)

For testing whether increasing the incubation time improved labelling, we followed the protocol in Appendix C but incubated with the primary antibodies for 48 hours instead of overnight. Both incubation in room temperature and in refrigerator (4 ˚C) was tested.

We also tested a new, purified version of the batch of antibody that was used for labelling the tissue used for stereology (batch lot # 1660). The tissue was from a three months old homozygous McGill-R-Thy1-APP rat and the protocol in Appendix C was used.

G.2.2. Results

There were no evident differences in labelling with blocking variations. Incubating the tissue in 5% NGS for two hours prior to incubating with the primary antibody resulted in weakly labelled cells in LII of EC and no visible labelling in other areas, both when the tissue was subsequently incubated with NGS along with the primary antibody (Figure G.6 A-B) and the primary antibody alone (Figure G.6 C-D). No blocking did not result in improved labelling (Figure G.5 E-F).

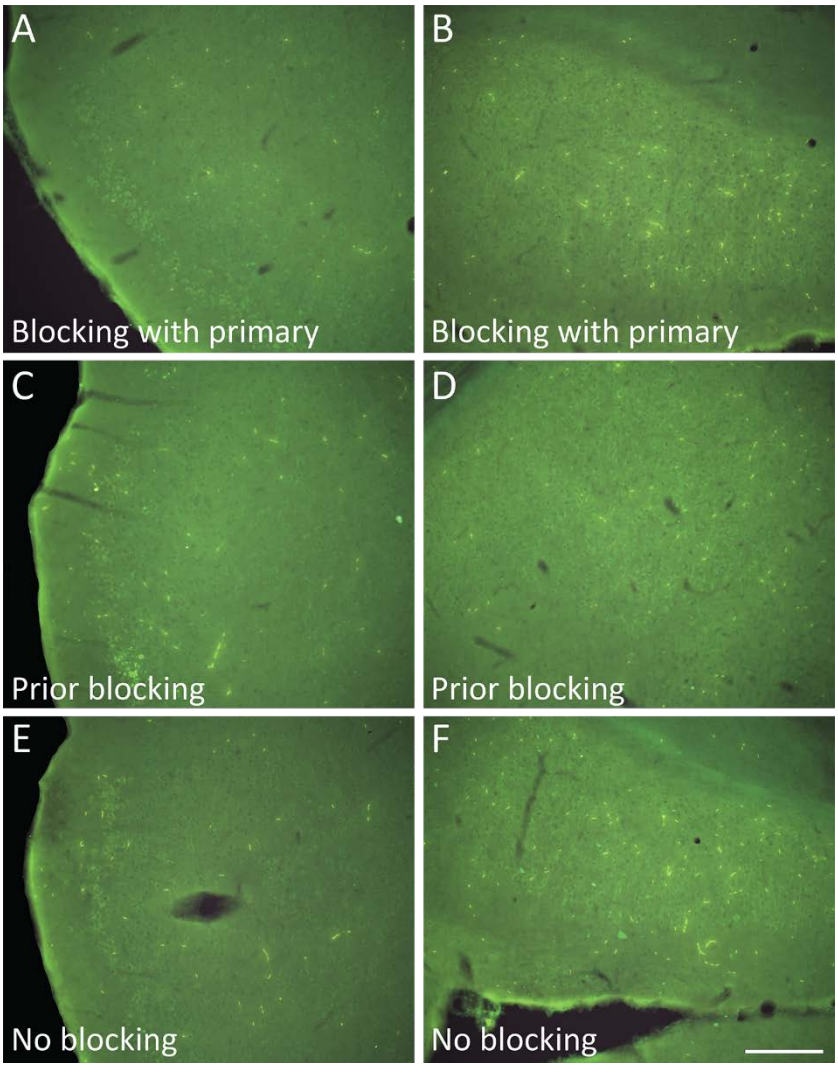

Figure G.6. Variations with blocking did not result in improved reelin labelling with the polyclonal rabbit antibody, as shown for tissue from a one month old homozygous McGill-R-Thy1-APP rat (ID: 20061). A, B: Incubation with 5% normal goat serum prior to incubation with primary antibodies and during primary antibody incubation; C, D: Incubating with 5% normal goat serum only prior to incubation with primary antibodies; E, F: No blocking. Areas shown are lateral entorhinal cortex (A, C, E) and subiculum (B, D, F). Scale bar: 200 µm.

No improvement in reelin labelling was evident when the time for incubation with primary antibodies was increased from overnight to 48 hours. Weakly labelled cells could be seen in LEC LII (Figure G.7 A, C), but not in any other areas (Figure G.7 B, D).

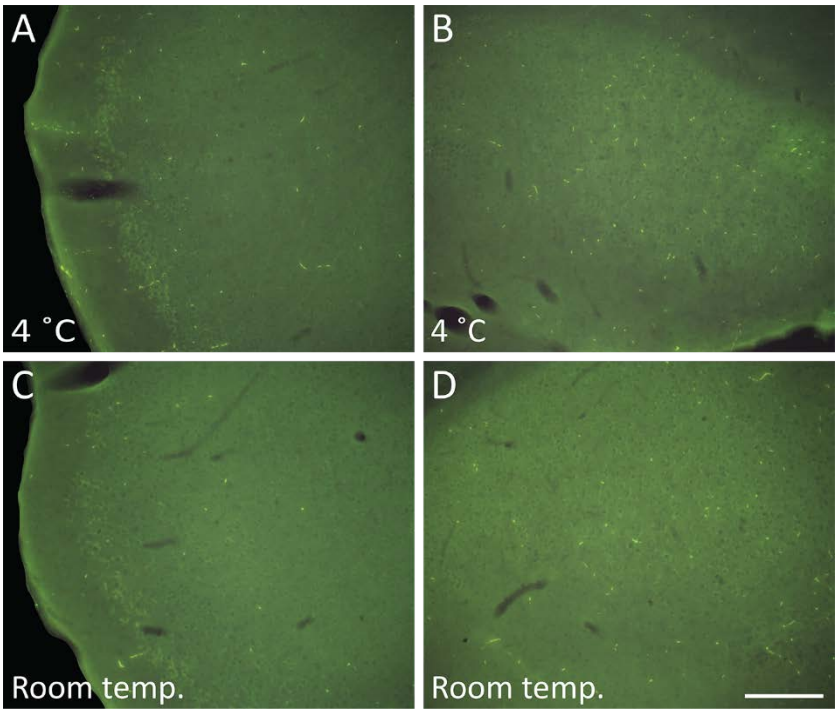

Figure G.7. 48 hours of incubation with the primary antibody did not result in improved reelin labelling with the polyclonal rabbit antibody, as shown for tissue from a one month old homozygous McGill-R-Thy1-APP rat (ID: 20061). A, B: Incubation at 4 ˚C; C, D: Incubation in room temperature. Areas shown are lateral entorhinal cortex (A, C) and subiculum (B, D). Scale bar: 200 µm.

No labelling of reelin could be seen with the purified batch of the rabbit anti-reelin antibody in any areas with the protocol tested.

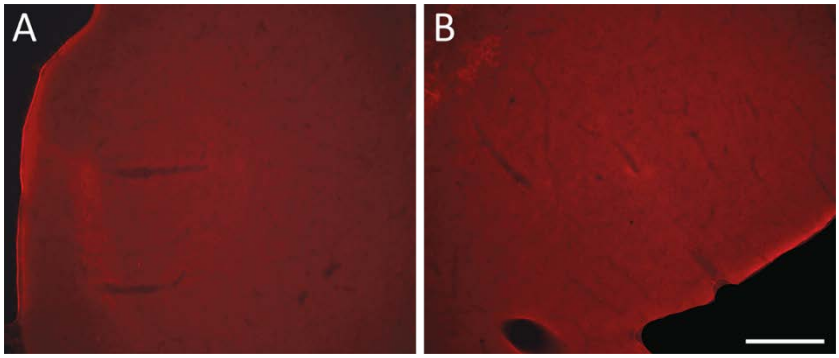

Figure G.8. The new, purified version of batch # 1660 of the polyclonal rabbit anti-reelin antibody did not result in any reelin labelling in any areas, as shown for lateral entorhinal cortex (A) and subiculum (B). Both sections are from a three months old homozygous McGill-R-Thy1-APP rat (ID: 17015). Scale bar: 200 µm.

APPENDIX H – SUPPLEMENTARY FIGURES

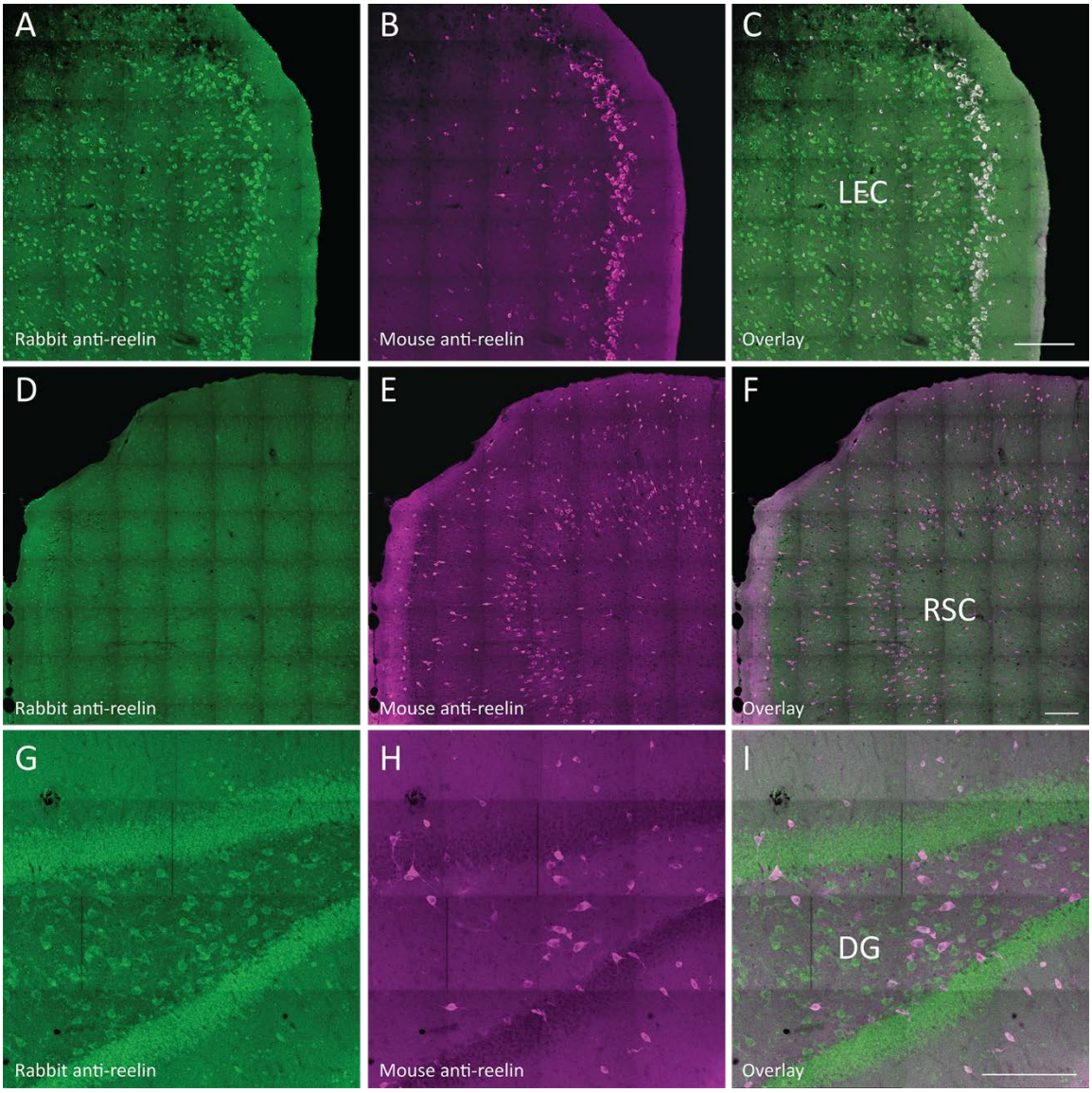

Figure H.1. Difference in labelling of reelin-immunoreactive cells with two reelin-specific antibodies, shown for lateral entorhinal cortex (LEC), retrosplenial cortex (RSC), and dentate gyrus (DG) of homozygous McGill-R-Thy1-APP transgenic rats. A-C: LEC of a three months old rat (ID: 17017); D-F: RSC of a one month old rat (ID: 20061); G-I: DG of a three months old rat (ID: 17017). A, D, G: rabbit anti-reelin; B, E, H: mouse anti-reelin; C, F, I: overlay. Scale bars: 200 µm.

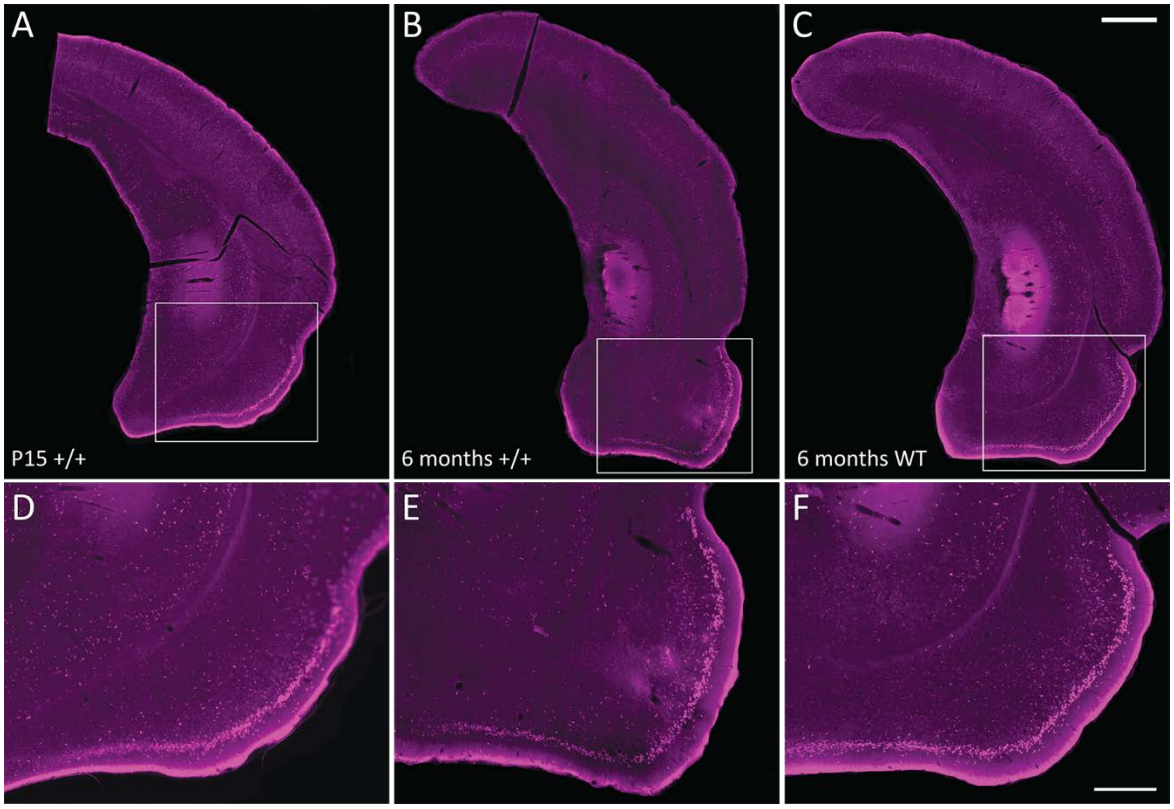

Figure H.2. No difference in reelin-expression between P15 and six month old homozygous McGill-R-Thy1-APP rats and six month old wild-type (WT) rats was evident from photomicrographs, as shown for three coronal sections at the approximately same rostro-caudal level. All sections are stained using mouse anti-reelin (G10). A: coronal section of a P15 homozygous rat (ID: 19875); B: coronal section of a six months old homozygous rat (ID: 15717); C: coronal section of a six months old WT rat (ID: 16121). D, E, and F show high-power images of the boxed areas indicated in A, B, and C, respectively. Scale bars: 1000 µm (A-C), 500 µm (D-F).

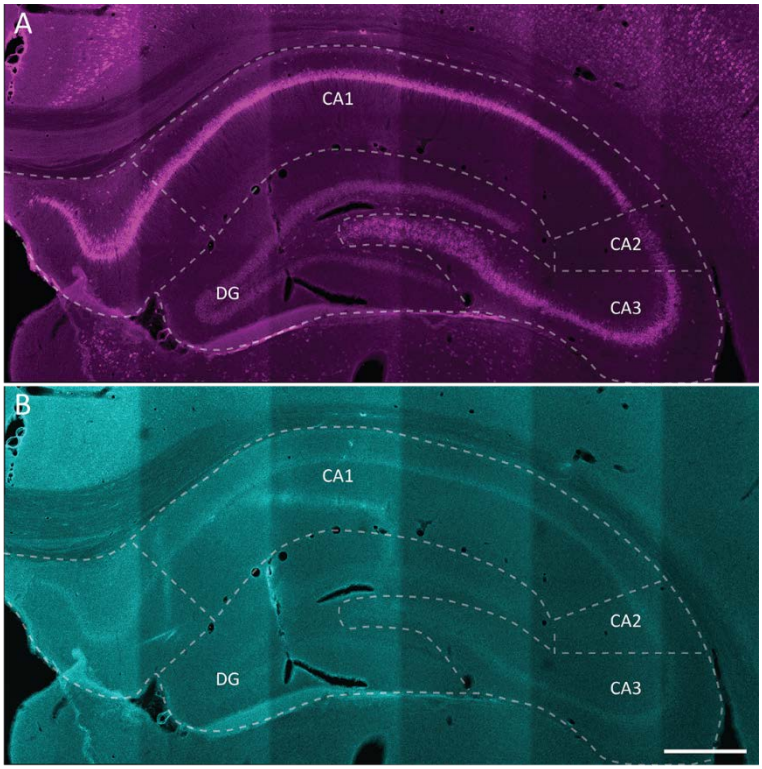

Figure H.3. Staining with McSA1 (mouse anti-human Aβ, IgG1) and the two secondary antibodies goat anti-mouse IgG1 A555 and goat anti-mouse IgG2a A647 revealed that the two secondary antibodies did not cross-react, as shown for a representative coronal section of a three months old homozygous McGill-R-Thy1-APP rat (ID: 19942). A: Goat anti-mouse IgG1 labelled Aβ-positive-positive cells; B: No cells were labelled with goat anti-mouse IgG2a. Scale bar: 500 µm. CA: Cornu Ammonis; DG: dentate gyrus.

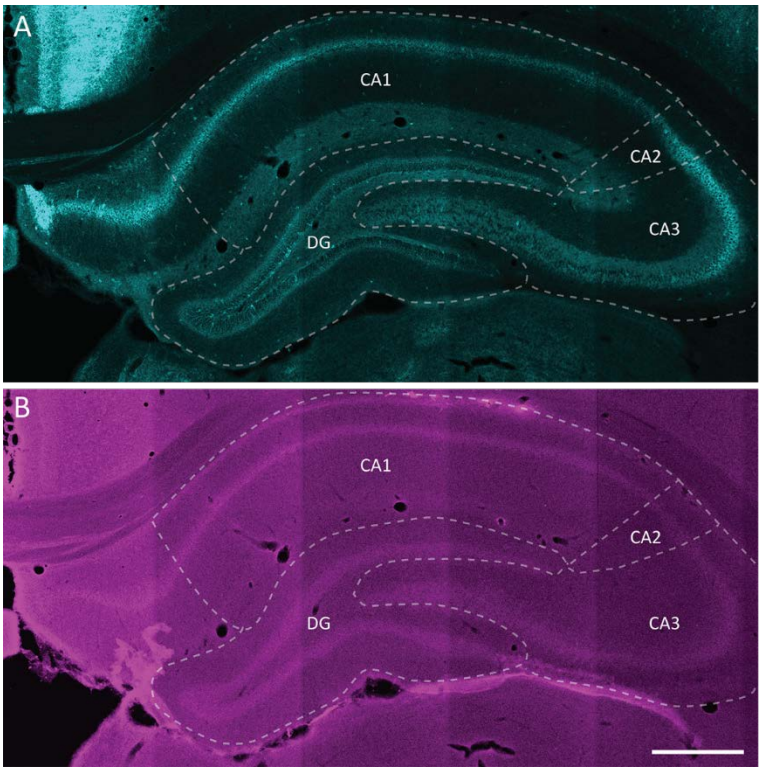

Figure H.4. Staining with mouse anti-GAD67 (IgG2a) and the two secondary antibodies goat anti-mouse IgG1 A555 and goat anti-mouse IgG2a A647 revealed that the two secondary antibodies did not cross-react, as shown for a representative coronal section of a three months old homozygous McGill-R-Thy1-APP rat (ID: 19942). A: Goat anti-mouse IgG2a labelled GAD67-positive-positive cells; B: No cells were labelled with goat anti-mouse IgG1. Scale bar: 500 µm. CA: Cornu Ammonis; DG: dentate gyrus.

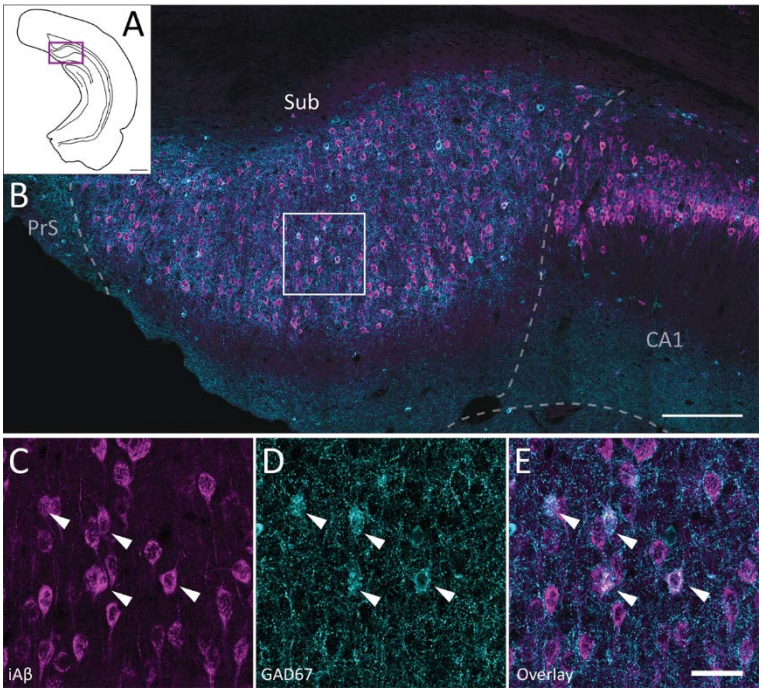

Figure H.5. GAD67-positive cells expressing iAβ in dorsal subiculum of a one month old homozygous McGill-R-Thy1-APP transgenic rat (ID: 20498). A: Schematic line drawing illustrating the rostro-caudal position of the selected coronal section. The boxed area indicates the extent and position of the high-power image shown in B. B: Co-localisation of GAD67 and iAβ in dorsal subiculum. C: iAβ-positive cells stained with McSA1 (mouse anti-human Aβ); D: interneurons stained with mouse anti-GAD67; E: overlay. Scale bars: 1000 µm (A), 200 µm (B), 40 µm (C-E). CA1: Cornu Ammonis 1; DG: dentate gyrus; PrS: presubiculum; Sub: subiculum.

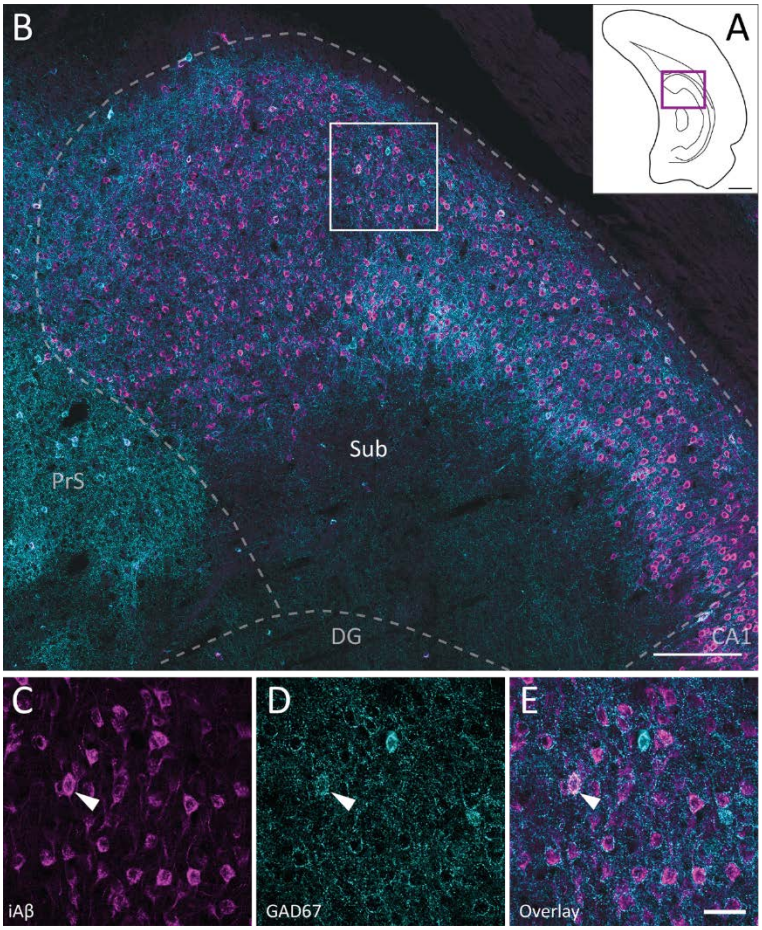

Figure H.6. GAD67-positive cells expressing iAβ in dorsal subiculum of a one month old homozygous McGill-R-Thy1-APP transgenic rat (ID: 20498). A: Schematic line drawing illustrating the rostro-caudal position of the selected coronal section. The boxed area indicates the extent and position of the high-power image shown in B. B: Co-localisation of GAD67 and iAβ in dorsal subiculum. C: iAβ-positive cells stained with McSA1 (mouse anti-human Aβ); D: interneurons stained with mouse anti-GAD67; E: overlay. Scale bars: 1000 µm (A), 200 µm (B), 40 µm (C-E). CA1: Cornu Ammonis 1; DG: dentate gyrus; PrS: presubiculum; Sub: subiculum.

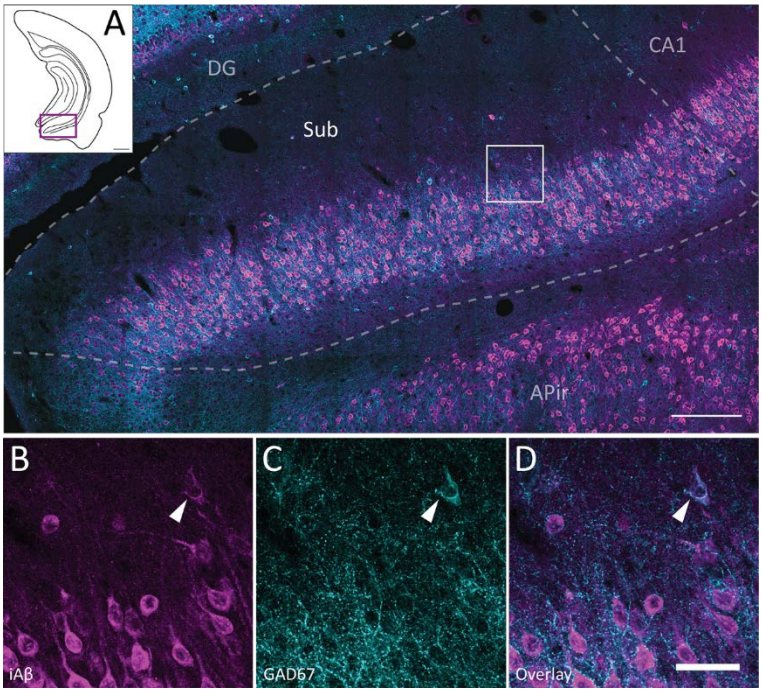

Figure H.7. GAD67-positive cells expressing iAβ in ventral subiculum of a one month old homozygous McGill-R-Thy1-APP transgenic rat (ID: 20498). A: Schematic line drawing illustrating the rostro-caudal position of the selected coronal section. The boxed area indicates the extent and position of the high-power image shown in B. B: Co-localisation of GAD67 and iAβ in ventral subiculum. C: iAβ-positive cells stained with McSA1 (mouse anti-human Aβ); D: interneurons stained with mouse anti-GAD67; E: overlay. Scale bars: 1000 µm (A), 200 µm (B), 40 µm (C-E). APir: Amygdaloipiriform transition area; CA1: Cornu Ammonis 1; DG: dentate gyrus; Sub: subiculum.

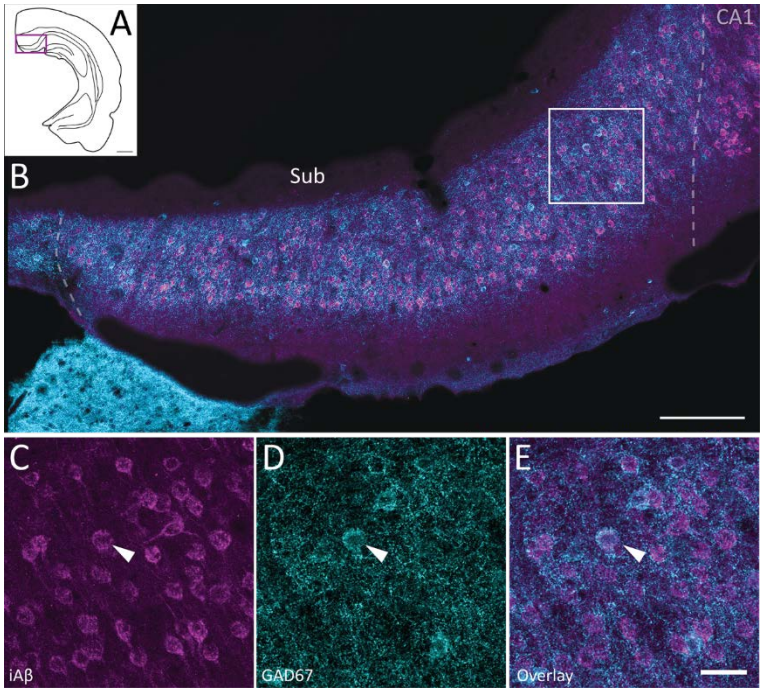

Figure H.8. GAD67-positive cells expressing iAβ in dorsal subiculum of a six months old homozygous McGill-R-Thy1-APP transgenic rat (ID: 16908). A: Schematic line drawing illustrating the rostro-caudal position of the selected coronal section. The boxed area indicates the extent and position of the high-power image shown in B. B: Co-localisation of GAD67 and iAβ in dorsal subiculum. C: iAβ-positive cells stained with McSA1 (mouse anti-human Aβ); D: interneurons stained with mouse anti-GAD67; E: overlay. Scale bars: 1000 µm (A), 200 µm (B) and 40 µm (C-E). CA1: Cornu Ammonis 1; Sub: subiculum.

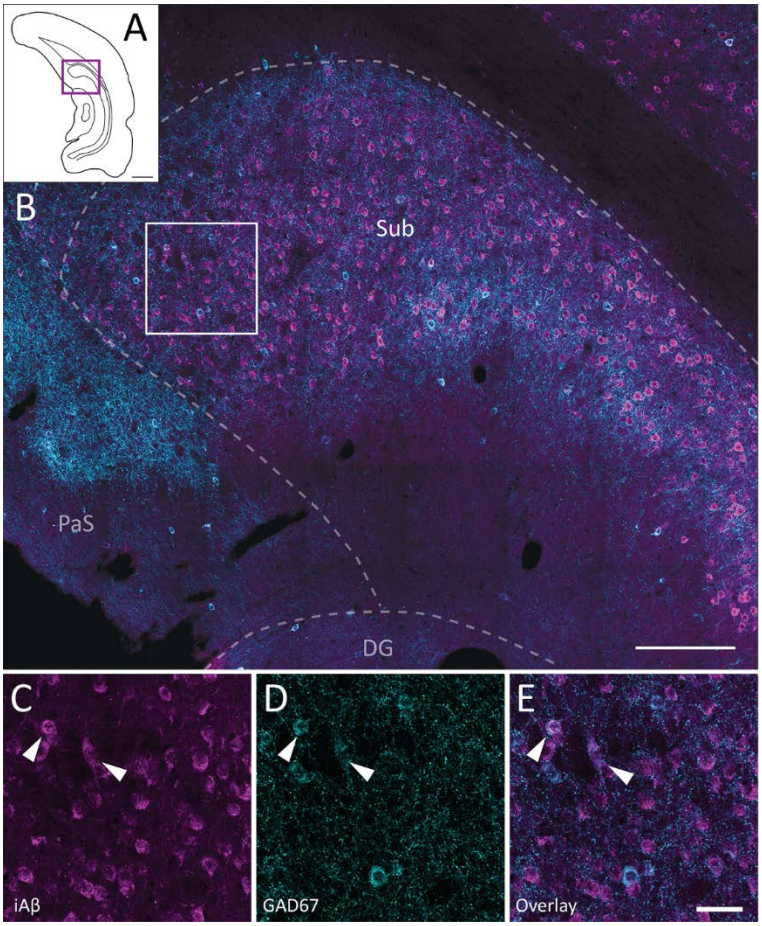

Figure H.9. GAD67-positive cells expressing iAβ in dorsal subiculum of a six months old homozygous McGill-R-Thy1-APP transgenic rat (ID: 16908). A: Schematic line drawing illustrating the rostro-caudal position of the selected coronal section. The boxed area indicates the extent and position of the high-power image shown in B. B: Co-localisation of GAD67 and iAβ in dorsal subiculum. C: iAβ-positive cells stained with McSA1 (mouse anti-human Aβ); D: interneurons stained with mouse anti-GAD67; E: overlay. Scale bars: 1000 µm (A), 200 µm (B), 40 µm (C-E). DG: dentate gyrus; PaS: parasubiculum; Sub: subiculum.

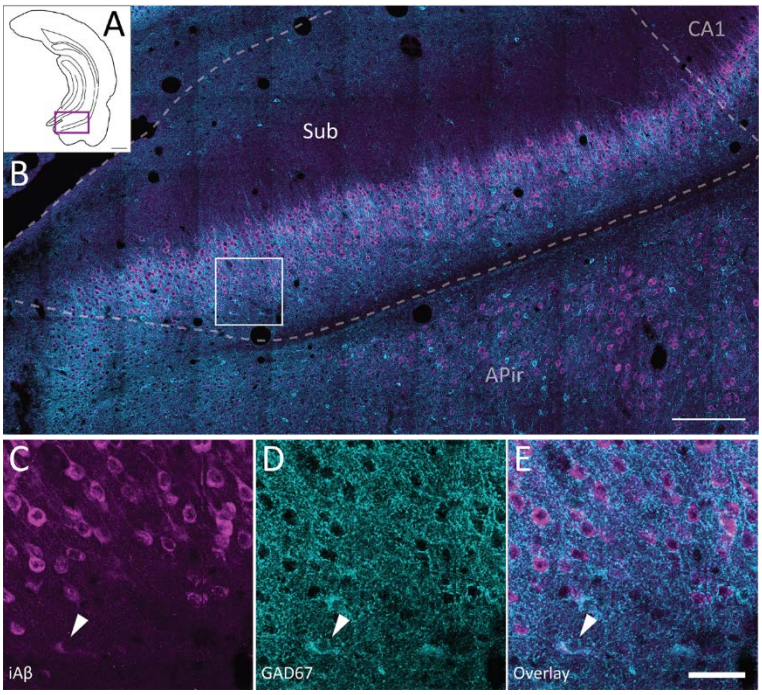

Figure H.10. GAD67-positive cells expressing iAβ in ventral subiculum of a six months old homozygous McGill-R-Thy1-APP transgenic rat (ID: 16908). A: Schematic line drawing illustrating the rostro-caudal position of the selected coronal section. The boxed area indicates the extent and position of the high-power image shown inB. B: Co-localisation of GAD67 and iAβ in ventral subiculum. C: iAβ-positive cells stained with McSA1 (mouse anti-human Aβ); D: interneurons stained with mouse anti-GAD67; E: overlay. Scale bars: 1000 µm (A), 200 µm (B), 40 µm (C-E). APir: Amygdaloipiriform transition area; CA1: Cornu Ammonis; Sub: subiculum.

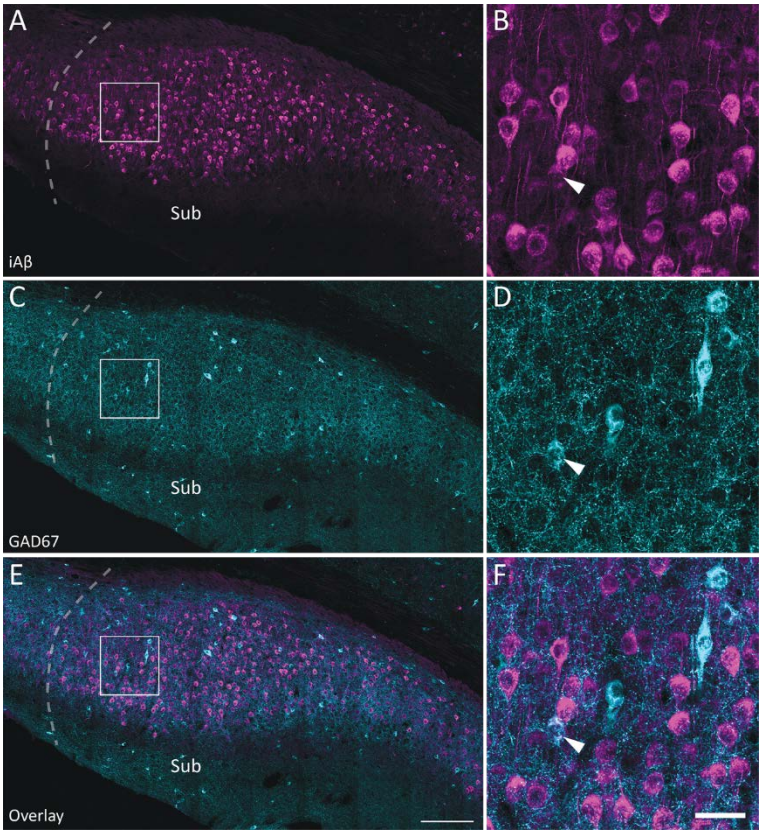

Figure H.11. GAD67-positive cells expressing iAβ in dorsal subiculum of a P15 homozygous McGill-R-Thy1-APP transgenic rat (ID: 19573). A: iAβ-positive cells stained with McSA1 (mouse anti-human Aβ); C: interneurons stained with mouse anti-GAD67; E: overlay. B, D, and F show high-power images of the boxed area indicated in A, C, and E, respectively. Scale bars: 200 µm (A, C, E), 40 µm (C-E). APir: Amygdaloipiriform transition area; CA1: Cornu Ammonis; Sub: subiculum.

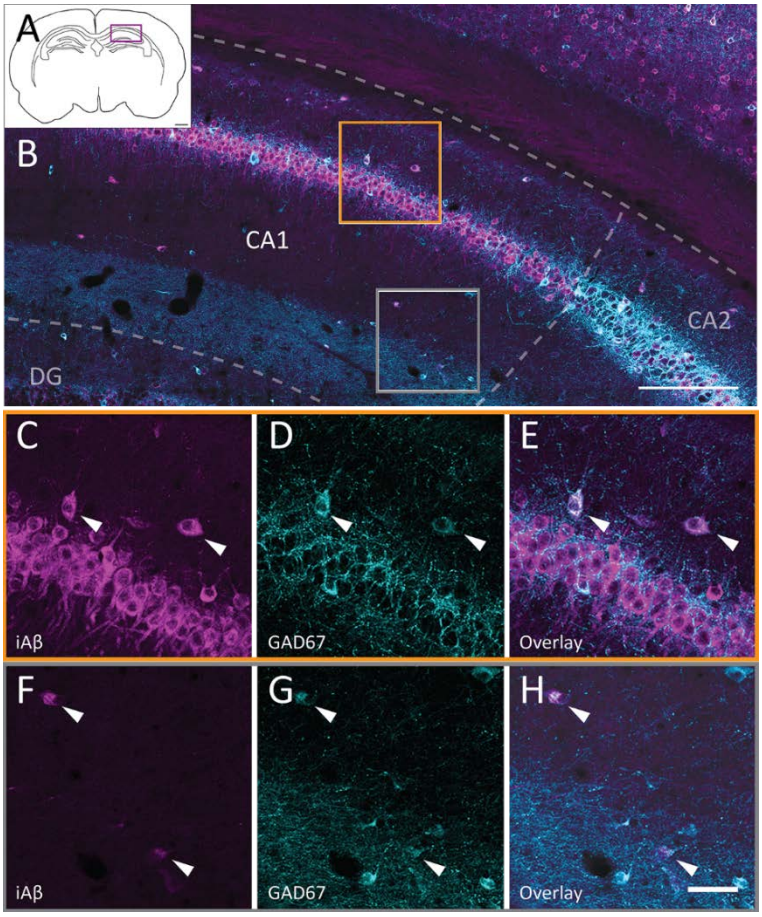

Figure H.12. GAD67-positive cells expressing iAβ in dorsal CA1 of a one month old homozygous McGill-R-Thy1-APP transgenic rat (ID: 20498). A: Schematic line drawing illustrating the rostro-caudal position of the selected coronal section. The boxed area indicates the extent and position of the high-power image shown in B. B: Co-localisation of GAD67 and iAβ in CA1. C, F: iAβ-positive cells stained with McSA1 (mouse anti-human Aβ); D, G: interneurons stained with mouse anti-GAD67; E, H: overlay. Scale bars: 1000 µm (A), 200 µm (B), 40 µm (C-H). CA: Cornu Ammonis, DG: dentate gyrus.

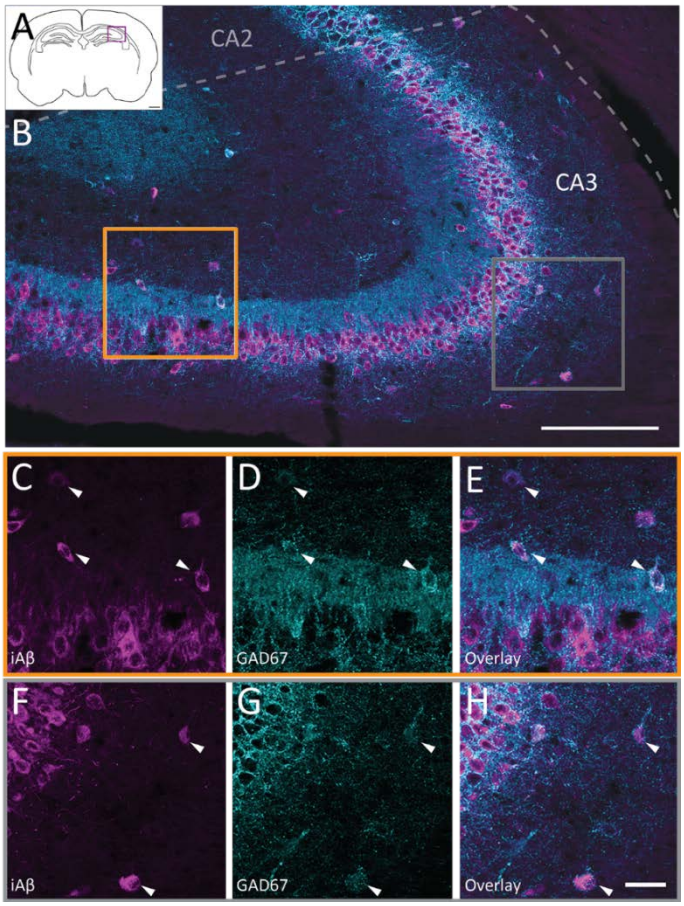

Figure H.13. GAD67-positive cells expressing iAβ in dorsal CA3 of a one month old homozygous McGill-R-Thy1-APP transgenic rat (ID: 20498). A: Schematic line drawing illustrating the rostro-caudal position of the selected coronal section. The boxed area indicates the extent and position of the high-power image shown in B. B: Co-localisation of GAD67 and iAβ in CA3. C, F: iAβ-positive cells stained with McSA1 (mouse anti-human Aβ); D, G: interneurons stained with mouse anti-GAD67; E, H: overlay. Scale bars: 1000 µm (A), 200 µm (B), 40 µm (C-H). CA: Cornu Ammonis.

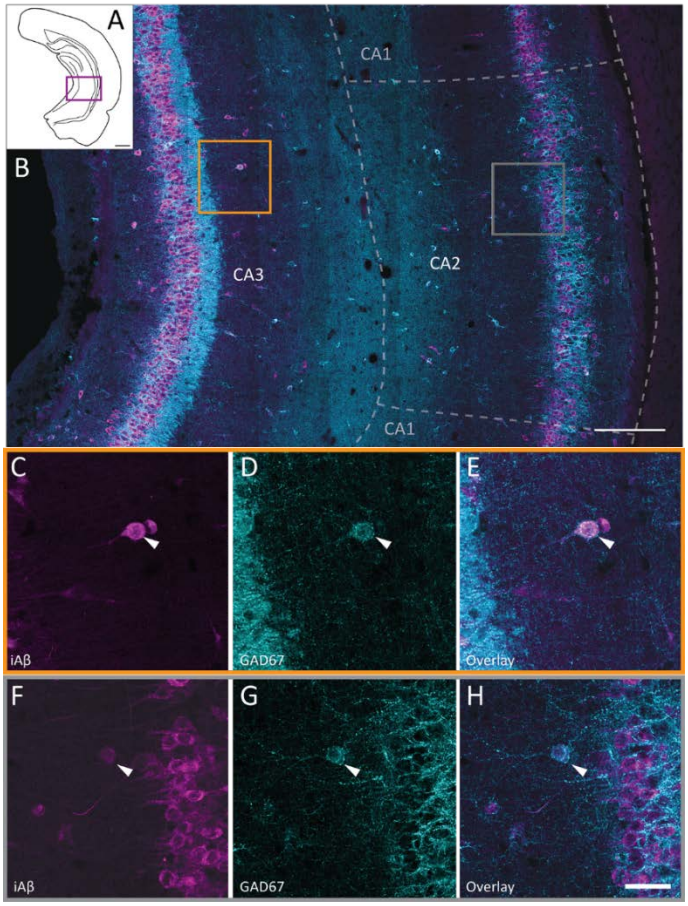

Figure H.14. GAD67-positive cells expressing iAβ in intermediate CA2 and CA3 of a one month old homozygous McGill-R-Thy1-APP transgenic rat (ID: 20498). A: Schematic line drawing illustrating the rostro-caudal position of the selected coronal section. The boxed area indicates the extent and position of the high-power image shown in B. B: Co-localisation of GAD67 and iAβ in CA3 and CA3. C, F: iAβ-positive cells stained with McSA1 (mouse anti-human Aβ); D, G: interneurons stained with mouse anti-GAD67; E, H: overlay. Scale bars: 1000 µm (A), 200 µm (B), 40 µm (C-H). CA: Cornu Ammonis.

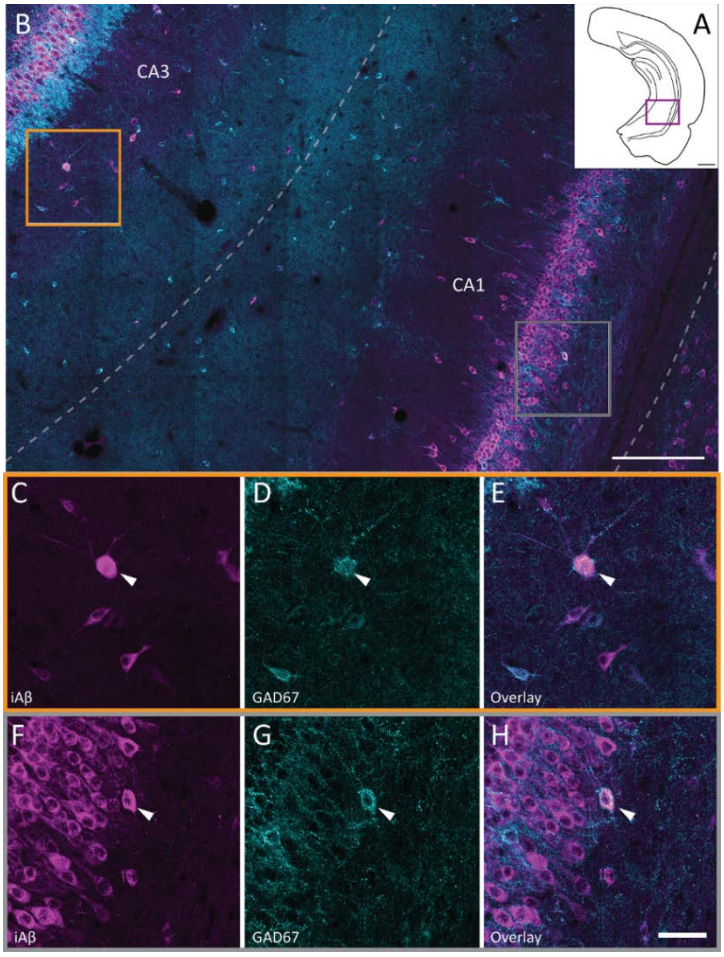

Figure H.15. GAD67-positive cells expressing iAβ in ventral CA1 and CA3 of a one month old homozygous McGill-R-Thy1-APP transgenic rat (ID: 20498). A: Schematic line drawing illustrating the rostro-caudal position of the selected coronal section. The boxed area indicates the extent and position of the high-power image shown in B. B: Co-localisation of GAD67 and iAβ in CA1 and CA3. C, F: iAβ-positive cells stained with McSA1 (mouse anti-human Aβ); D, G: interneurons stained with mouse anti-GAD67; E, H: overlay. Scale bars: 1000 µm (A), 200 µm (B), 40 µm (C-H). CA: Cornu Ammonis.

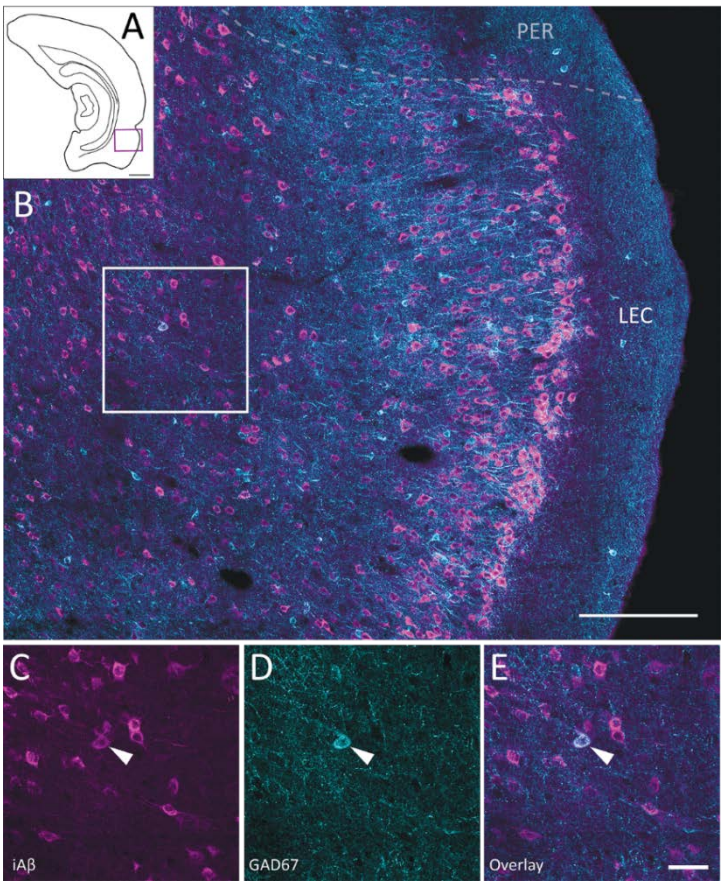

Figure H.16. GAD67-positive cells expressing iAβ in layer V of lateral entorhinal cortex (LEC) of a one month old homozygous McGill-R-Thy1-APP transgenic rat (ID: 20498). A: Schematic line drawing illustrating the rostro-caudal position of the selected coronal section. The boxed area indicates the extent and position of the high-power image shown in B. B: Co-localisation of GAD67 and iAβ in LEC. C: iAβ-positive cells stained with McSA1 (mouse anti-human Aβ); D: interneurons stained with mouse anti-GAD67; E: overlay. Scale bars: 1000 µm (A), 200 µm (B), 40 µm (C-E). PER: perirhinal cortex.

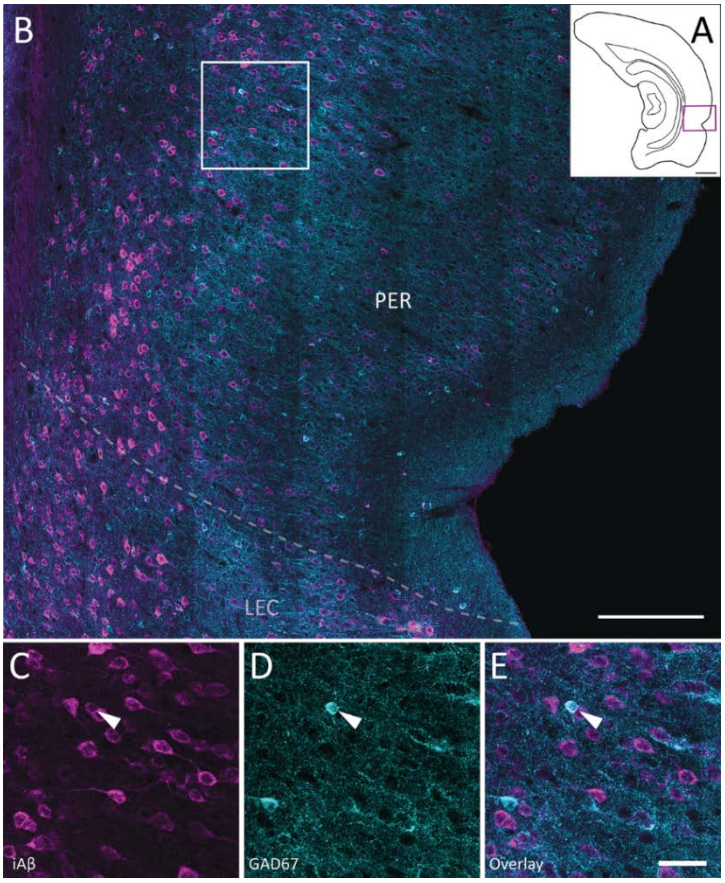

Figure H.17. GAD67-positive cells expressing iAβ in perirhinal cortex (PER) of a one month old homozygous McGill-R-Thy1-APP transgenic rat (ID: 20498). A: Schematic line drawing illustrating the rostro-caudal position of the selected coronal section. The boxed area indicates the extent and position of the high-power image shown in B. B: Co-localisation of GAD67 and iAβ in PER. C: iAβ-positive cells stained with McSA1 (mouse anti-human Aβ); D: interneurons stained with mouse anti-GAD67; E: overlay. Scale bars: 1000 µm (A), 200 µm (B), 40 µm (C-E). LEC: lateral entorhinal cortex.

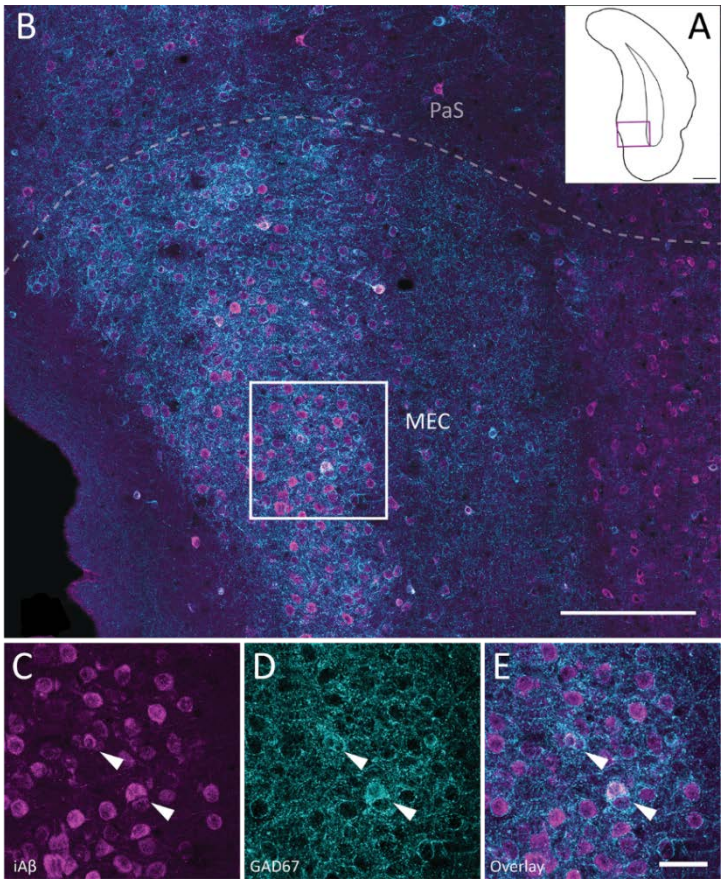

Figure H.18. GAD67-positive cells expressing iAβ in medial entorhinal cortex (MEC) of a three months old homozygous McGill-R-Thy1-APP transgenic rat (ID: 17019). A: Schematic line drawing illustrating the rostro-caudal position of the selected coronal section. The boxed area indicates the extent and position of the high-power image shown in B. B: Co-localisation of GAD67 and iAβ in MEC. C: iAβ-positive cells stained with McSA1 (mouse anti-human Aβ); D: interneurons stained with mouse anti-GAD67; E: overlay. Scale bars: 1000 µm (A), 200 µm (B), 40 µm (C-E). PaS: parasubiculum.

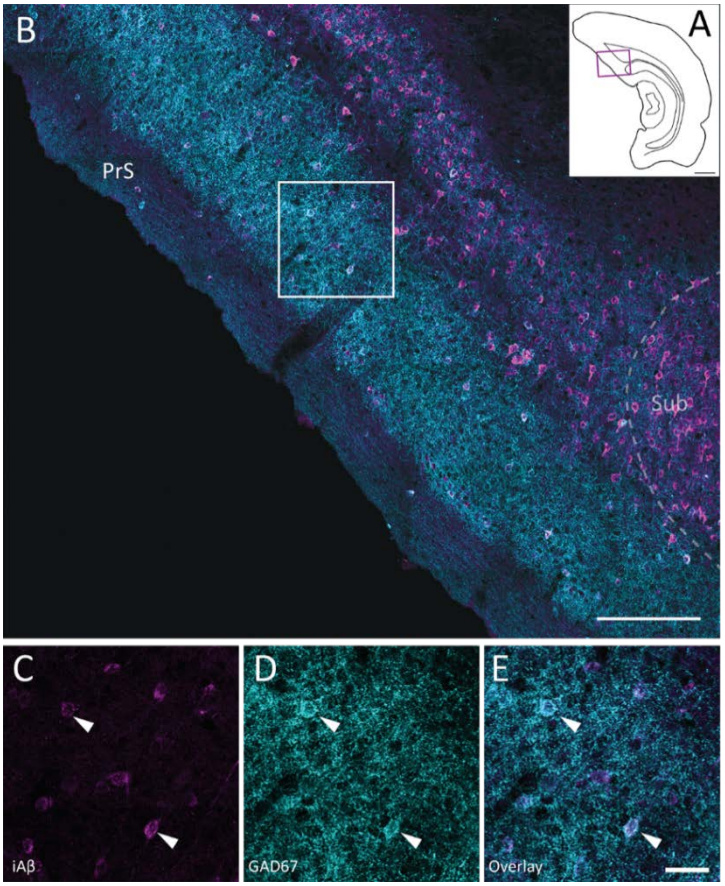

Figure H.19. GAD67-positive cells expressing iAβ in presubiculum (PrS) of a one month old homozygous McGill-R-Thy1-APP transgenic rat (ID: 20498). A: Schematic line drawing illustrating the rostro-caudal position of the selected coronal section. The boxed area indicates the extent and position of the high-power image shown in B. B: Co-localisation of GAD67 and iAβ in PrS. C: iAβ-positive cells stained with McSA1 (mouse anti-human Aβ); D: interneurons stained with mouse anti-GAD67; E: overlay. Scale bars: 1000 µm (A), 200 µm (B), 40 µm (C-E). Sub: subiculum.

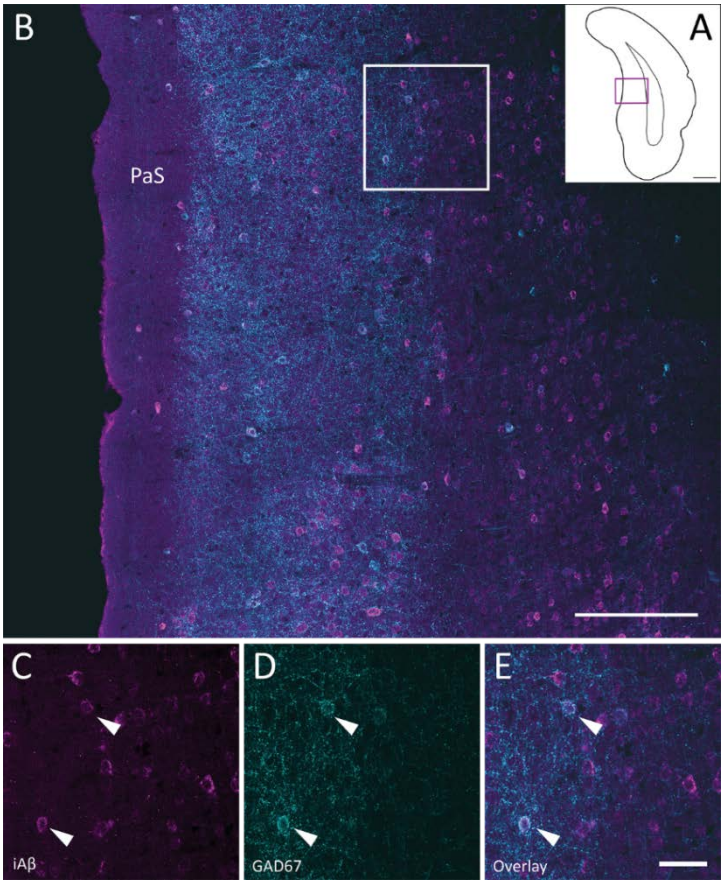

Figure H.20. GAD67-positive cells expressing iAβ in parasubiculum (PaS of a three months old homozygous McGill-R-Thy1-APP transgenic rat (ID: 17019). A: Schematic line drawing illustrating the rostro-caudal position of the selected coronal section. The boxed area indicates the extent and position of the high-power image shown in B. B: Co-localisation of GAD67 and iAβ in PaS. C: iAβ-positive cells stained with McSA1 (mouse anti-human Aβ); D: interneurons stained with mouse anti-GAD67; E: overlay. Scale bars: 1000 µm (A), 200 µm (B), 40 µm (C-E).

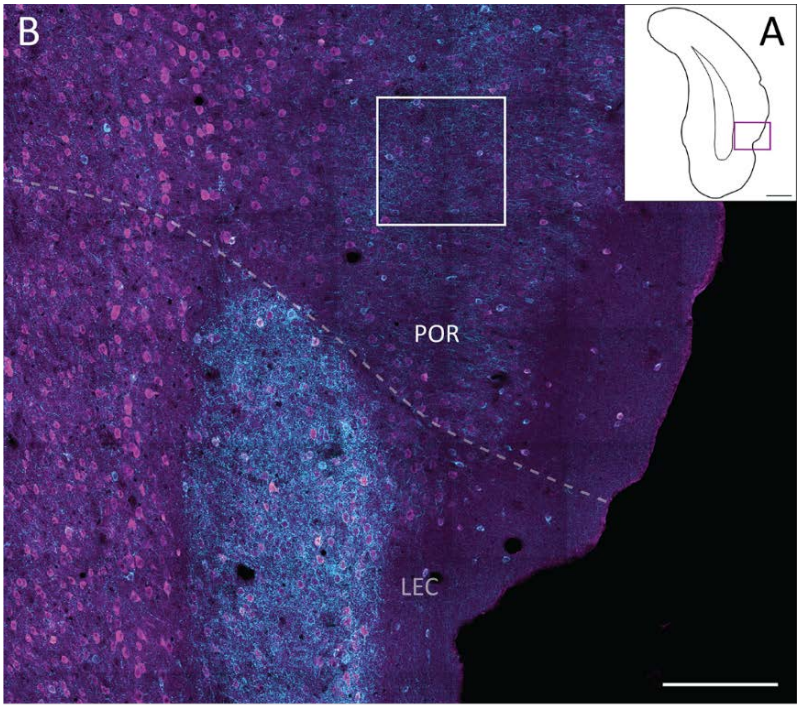

Figure H.21. GAD67-positive cells expressing iAβ in postrhinal cortex (POR) of a three months old homozygous McGill-R-Thy1-APP transgenic rat (17019). A: Schematic line drawing illustrating the rostro-caudal position of the selected coronal section. The boxed area indicates the extent and position of the high-power image shown in B. B: Co-localisation of GAD67 and iAβ in PaS. C: iAβ-positive cells stained with McSA1 (mouse anti-human Aβ); D: interneurons stained with mouse anti-GAD67; E: overlay. Scale bars: 1000 µm (A), 200 µm (B), 40 µm (C-E). LEC: lateral entorhinal cortex.

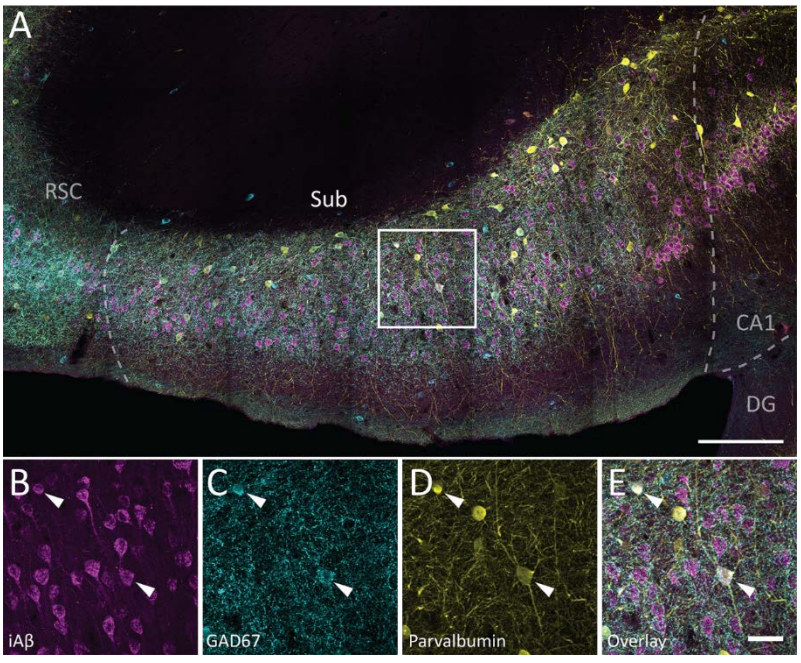

Figure H.22. GAD67-positive cells expressing parvalbumin and iAβ in dorsal subiculum of a three months old homozygous McGill-R-Thy1-APP transgenic rat (17015). A: Co-localisation of GAD67, parvalbumin, and iAβ. B: iAβ-positive cells stained with McSA1 (mouse anti-human Aβ); C: interneurons stained with mouse anti-GAD67; D: parvalbumin-positive cells stained with rabbit anti-parvalbumin; E: overlay. Scale bars: 200 µm (A), 40 µm (B-E). CA: Cornu Ammonis; DG: dentate gyrus; RSC: retrosplenial cortex; Sub: subiculum.

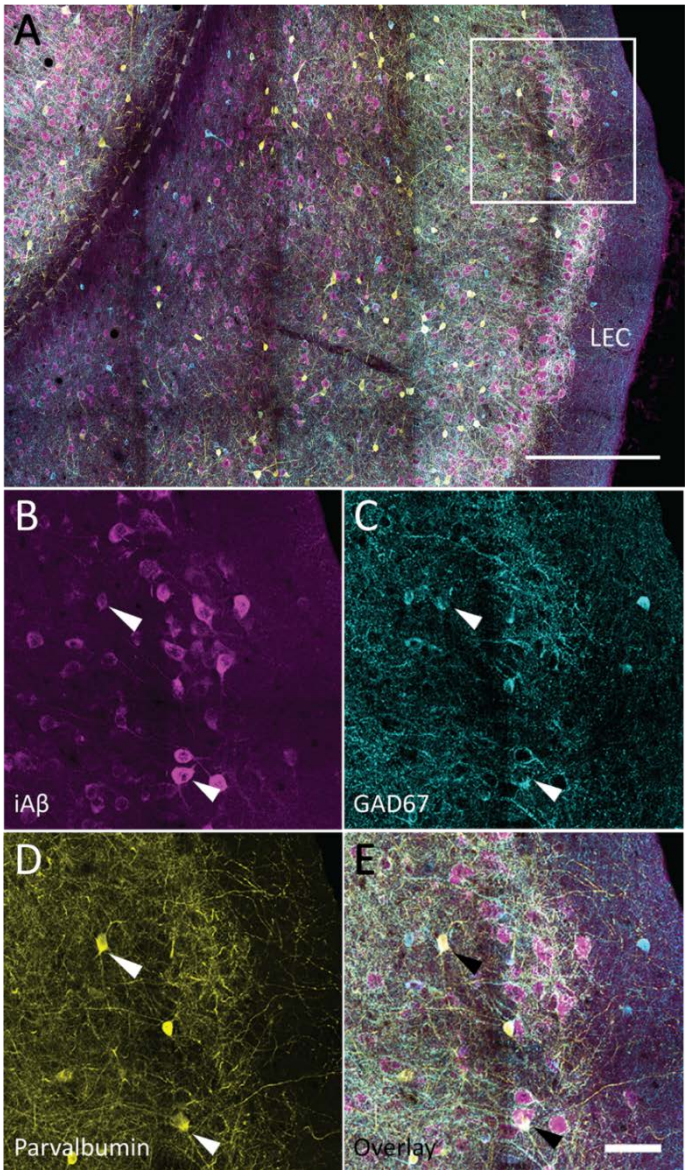

Figure H.23. GAD67-positive cells expressing parvalbumin and iAβ in lateral entorhinal cortex (LEC) of a three months old homozygous McGill-R-Thy1-APP transgenic rat (17015). A: Co-localisation of GAD67, parvalbumin, and iAβ. B: iAβ-positive cells stained with McSA1 (mouse anti-human Aβ); C: interneurons stained with mouse anti-GAD67; D: parvalbumin-positive cells stained with rabbit anti-parvalbumin; E: overlay. Scale bars: 200 µm (A), 40 µm (B-E).

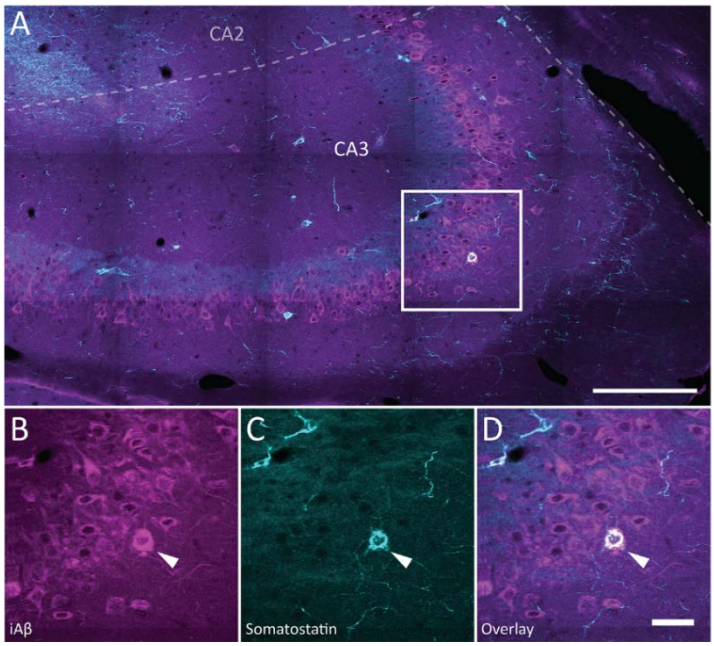

Figure H.24. Somatostatin-positive cells expressing iAβ in CA3 of a six months old homozygous McGill-R-Thy1-APP transgenic rat (ID: 16804). A: Co-localisation of somatostatin and iAβ in CA3. B: iAβ-positive cells stained with McSA1 (mouse anti-human Aβ); C: somatostatin-positive cells stained with goat anti-somatostatin; D: overlay. Scale bars: 200 µm (A), 40 µm (B-D). CA: Cornu Ammonis.